Atomically thin magnetic semiconductors open exciting perspectives for both fundamental research and future applications at the interface between optoelectronics and spintronics. The van der Waals-layered magnet CrSBr is a particularly promising system, owing to the complex coupling of its magnetic order and quasi-1D excitons, whose ultrafast dynamics are of paramount importance for potential quantum devices.

In this work, we combine sub-cycle terahertz polarisation nanoscopy with a tunable source of optical excitation pulses to selectively prepare and probe excitons and unbound electron-hole pairs in CrSBr, irrespective of interband selection rules. We unveil femtosecond recombination of photoexcited quasi-1D excitons in atomically thin CrSBr, which is 30 times shorter than in the bulk, where two distinct decay dynamics suggest scattering of excitons with paramagnons. Moreover, we directly extract the nonequilibrium dielectric function of monolayer CrSBr showcasing the hallmark of transitions between highly excited excitons. Our experiments demonstrate how combining ultrafast near-field microscopy with tunable pump pulses can reveal spectral fingerprints and femtosecond dynamics of exotic quasiparticles in microscopic quantum materials.

Pushing towards exploring the femtosecond dynamics of magnetic systems on the atomic scale, we introduce a scalable and versatile terahertz emission scheme perfectly suited for lightwave-driven scanning tunnelling microscopy. The novel emitters based on spatially indirect interband transitions in epitaxial quantum wells generate intense, sub-half-cycle field transients, whose single positive peak exceeds the strongest negative excursion by more than three times. In combination with a recently built scanning tunnelling microscope capable of applying strong external magnetic fields, such remarkably asymmetric waveforms are expected to drive unipolar, spin-selective tunnelling currents in time windows much shorter than 100 fs, for the first time enabling simultaneous state-selective, atom-scale and ultrafast microscopy of individual spins.

Cover: A metallic tip confines terahertz waveforms (blue, left) to its apex, such that by recording the scattered field transient (blue, right) quasi-1D electron-hole pairs (glowing blue and red spheres) in a CrSBr crystal can be probed in a nanoscopic volume with femtosecond precision.

Universität Regensburg
Institut für Experimentelle und Angewandte Physik
Lehrstuhl Prof. Dr. Rupert Huber

Christian Meineke – **From ultrafast electronic dynamics in 2D materials towards spin-resolved atom-scale videography**

From ultrafast electronic dynamics in 2D materials towards spin-resolved atom-scale videography

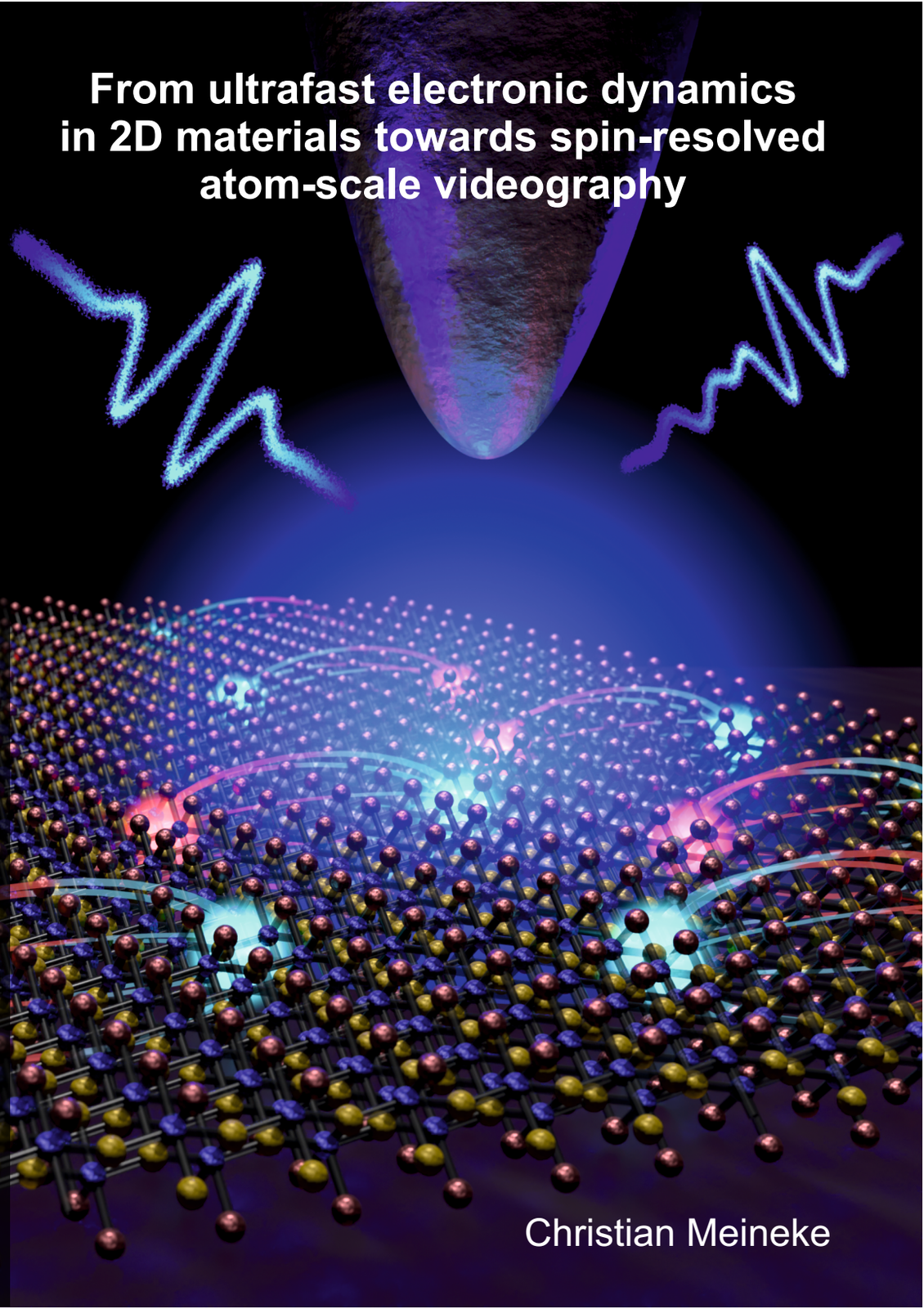

Christian Meineke

From ultrafast electronic dynamics in 2D materials towards spin-resolved atom-scale videography

Dissertation
zur Erlangung des Doktorgrades der Naturwissenschaften
(Dr. rer. nat.)
der Fakultät für Physik der Universität Regensburg

vorgelegt von
Christian Helmut Meineke
aus Landshut
im Jahr 2024

Das Promotionsgesuch wurde eingereicht am: 15.01.2024
Die Arbeit wurde angeleitet von: Prof. Dr. Rupert Huber

Prüfungsausschuss:	Vorsitzender:	Prof. Dr. Vladimir Braun
	1. Gutachter:	Prof. Dr. Rupert Huber
	2. Gutachter:	Prof. Dr. Jascha Repp
	weiterer Prüfer:	Prof. Dr. Jörg Wunderlich

Meinen Eltern.

Contents

Es soll sich regen, schaffend handeln
Erst sich gestalten, dann verwandeln
Nur scheinbar steht's Momente still
Das Ewige regt sich fort in allen
Denn alles muss in Nichts zerfallen
Wenn es im Sein beharren will

— Johann Wolfgang von Goethe,
Eins und alles (1821)

Chapter 1

Introduction: Ultrafast nanoscopy of quantum materials

Throughout history, scientists have endeavoured to break the observable world down into its elementary building blocks. Contemporary solid state physics understands solids as electrostatically bound compounds of typically 10^{23} atoms per cubic centimetre. Despite the enormous number of degrees of freedom involved in these systems, pioneers of condensed matter physics have put forth quantitative descriptions of crystalline solids by condensing the collective behaviour of many interacting electrons into dressed states called *quasiparticles*[1–3]. A prime example of this approach is the description of electrons in the conduction band of a semiconductor. Instead of treating the interaction of the excited electron with all remaining valence band electrons, a new quasiparticle, the positively charged *hole*, is introduced. Both the electron and hole quasiparticles are attributed a respective *effective* mass, which incorporates the electrostatic interaction with the environment in the crystal. In this way, the dynamics of the electron and hole can be treated in analogy to free charge carriers in vacuum.

While this single-particle picture is remarkably elegant and accurately describes electronic dynamics in a wide variety of solids, it faces limitations, when applied to materials marked by strong correlations of the quantum degrees of freedom of charge, spin, orbit and lattice. Their complex interplay not only challenges our understanding of the fundamental processes in condensed matter, but also gives

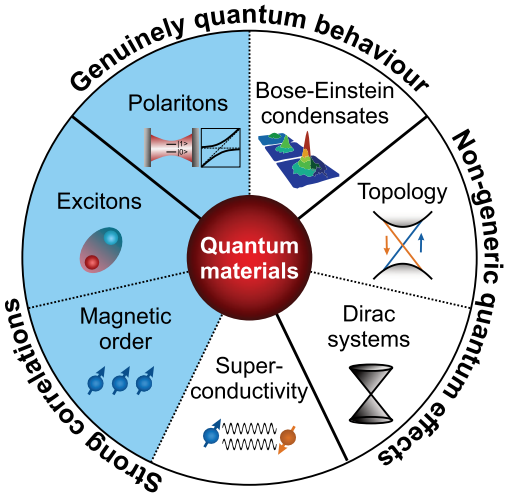

Figure 1.1 | Overview of selected emergent phenomena in quantum materials. Quantum materials are subject to complex quantum effects and/or correlations between the fundamental quantum degrees of freedom of charge, spin, orbit and lattice. The van der Waals layered magnet CrSBr hosts a multitude of intertwined quantum phases, marked as blue segments.

rise to many fascinating quantum phases in solids, such as magnetic order and superconductivity. These *emergent* phenomena, epitomising the age-old idea that "*the whole is greater than the sum of its parts*", are expected to open unprecedented frontiers in sensing, energy and information technologies[4]. As a consequence, research on so-called *quantum materials*[4–6], condensing correlated materials, which low-level quantum mechanics fails to describe, under one term, is at the heart of 21st century solid state physics (Figure 1.1).

In the last two decades, condensed matter physics has been driven by the development of new fabrication methods and the search for new types of van der Waals layered materials, which, owing to weak interlayer binding forces, can be mechanically exfoliated down to the atomically thin limit[7,8]. Two-dimensional semiconductors like transition metal dichalcogenide monolayers do not only pave the way for func-

tional devices at the limit of miniaturisation[9,10], but they harbour unique quantum states[11,12]. In particular, the confinement of electron–hole pairs in atomically thin transition metal dichalcogenides gives rise to strong Coulomb correlations, resulting in the formation of hydrogen-like bound states, called excitons. As these tightly bound electron–hole pairs are stable even at room temperature[13], strongly interact with light and form on ultrafast timescales after photoexcitation[14], they are promising candidates for optoelectronic devices.

Recently, the class of two-dimensional materials has been complemented by the discovery of a broad variety of van der Waals layered magnets[15–18], which have drawn tremendous attention, as they interface many research fields such as quantum electronics and optics as well as spintronics. Among van der Waals layered magnets, the quantum material CrSBr stands out for its extremely anisotropic electronic structure, rendering it an *intrinsically* quasi-one-dimensional semiconductor[19], which sets it apart from previously available, artificially synthesised one-dimensional systems like quantum wires[20], nanotubes[21,22], or moiré superlattices[23]. The microscopic processes in CrSBr are marked by pronounced correlations of electron–hole pairs with the lattice and spin-order, giving rise to strongly correlated excitons[19,24–26] in a rich magnetic environment[27–32] (Figure 1.1). Moreover, these magnetic excitons strongly couple to light, creating exciton–polaritons, which further correlate with collective spin excitations, called magnons[33,34]. The intricate interconnection of the quantum degrees of freedom in CrSBr opens up exciting possibilities for studies of emergent quantum phenomena in condensed matter and promises a wide range of next-generation technologies such as quantum sensors, data storage or processing units.

Pantha rhei – everything flows

— Heraclitus, (c. 500 BC)

Generally, the key to understanding and harnessing the function of novel quantum devices is to study their dynamics at the microscopic level. In the monolayer limit of CrSBr, where the quasi-one-dimensional character of electron–hole pairs is strongest, the large exciton binding energy of hundreds of meV is comparable to the one of well-understood excitons in transition metal dichalcogenide monolayers[35,36], suggest-

ing similar, ultrashort radiative exciton recombination times on the femtosecond ($1\,\mathrm{fs} = 10^{-15}\,\mathrm{s}$) timescale. However, despite their pivotal role for future research and applications, the exciton dynamics on ultrafast timescales have remained unknown.

A powerful tool to investigate femtosecond electron–hole pair dynamics in correlated materials like CrSBr is time-resolved optical spectroscopy. (Multi-)terahertz ($1\,\mathrm{THz} = 10^{12}\,\mathrm{Hz}$) pulses are a particularly versatile probe, as they couple to low-energy excitations including vibrations of the crystal lattice, called phonons[37,38], magnons[39–41], and polarisable electron–hole pairs[14,42,43]. Phase-locked terahertz field transients are routinely detected in a phase-resolved manner, allowing for *sub-cycle* temporal resolution[44,45]. Moreover, by tracing the amplitude and phase of the terahertz waveforms after photoexcitation, the ultrafast time evolution of the full, complex-valued dielectric function of the sample can be retrieved. Exploiting these capabilities, femtosecond exciton formation[14], recombination[36] and the dynamics of interlayer tunnelling[46] have been unveiled in two-dimensional semiconductors. However, as a consequence of the diffraction limit[47], the spatial resolution of far-field terahertz techniques is inherently restricted by the large entailed wavelengths ($1\,\mathrm{THz} \mathrel{\hat{=}} 300\,\mu\mathrm{m}$) which exceed the scales of magnetic domains and even the typical lateral dimensions of CrSBr monolayers.

Near-field microscopy[48–53] is an elegant method to resolve this mismatch: When light is focused onto a sharp metallic tip, the evanescent electric field probes the local dielectric properties of the sample in a volume governed by the tip apex, thereby providing nanoscale spatial resolution largely independent of the probe wavelength. Therefore, near-field microscopy has been harnessed to all-optically explore ultrafast phenomena in nanoobjects[54–56], such as the exciton Mott transition in bilayers of transition metal dichalcogenides[57]. In this work, near-field microscopy is pushed to its limits to reveal the femtosecond formation and decay of paramagnetic electron–hole pairs in CrSBr bulk and even monolayers. We combine ultrafast polarisation nanoscopy[56,57], a technique based on sub-cycle near-field microscopy at terahertz frequencies, with a source of tunable optical pump pulses, which allows us to selectively inject electron–hole pairs in excitonic or continuum states. The phase-locked terahertz probe fields directly trace the dynamics of all electron–hole pairs, regardless of interband selection rules. In this way, an extremely short, femtosecond exciton lifetime in atomically thin CrSBr is revealed, which is over an

order of magnitude shorter than in the bulk, where two distinct decay dynamics are observed. In the initial relaxation process, scattering with short-range spin correlation, called paramagnons, could occur, while the slower decay is attributed to recombination of excitons. Furthermore, near-field spectroscopy unveils the hallmark dielectric signatures of bound and unbound electron–hole pairs in bulk CrSBr, providing valuable information on the exciton binding energies. Furthermore, the complex-valued dielectric function of a photoexcited CrSBr monolayer is retrieved in a model-free manner, featuring the spectral fingerprints of internal transitions between exciton states with high principal quantum numbers.

Ultimately, investigating the strong correlations of charge and spin in atomically thin magnetic systems calls for probing techniques with atom-scale spatial resolution. Moreover, exploring and controlling the ultrafast dynamics of *individual* spins could mark a paradigm shift in the study of magnetically ordered matter. Lightwave-driven scanning tunnelling microscopy[58–62] provides the means to accomplish this vision. By replacing the bias voltage with the transient electric field of an intense, phase-stable field transient, ultrafast, sub-cycle tunnelling currents can be driven through an atom-scale tip-sample junction, thereby uniting the Angstrom ($1\,\text{Å} = 10^{-10}\,\text{m}$) spatial precision of scanning tunnelling microscopy with femtosecond temporal resolution. In this work, in a collaboration with the group of Prof. Jascha Repp we strive towards the ambitious milestone of combined femtosecond and atom-scale exploration of single spins by developing the next generation of lightwave-driven scanning tunnelling microscopy. While Prof. Repp's group focused on a new ultra-high vacuum scanning tunnelling microscope, which allows one to apply strong external magnetic fields, here, we designed and realised a novel and scalable source of sub-cycle terahertz field transients acting as ultimately short transient bias. Exploiting a new emission mechanism based on ultrafast quenching of photoinduced shift currents in custom-tailored, epitaxially grown semiconductor heterostructures, intense terahertz waveforms are generated, which comprise only one pronounced field maximum, accompanied by two feeble field minima. Such an asymmetric waveform is ideally suited to open tunnelling windows as short as tens of femtoseconds, marking a substantial advancement for the time resolution of lightwave-driven tunnelling experiments. Merging this optimised source of sub-cycle field transients with the new state-of-the-art tunnelling microscope will result in an unprecedented experimental

setup, which is expected to allow one to explore and manipulate the ultrafast dynamics of single spins on the atomic scale.

This work is structured as follows: In **Chapter 2**, I introduce the fundamental properties of the van der Waals magnet CrSBr, focussing on the highly anisotropic electronic structure, which includes quasi-one-dimensional excitons. The technique of scattering-type near-field optical microscopy and an accurate analytical model of the entailed nanoscale light-matter interaction is discussed in **Chapter 3**, before we focus on the concept of terahertz polarisation nanoscopy. Moreover, the corresponding experimental setup, which comprises a source of intense, phase-locked terahertz probe pulses and a scheme for phase-resolved detection, is described in detail. In **Chapter 4**, we delve into the functional principle and experimental setup of the noncollinear optical parametric amplifier, which was designed and built in this work to operate as a high-repetition-rate source of tunable, ultrashort laser pulses for photoexcitation. In **Chapter 5**, I present, how the previously introduced techniques are merged into a powerful and flexible scheme of ultrafast terahertz nanoscopy, which allows us to reveal the ultrafast dynamics of strongly correlated electron–hole pairs in the quantum material CrSBr in both its bulk and monolayer form. Following up on femtosecond nanoscopy of magnetic quantum systems, in **Chapter 6**, I briefly introduce the technique of lightwave-driven scanning tunnelling microscopy. Subsequently, I present a novel mechanism for generation of phase-locked and strongly sub-cycle terahertz field transients based on ultrafast quenching of shift currents in custom-tailored epitaxial semiconductor heterostructures. We then assess these scalable emitters, finding that the generated intense, strongly asymmetric waveforms constitute the ideal ultrashort bias for lightwave-driven tunnelling microscopy and spectroscopy. Finally, the experimental findings are concluded and an outlook on future experiments, particularly spin-resolved ultrafast nanoscopy, is given in **Chapter 7**.

Chapter 2

The quasi-one-dimensional quantum material CrSBr

Starting with the discovery of graphene[7], two-dimensional crystals have initiated a paradigm shift in condensed matter physics. These materials, comprising individual layers bound only by weak van der Waals interactions, allow atomically thin films to be readily manufactured by mechanical exfoliation. Transition metal dichalcogenide (TMDC) monolayers[8] have further revolutionised the field by providing access to strongly Coulomb-bound electron-hole pairs, that is, excitons[35], making them promising candidates for novel room-temperature optoelectronic devices at the limit of miniaturisation. Importantly, van der Waals materials introduce a new way to custom-tailor strong Coulomb correlations by stacking monolayer crystals at tunable twist angles[63–68]. Recently, a plethora of van der Waals *magnets* has been discovered[15–18], fostering thriving research of two-dimensional magnetism. As the family of atomically thin magnets is rapidly growing, it has become a diverse material class, encompassing both metals, such as VSe_2[69] and Fe_3GeTe_2[70], as well as semicondcutors like CrI_3[15,71,72], $CrGeTe_3$[16,73], $CrPS_4$[74], $MnPS_3$[73,75,76], $NiPS_3$[77–79] and many more[18,73].

Among atomically thin semiconductors, which offer particularly viable prospects for future high-performance optoelectronics, spintronics and data storage, the quantum material CrSBr stands out as both its bulk and monolayer forms host tightly bound excitons[19,24–26,33] in a magnetic environment[27–32]. Moreover, the electronic and spin

structures of CrSBr are extremely anisotropic, rendering the material quasi-one-dimensional, even in its bulk form[19,26]. Therefore, CrSBr provides a readily available platform to investigate and harness quantum phenomena in a quasi-one-dimensional material, complementing artificially synthesised systems such as nanoribbons and nanotubes available to date.

Intriguingly, the microscopic dynamics in CrSBr are marked by strong coupling of its spin order and lattice with the electronic structure, resulting in an enormous phase space for manipulation and exploration of intricately intertwined quantum degrees of freedom. Examples of the plethora of highly correlated phenomena in CrSBr include spin-phonon[80–82] and exciton-magnon coupling[24,25]. Furthermore, placed in external cavities, CrSBr is subject to strong light-matter interaction and hosts magnetically dressed cavity modes, that is, exciton-polaritons[33,34]. The dynamics of many of these emergent phenomena are expected to unfold on ultrafast timescales as short as picoseconds ($1\,\mathrm{ps} = 10^{-12}\,\mathrm{s}$) or even femtoseconds ($1\,\mathrm{fs} = 10^{-15}\,\mathrm{s}$). However, to date, despite the key importance for fundamental research and future quantum devices, even very elementary dynamics, such as the ultrafast recombination of tightly bound excitons in CrSBr have remained unexplored. Thus, a major goal of this work is to unravel the femtosecond dynamics and the lifetime of quasi-one-dimensional excitons in bulk and, most importantly, monolayer CrSBr.

In this chapter, I will introduce the unique quasi-one-dimensional quantum material CrSBr by providing an overview over its anisotropic lattice (Section 2.1), magnetic (Section 2.2) and electronic structure (Section 2.3). In Section 2.4, I will discuss how the interplay of strong Coulomb correlations and electronic anisotropy gives rise to quasi-one-dimensional excitons and how these influence the optoelectronic properties of CrSBr compared to well-known van der Waals materials.

2.1 Crystal structure

Bulk CrSBr is composed of stacks of individual layers, which are bound by van der Waals forces. The monolayer crystallises in an orthorhombic lattice with space group *Pmmn* and point group symmetry $D_{2\mathrm{h}}$ and comprises buckled planes of covalently bound CrS embedded in sheets of bromine[27]. As viewed along the out-of-plane c-axis, CrSBr has a rectangular structure with two distinct in-plane axes featuring lattice

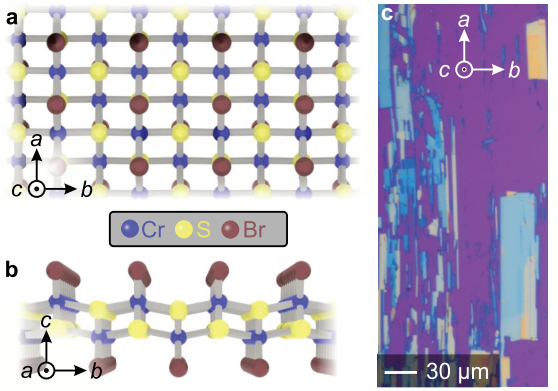

Figure 2.1 | Crystal structure of CrSBr. **a**, Crystal structure of CrSBr as viewed along the out-of-plane c-axis. **b**, Crystal structure of a CrSBr monolayer as viewed along the a-axis. **c**, Optical micrograph of exfoliated CrSBr featuring needle-like flakes extending along the a-axis.

constants of $a = 3.50\,\text{Å}$ and $b = 4.76\,\text{Å}$, respectively[27] (Figure 2.1a). Individual layers have a thickness of $c = 7.96\,\text{Å}$. The side view of the monolayer (Figure 2.1b) shows that atoms of the same chemical element – that is, chromium, sulphur and bromine – align along the a-axis, while the crystal structure along the b-axis is marked by alternating Cr–S chains.

Owing to the weak van der Waals binding of the individual layers, bulk CrSBr crystals can be readily mechanically exfoliated down to a monolayer. The in-plane anisotropy of the lattice manifests itself in the stripe-like shape of exfoliated CrSBr crystals, which extend along the a-axis (Figure 2.1c). This distinctive alignment enormously simplifies the in-situ identification of the crystallographic orientation of CrSBr samples in experiments. The lattice structure of CrSBr remains unchanged as a function of temperatures[27]. Moreover, in contrast to most currently known van der Waals magnets, CrSBr is chemically stable under ambient conditions[81].

2.2 Magnetic order

In the class of van der Waals magnets, CrSBr stands out particularly for its high magnetic order temperatures. Below its Néel temperature, $T_\text{N} = 132\,\text{K}$, bulk CrSBr is an A-type antiferromagnet, that is, the individual layers exhibit ferromagnetic order, while the interlayer coupling is of antiferromagnetic nature[83] (Figure 2.2a).

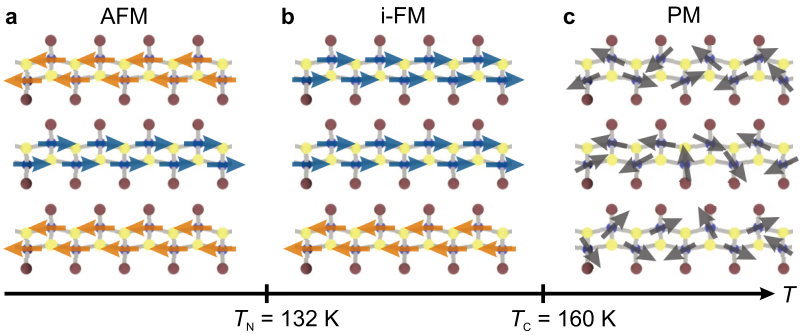

Figure 2.2 | Magnetic order in bulk CrSBr. a, Below its Néel temperature, T_N, bulk CrSBr exhibits ferromagnetically ordered layers which couple antiferromagnetically. **b**, Between T_N and the Curie temperature, T_C, an intermediate magnetic phase (i-FM) has been predicted, in which the interlayer coupling is paramagnetic[28]. **c**, At temperatures above T_C, the intralayer magnetic order of CrSBr collapses, leaving it in a paramagnetic state.

Interestingly, the isotropic Heisenberg model of magnetism forbids magnetic order in two-dimensional systems[84]. Thus, (anti-)ferromagnetism is only stable in the presence of magnetic anisotropy. Indeed, CrSBr exhibits a triaxial magnetic anisotropy with the easy axis along the *b*-axis, the intermediate *a*-axis and the hard *c*-axis[27].

With decreasing number of layers, T_N increases from 132 K (bulk) towards 145 K, which is the Curie temperature of the monolayer limit[28] This increase contradicts the conventional picture suggesting a decreased stability of the magnetic order, when the two-dimensional limit is approached. In the literature, this discrepancy is attributed to the presence of an intermediate magnetic phase, labelled i-FM, in which individual layers are ferromagnetically ordered internally, but the interlayer coupling remains paramagnetic[28] (Figure 2.2b). The intralayer magnetic order of CrSBr collapses into the paramagnetic phase (Figure 2.2c) above the Curie temperature, which scales with the sample thickness from 146 K in the monolayer limit to 160 K in the bulk[28].

Strong magnetic correlations. The rich magnetic structure of CrSBr is tightly and intricately coupled to its lattice, electronic structure and optical properties. CrSBr exhibits strong spin-phonon coupling[81,82] and a large negative magnetore-

sistance that is variable by the carrier concentration[85]. Furthermore, a complex interplay between magnons and Coulomb-bound electron–hole pairs, that is, excitons, has been revealed[24]. The exciton-magnon interaction can be mechanically tuned[25,86] and even be controlled by strong light-matter interaction in cavity-coupled CrSBr[33,34], opening an avenue for manipulating its magneto-optic properties on ultrashort timescales. Even in the absence of long-range magnetic order, short-range and short-lived magnetic fluctuations, so-called paramagnons, have been shown to couple to charge carriers in correlated materials[87,88]. Since signatures of paramagnon scattering have already been observed in the van der Waals magnet $CrPS_4$ at a temperature exceeding its Néel and Curie temperatures by a factor of four and three, respectively[74], these spontaneous spin correlations are expected to influence the electronic structure of CrSBr on ultrashort timescales, even at room temperature.

2.3 Highly anisotropic electronic structure

Beyond the complex intertwining of spin and charge carriers, the electronic structure of CrSBr is unique in its own right. Recent transport measurements in bulk CrSBr have discovered an extreme anisotropy of the conductivity along the in-plane a- and b-axis, revealing a contrast ratio of 10^5, which corresponds to quasi-one-dimensional transport[89]. This observation agrees with the calculated, exceptionally anisotropic band structure of CrSBr[19] (Figure 2.3). The lowest conduction band is almost flat along the Γ–X direction, where the high-symmetry point X corresponds to movement along the a-axis. In stark contrast, the band is parabolic in the Γ–Y direction, associated to a momentum along the b-axis. The highest valence band shows similar, yet less pronounced asymmetry. Quantitatively, the anisotropy is reflected in the respective effective electron and hole masses[19], $m_X^{\mathrm{e}} = 7.31\,m_0$, $m_Y^{\mathrm{e}} = 0.14\,m_0$, $m_X^{\mathrm{h}} = 2.84\,m_0$ and $m_Y^{\mathrm{h}} = 0.45\,m_0$. The ratio of effective electron masses of almost 50 even exceeds the corresponding ratio in black phosphorus[90]. Microscopically, the extreme electronic anisotropy of CrSBr originates from the orbital composition around the valence band maximum and conduction band minimum, respectively: The charge density around the Fermi level is predominantly localised along the Cr–S chains in the b-direction, while the orbitals of the Br atoms barely contribute. As the Cr and S atoms and orbitals are embedded in Br sheets, this admixture of

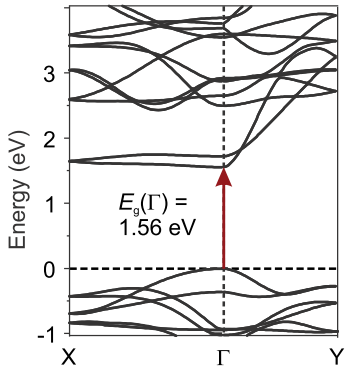

Figure 2.3 | Highly anisotropic electronic structure of CrSBr. Band structure of bulk CrSBr along the high-symmetry points X–Γ–Y calculated by means of density-functional theory. The conduction band is flat along the Γ–X direction, which is associated to a momentum along the *a*-axis. The corresponding effective electron mass amounts to $m_X^e = 7.31\,m_0$, Along the Γ–Y direction, associated to a momentum along the *b*-axis, the conduction band is parabolic, featuring an effective electron mass of $m_Y^e = 0.14\,m_0$. Adapted from Reference 19.

electronic states results in a feeble interlayer hybridisation. Consequently, even in its bulk form, CrSBr shows characteristics of a quasi-one-dimensional system, making it an exceptional subject for investigating strongly correlated phenomena in low dimensions.

While CrSBr is known to be a direct-bandgap semiconductor, independently of the number of layers, the magnitudes of the corresponding bandgaps are still under debate. Scanning tunnelling spectroscopy studies report a bulk bandgap of (1.5 ± 0.2) eV (References 19 and 27). Meanwhile, angle-resolved photoemission spectroscopy measurements have suggested a bandgap exceeding 1.5 eV and shown good agreement with calculations predicting 2.1 eV (Reference 91). Moreover, the knowledge about of the bandgap of the monolayer is limited to calculations, predicting a direct bandgap of 2.1 eV (Reference 19).

2.4 Quasi-one-dimensional excitons

One reason, why determining the single-particle bandgap of CrSBr has remained elusive, is that its electronic structure is dominated by excitons, that is, electron–hole pairs, which are bound by strong Coulomb attraction. Therefore, unveiling the internal structure and dynamics of excitons in CrSBr is a key challenge for research on this material system. Generally, the microscopic description of excitons distinguishes between Frenkel[92] and Wannier-Mott[93] excitons. The strongly bound

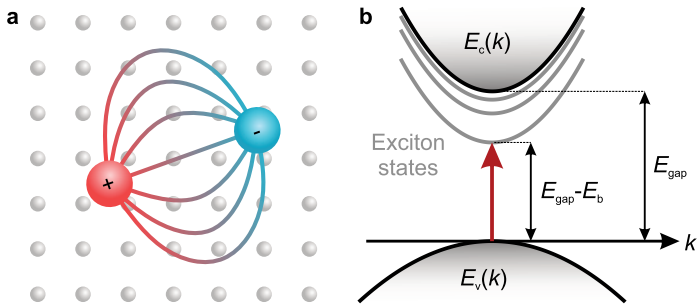

Figure 2.4 | Electronic properties of excitons. a, Schematic sketch of a Wannier-Mott exciton spread over multiple unit cells of a crystal lattice. **b**, Simplified band structure of a direct-bandgap semiconductor with an energy gap, E_{gap}, between valence band (E_v) maximum and conduction band (E_c) minimum. The Coulomb-bound exciton states (grey lines) emerge within the gap, reducing the optical bandgap by the exciton binding energy, E_b.

Frenkel excitons mostly occur in molecules or ion crystals and feature large binding energies of up to 1 eV. As they are localised to one lattice site, their transport is dominated by tunnelling to neighbouring atoms. In contrast, weakly bound Wannier-Mott excitons, typically found in inorganic semiconductors, exhibit an electron–hole distance of multiple lattice constants (Figure 2.4a). Their quasi-free movement in the crystal allows for a microscopic description in analogy to the hydrogen atom[94], giving rise to a series of excitonic states within the single-particle bandgap (Figure 2.4b). Consequently, the 1s ground state reduces the optical bandgap by the exciton binding energy, E_b.

In most bulk semiconductors, the large dielectric permittivity ($\varepsilon \sim 10$) strongly screens the Coulomb interaction, resulting in small binding energies on the order of few meV (Figure 2.5a). At room temperature, thermal fluctuations dissociate these excitons and, thus, they play a negligible role for the electronic properties of most dielectrics. Monolayer TMDCs introduced a paradigm shift in the study of excitons by providing a platform that hosts tightly bound Wannier-Mott excitons with binding energies in the hundreds of meV[11,13,36,46,95,96]. This drastic enhancement of the Coulomb binding compared to bulk TMDCs can be attributed to, on the one hand,

the spatial confinement of electron and hole wavefunction to a two-dimensional plane, which causes an increase of the binding energy by a factor of four[94] (Figure 2.5b). On the other hand, typical monolayer samples are exfoliated on a substrate featuring a drastically smaller dielectric permittivity than the TMDC. As a consequence, the two half spaces of vacuum or air and the substrate, which surround the monolayer, barely screen the attractive Coulomb interaction of electrons and holes, further enhancing the exciton binding energy[13].

When the effective masses of electrons and holes are strongly anisotropic, where the effective masses along one direction in momentum space are much larger than the rest mass of a free electron, the exciton is not only confined to an individual layer, but also along the crystal axis associated to the higher effective masses (Figure 2.5c). In CrSBr monolayers, the unparalleled ratio of reduced effective masses ratio of almost 20 results in an extremely anisotropic, quasi-one-dimensional exciton wavefunction (Figure 2.6, Appendix B.2 for details on the calculation).

Absorption spectra in low-dimensional semiconductors. The dimensionality of the electronic structure distinctly manifests itself in the absorption spectra. In conventional bulk semiconductors with a fairly isotropic band structure, the exciton appears as an absorption peak close to the single-particle bandgap energy, E_{gap}, reflecting its small binding energy (Figure 2.5d). Since the oscillator strength of three-dimensional exciton states scales with their principal quantum number, n, as n^{-3} (Reference 94), higher states have only a marginal effect on the absorption spectrum. Furthermore, Coulomb correlations cause an increase of the absorption above the bandgap compared to a pure single-particle microscopic description (dashed line), commonly known as Sommerfeld enhancement[94]. When the semiconductor is reduced to an atomically thin layer, the weaker dielectric screening and the spatial confinement drastically increase the binding energy, such that multiple exciton absorption peaks are clearly separated from the Sommerfeld-enhanced continuum absorption (Figure 2.5e). Moreover, the stronger spatial overlap of electron and hole wavefunction gives rise to large oscillator strengths, which directly translate to enhanced absorption compared to the three-dimensional case. In a quasi-one-dimensional system such as CrSBr, the oscillator strengths and binding energies are expected to further increase (Figure 2.5f). Additionally, the strong electronic

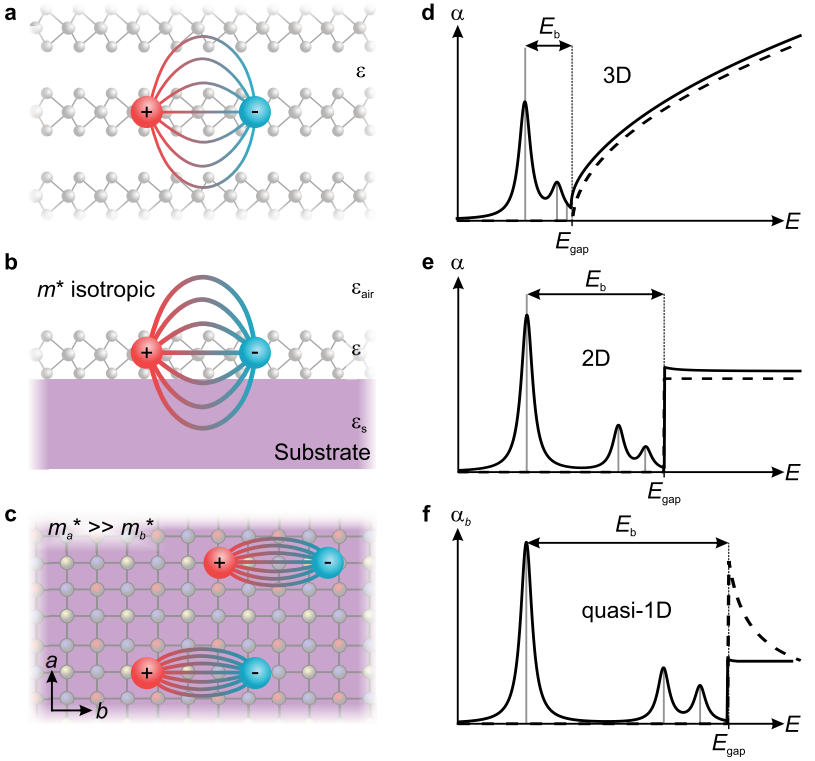

Figure 2.5 | Optical properties of low-dimensional excitons. a, In a van der Waals-layered bulk semiconductor, the Coulomb interaction of electron–hole pairs is screened by the dielectric environment, ε. **b**, In the monolayer limit, only the monolayer itself (ε) and the substrate (ε_s) screen the Coulomb interaction, in contrast to air (ε_air). **c**, In a monolayer of a semiconductor with anisotropic effective masses, m_a^* and m_b^*, for example in CrSBr depicted here, the excitons are effectively confined to one dimension. **d-f**, Schematic absorption spectra of semiconductors in three, two and one dimension(s). Exciton states manifest themselves as sharp peaks in the absorption, α, below the single-particle bandgap, E_gap. As a result of increasing spatial confinement of the electron–hole pairs the binding energy, E_b, inversely scales with the dimensionality of the system. The schematic absorption spectra neglecting Coulomb correlations are shown as dashed lines.

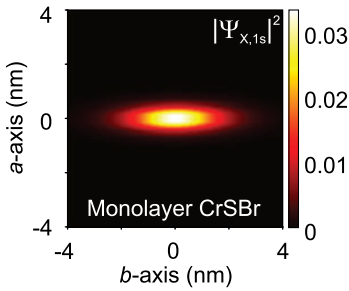

Figure 2.6 | Highly anisotropic excitons in CrSBr. Calculated real-space probability density function $|\Psi_{X,1s}|^2$ of the excitonic 1s ground state in a CrSBr monolayer (see Section 5.4 and Appendix B.2 for details on the calculation). The extremely anisotropic wavefunction is in good agreement with calculations in the literature based on the Bethe-Salpeter equations[19].

anisotropy results in small transition dipole matrix elements along the axis featuring the larger effective mass and, thus, strongly attenuated absorption for light polarised along that direction. Consequently, in the example of CrSBr, efficient photoexcitation of excitons requires light polarised along the *b*-axis. Interestingly, in stark contrast to three- and two-dimensional systems, the continuum absorption in a one-dimensional semiconductor is suppressed, when Coulomb correlations are considered[94].

Conclusion: CrSBr as a unique quantum material. In summary, CrSBr stands out as a fascinating quantum material, showcasing a diverse range of correlations, including magnetic order and tightly bound excitons. Moreover, in CrSBr, quasiparticles are intricately interconnected, giving rise to a plethora of quantum phenomena, such as spin-phonon and exciton-magnon coupling as well as strong light-matter interaction. Notably, the capability of CrSBr to be thinned down to a monolayer, combined with its extreme electronic anisotropy, positions it as an ideal model system for studying *intrinsically* one-dimensional excitons – a realm previously confined to artificially assembled structures such as quantum wires[20], nanotubes[21,22], or moiré superlattices[23]. The unparalleled convergence of these characteristics establishes CrSBr as an exceptionally promising system for solid-state research and future quantum technology.

The ultrafast dynamics of excitons in CrSBr play a central role in these endeavours, but have not yet been explored. The exciton binding energies in CrSBr have been reported to amount to $\sim 700\,\mathrm{meV}$ and $\sim 100\,\mathrm{meV}$ in monolayers and bulk, respectively[19]. Owing to the corresponding large oscillator strengths, exciton lifetimes

on the femtosecond timescale are expected[14,36]. Furthermore, the micron-scale lateral sizes of exfoliated monolayers call for a *microscopic* probe technique featuring femtosecond temporal resolution to conclusively investigate the ultrafast dynamics in atomically thin CrSBr.

In the following, I will describe the sophisticated, state-of-the-art experimental approach we utilised to reveal the femtosecond dynamics of paramagnetic excitons in bulk and monolayer CrSBr.

Chapter 3

Ultrafast field-resolved terahertz polarisation nanoscopy

CrSBr presents an unprecedented environment for the investigation of magnetically ordered quasi-one-dimensional excitons in a *bulk* semiconductor. The one-dimensional character will be even more pronounced in monolayers of CrSBr owing to the absence of interlayer coupling. The optical properties of excitons including binding energies and oscillator strengths are often determined by the experimental schemes of photoluminescence[11,19,27,95–97], linear absorption[11] and reflectance[13,24,97] measurements. However, these interband techniques can solely probe "bright" excitonic states within the light cone, while "dark" excitons, which require spin-flip and/or momentum transfer, remain inaccessible[98]. In contrast, *intra*band approaches such as terahertz polarisation probing[56,57,99,100] can directly trace all excitons, independently of interband selection rules. As a consequence of the diffraction limit[47], the large terahertz wavelengths on the order of 300 µm limit the spatial resolution of far-field techniques to scales far exceeding the typical lateral dimension of exfoliated CrSBr monolayers ($\sim 10\,\mu m \times 10\,\mu m$).

Therefore, to study atomically thin samples with terahertz probe pulses, subwavelength resolution is mandatory. Near-field microscopy[48] has marked a breakthrough in overcoming the diffraction limit by confining light with aperture-probes[101], which facilitated spatial resolution down to 20 nm (Reference 102). However, extending aperture-type near-field microscopy to the (multi-)terahertz regime has proven to

be difficult because of strong attenuation of terahertz waves in the employed fibres and the low-frequency cut-off of metallised waveguides[103]. Meanwhile, scattering-type near-field optical microscopy (s-SNOM)[49–53] is readily compatible with terahertz waves[104], as in this technique, far-field waves are focused onto a metallic tip and the scattered radiation is detected. In a pioneering study, simultaneous spatial resolution of 10 nm and ultrafast, sub-cycle temporal precision of 10 fs have been achieved by field-resolved detection of scattered mid-infrared pulses[105]. Over the past decade, s-SNOM at low terahertz frequencies has proven as an elegant method to probe the nanoscopic, femtosecond dynamics of low-energy excitations and correlations in micron-scale samples of modern quantum materials[54–57,106].

In the following sections, I will shortly discuss the functional principle of s-SNOM as well as the underlying experimental and theoretical concepts required to conduct conclusive studies of nanoscale dynamics (Section 3.1). Subsequently, I will review the recently introduced technique of ultrafast terahertz polarisation nanoscopy (Section 3.2) and the experimental setup, which enables the generation of ultrashort phase-locked terahertz probe pulses (Section 3.3) as well as phase-resolved detection (Section 3.4).

3.1 Scattering-type scanning near-field optical microscopy

Basic concept. The fundamental idea behind s-SNOM is to couple electromagnetic waves to the tip of an atomic force microscope, localising the light to strongly sub-wavelength scales and enhancing the electric field at the tip apex (Figure 3.1a). As the evanescent field interacts with the sample in a volume determined by the radius of curvature of the tip apex, information about the nanoscopic sample properties is encoded in the radiation scattered into the far field. In typical near-field experiments, either the scattered intensity or electric field is detected.

Background suppression by Fourier analysis. Near fields in s-SNOM are usually confined to a volume smaller than $\sim (100\,\mathrm{nm})^3$ (References 105 and 107), which, for terahertz waves, is ten orders of magnitude smaller than the diffraction

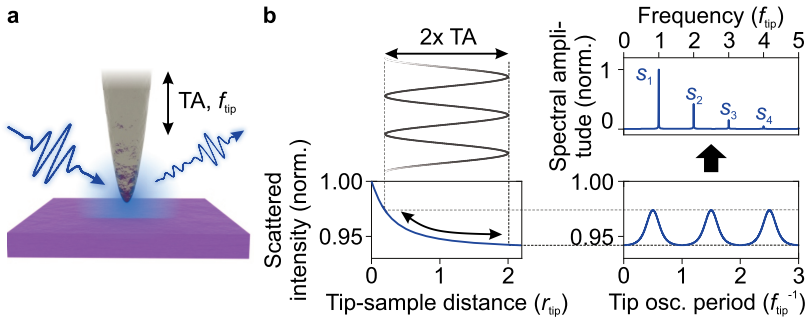

Figure 3.1 | Functional principle of scattering-type scanning near-field optical microscopy (s-SNOM) a, Sketch of the tip-sample system. An electromagnetic wave (left, blue) is coupled to the apex of a metallic tip oscillating with a frequency, f_{tip}, at an amplitude, TA. As a result of the near-field interaction (blue halo), another lightwave (blue, right) encoding nanoscopic properties of the sample is scattered into the far field. **b**, Origin of the signal harmonics. The scattered intensity (bottom left) scales nonlinearly with the tip-sample distance, given in units of the tip radius, r_{tip}. The sinusoidal modulation of the tip-sample distance then leads to bursts in the scattered intensity (bottom right). The spectral amplitude of the scattered signal contains Fourier components, $s_{\mathrm{n}} = |E_n|$, at harmonics of the tip oscillation frequency, f_{tip} (top right), which are used to separate the nanoscopic near-field and far-field contributions.

limit. Owing to the conflicting nature of detecting radiation originating from such extreme sub-wavelength scales in the *far field*, a key challenge of s-SNOM is to isolate the near-field contribution by eliminating the unwanted far-field background from reflections from the cantilever or the sample surface. In s-SNOM experiments, the far-field share of the signal is typically suppressed by a combination of operating the microscope in tapping mode and Fourier analysis: Since the scattering efficiency *nonlinearly* depends on the distance between tip and sample (Figure 3.1b), the sinusoidal modulation of the tip-sample distance with amplitude TA translates into an anharmonic scattering response, containing harmonics at the n-th harmonic of the oscillation frequency, f_{tip}. Using lock-in detection, the corresponding Fourier components, E_n, can be extracted. For increasing demodulation order, n, the contribution of the far-field background to the signal decreases[108]. Background

suppression is further enhanced when one analyses the pump-induced change of the scattered field in optical-pump/terahertz probe measurements[56]. Consequently, s-SNOM provides strongly sub-wavelength spatial resolution, which is dominated by the radius of curvature of the tip apex and only weakly depends on the wavelength of the probe radiation[107].

Analytical modelling of the scattering. To extract the nanoscopic properties and dynamics of the probed sample from the near-field response, a detailed understanding of the complex interplay of confined electric fields, the sample and the nanoscale tip geometry[107,109] is required, calling for accurate modelling of the nanoscopic light-matter interaction. In the last decades, significant advances have been made in both numerical and analytical modelling of the scattering mechanism and intricate tip-sample interaction[108,110–113].

The common ansatz of these models is to express the scattered field strength, E_{scat}, as a function of the effective dipole moment, p_{eff} of the tip-sample system, which is described by its effective polarisability, α_{eff}: $E_{\mathrm{scat}} \propto p_{\mathrm{eff}} = \alpha_{\mathrm{eff}} E_0$. The external electric field at the tip apex, E_0, is given by the incident electric field, E_{in}, and the part reflected off the sample surface, $r_p E_{\mathrm{in}}$ quantified by the Fresnel reflection coefficient for p-polarised light (Figure 3.2a). Similarly, the scattered field can either propagate directly into the far field or indirectly via a reflection from the surface. Thus, the detected scattered field is expressed as[113]:

$$E_{\mathrm{scat}} \propto (1 + r_{\mathrm{p}})^2 \alpha_{\mathrm{eff}} E_{\mathrm{in}}. \tag{3.1}$$

As a consequence of Equation (3.1), within the framework of analytical models, it is sufficient to determine the effective polarisability of the tip-sample system, α_{eff}, to predict the scattered electric field at the detector.

The earliest approach to analytically grasp the effective polarisability was the point-dipole model[110–112], which was proposed in the 1990s. Its straightforward approach of approximating the tip-sample system as two point dipoles in a uniform, purely vertical electric field, has proved as a useful tool to qualitatively understand features in near-field spectroscopy.

The finite-dipole model. The finite-dipole model[113] provides a more realistic analytical approach of modelling the tip-sample geometry and interaction (Figure 3.2). The tip apex is approximated by a perfectly conducting spheroid with a length, $2L$. When an incident electric field polarizes the tip (Figure 3.2a), the resulting dipole is simplified to two monopoles Q_0 and $-Q_0$ positioned at the centres of circles with radius r_{tip}, located at the ends of the spheroid (Figure 3.2b). The model assumes that the tip-sample interaction is dominated by the lower charge Q_0, which induces a mirror charge Q_0' in the sample. In turn, Q_0' induces a charge density in the spheroid, described by charges Q_{i} and $-Q_{\mathrm{i}}$ in the tip. As the distance of $-Q_{\mathrm{i}}$ to the sample is larger than that of Q_{i}, its contribution to the tip-sample interaction is expected to be weak. Thus, $-Q_{\mathrm{i}}$ is distributed uniformly across the spheroid to ensure charge neutrality. Finally, the induced charge Q_{i} close to the tip apex induces another image charge, Q_{i}', in the sample.

The effective dipole moment of the tip spheroid is given by $p_{\mathrm{eff}} = p_0 + p_{\mathrm{i}}$, where $p_0 = 2Q_0L$ is the dipole moment directly induced by the external field and p_{i} the dipole moment invoked by the near-field tip-sample interaction. The effective polarisability of the spheroid-sample system, $\alpha_{\mathrm{eff}}^{\mathrm{FDM}}$, can be determined from p_{eff} by quantifying the involved charges following Reference 113:

$$\alpha_{\mathrm{eff}}^{\mathrm{FDM}} = \frac{p_{\mathrm{eff}}}{E_{\mathrm{in}}} \propto \left(2 + \frac{\beta\left(g - \frac{r_{\mathrm{tip}}+h}{L}\right)\ln\left(\frac{4L}{4h+3r_{\mathrm{tip}}}\right)}{\ln\left(\frac{4L}{r_{\mathrm{tip}}}\right) - \beta\left(g - \frac{3r_{\mathrm{tip}}+4h}{4L}\right)\ln\left(\frac{2L}{2h+r_{\mathrm{tip}}}\right)}\right). \tag{3.2}$$

Most parameters in Equation (3.2), such as the tip-sample distance, h, the tip radius, r_{tip} and $\beta = \frac{\varepsilon_{\mathrm{s}}-1}{\varepsilon_{\mathrm{s}}+1}$, determined by the dielectric function of the sample, ε_{s}, are usually known from the experiment. The factor g describes the fraction of the induced charge actually interacting with the sample. A small imaginary part of g phenomenologically accounts for the slight phase shift between the incident field and the response of the tip, caused by the tip's finite conductivity. Accurate values for the spheroid length $2L$ and g have been determined by matching predictions of the finite-dipole model to experimental near-field responses, where $2L = 700\,\mathrm{nm}$ and $g = 0.7e^{0.06i}$ yield the best quantitative agreement[114,115].

The finite-dipole model has proven to be a powerful tool for quantitative modelling of approach curves and spectral features in the near-field response[113]. By extending

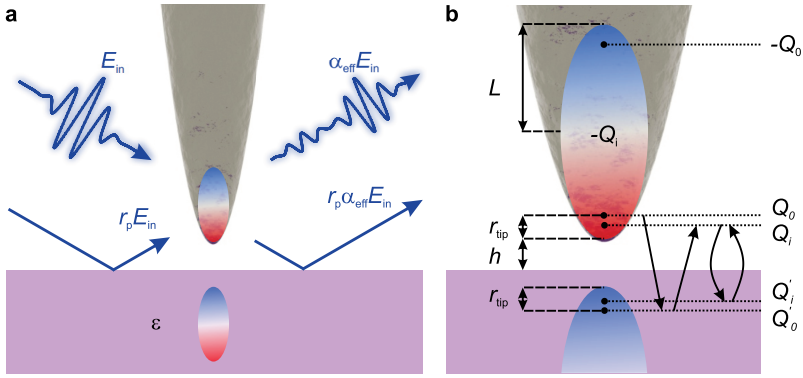

Figure 3.2 | The finite-dipole model. a, The incident electric field, E_{in}, either directly couples to the tip-sample junction or indirectly after a reflection from the sample surface, given by the Fresnel reflection coefficient for p-polarised light, r_{p}. Consequently, a polarisation approximated by a spheroid is induced in the apex of the tip. A corresponding image dipole is induced in the sample. The scattered electric field is determined by the effective polarisability of the tip-sample system, α_{eff}, dictated by the dielectric function of the sample, ε. **b**, Charge distribution at the tip apex in the finite-dipole model. The initial polarisation of the tip is approximated by two monopoles carrying charges $\pm Q_0$, respectively. The tip-sample interaction is modelled by an image charge Q_0' in the sample, which repolarises the tip, giving rise to induced charges $\pm Q_{\mathrm{i}}$ and finally, an image charge $\pm Q_{\mathrm{i}}'$ in the sample. The geometry of the system is characterised by the length of the spheroid, $2L$, the tip radius, r_{tip} and the tip-sample distance, h. Adapted from Reference 113.

the model, accurate predictions of the scattered signal of layered structures have been achieved[108,114]. Moreover, the finite-dipole model can be inverted, allowing to directly retrieve the complex-valued dielectric function of a sample from the scattering contrast via an optimisation algorithm[108].

Demodulated scattered signal. As described earlier, to suppress the far-field background, the scattered signal is demodulated at the n-th harmonic of the tip oscillation frequency (compare Figure 3.1b). Consequently, the respective Fourier components of the effective polarisability, $\alpha_{\mathrm{eff},n}$, describe the demodulated scattered electric field in the frequency domain, E_n, which is typically expressed in terms of

amplitude, s_n and phase, ϕ_n, in accordance with Equation (3.1)[113]:

$$E_n = s_n e^{i\phi_n} \propto (1 + r_p)^2 \alpha_{\mathrm{eff},n} E_{\mathrm{in}}. \tag{3.3}$$

Despite the demodulation, near-field signals can be compromised by additive backgrounds. For example, reflections from regions surrounding the sample, which exhibit a different dielectric function and, hence, r_p, are not accounted for in Equation (3.1). In a recent study, normalisation of signal harmonics, has been demonstrated to eliminate such artefacts[116]. Consequently, the exclusively local near-field response can be expressed by

$$E_{mn} = \frac{E_m}{E_n} = \frac{s_m}{s_n} e^{i(\phi_m - \phi_n)}, \tag{3.4}$$

where $m \neq n$. Furthermore, analysing the amplitude and phase of E_{mn} directly reveals dipole-active resonances in the sample[116], offering a powerful method of accessing its nanoscale dielectric function.

3.2 Terahertz polarisation nanoscopy

In this work, the ultrafast dynamics of electron–hole pairs in CrSBr is explored by means of sub-cycle polarisation nanoscopy[56,57], a recently pioneered technique based on time-resolved near-field microscopy[54,55,105,117–119] at terahertz frequencies[120–123]. The basic idea is to nonresonantly probe the polarisability of photoexcited electron–hole pairs with phase-stable electric-field waveforms coupled to the tip of a scattering-type near-field microscope. The instantaneous electric near field, E_{NF}, deflects the electron–hole pairs, inducing them to carry a dipole moment, p, which is proportional to their polarisability, α_{eh} (Figure 3.3, right). In the absence of dipole-active excitations, such as optical phonons, α_{eh} governs the nanoscopic tip-sample interaction, as shown in the previous section (Equations (3.1) and (3.3)). Thus, in a spectral probing window far from resonant quantum excitations of electron–hole pairs, α_{eh} can be retrieved by analysing the pump-induced change of the scattered waveform,

$$\Delta E \propto n_{\mathrm{eh}} \alpha_{\mathrm{eh}}. \tag{3.5}$$

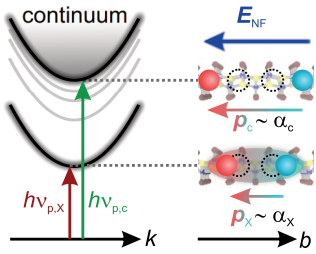

Figure 3.3 | Terahertz polarisation probing. Tunable optical pulses inject either excitons (red, $h\nu_{p,X}$) or continuum states (green, $h\nu_{p,c}$). The terahertz electric near field E_{THz} (blue) polarises the electron-hole pairs with polarisability α_X and α_c, respectively. The resulting dipole moment, $\boldsymbol{p}$, is imprinted in the scattered electric field.

Here, n_{eh} denotes the density of electron–hole pairs. As a consequence of Equation (3.5), by analysing ΔE one can explore the binding state, density and dynamics of the photoexcited electron–hole pairs.

Terahertz field transients have proven to be an exceptionally well-suited probe for polarisation nanoscopy, as their frequency is more than an order of magnitude below even low-energy quantum transitions, such as the Lyman-like 1s-2p transition of excitons in TMDC monolayers[14,46]. Therefore, the terahertz electric field directly couples to the polarisability of all electron–hole pairs, regardless of interband selection rules, enabling to study the dynamics of, for example, spin- or momentum-forbidden "dark" excitons as well as continuum states. In addition, the exact temporal evolution of phase-locked terahertz waveforms can be routinely recorded by means of electro-optic sampling[44,45,124]. Consequently, by deciphering the polarisability of the sample from the sampled field transients, one can resolve the ultrafast dynamics of photoexcited electron–hole pairs with *sub-cycle* precision and femtosecond temporal resolution. Lastly, the detection of the entire terahertz waveform provides direct access to the spectral amplitude and absolute phase of the scattered pulses, enabling ultrafast time-domain spectroscopy.

In CrSBr, the individual layers are effectively electronically decoupled[19], such that the in-plane polarisability far exceeds the out-of-plane one. Seminal studies have shown that, although the incident electric waveforms are polarised out of plane, as a result of the confinement to the tip apex, scattering-type near-field techniques are also sensitive to the *in-plane* polarisation[56,57]. Therefore, by resonantly photoexciting selected electronic states in CrSBr with femtosecond laser pulses, one may distinguish highly polarisable continuum states from excitons, whose polarisability is quenched

by Coulomb attraction (Figure 3.3) Moreover, by tracing the scattered terahertz field as a function of the delay time with respect to the optical pump pulses the ultrafast dynamics of electron–hole pairs, including relaxation, Coulomb binding and recombination can be revealed.

Setup for ultrafast optical pump/terahertz probe nanoscopy. As an integral part of this work, I designed and built the optical pump/terahertz probe experimental setup proposed above, which is sketched in Figure 3.4. The setup can be divided into three functional branches, all of which are driven by a commercial high-power ytterbium fibre laser providing pulses with a centre wavelength of 1030 nm, pulse duration of 140 fs and a pulse energy of 15 µJ at a repetition rate of 4 MHz. To guarantee optimal long-term stability and signal-to-noise ratios, the beam pointing of the laser output is actively stabilised (Appendix A).

Widely tunable optical pump pulses are generated in a home-built noncollinear optical parametric amplifier (NOPA, left panel, Chapter 4). The intensity of the pulses is modulated by an acousto-optic modulator (AOM) for differential pump-probe measurements, before the pump light is coupled into a commercial near-field optical microscope. Phase-locked terahertz pulses acting as ultrafast near-field probe are generated by optical rectification in a gallium phosphide crystal (Section 3.3). A hole in the collimating parabolic mirror separates the near-infrared generation pulses from the terahertz pulses. Residual near-infrared radiation is absorbed in a germanium wafer placed under Brewster's angle. The terahertz waveforms are transmitted and subsequently collinearly overlapped with the optical excitation pulses via reflection from a window coated with indium tin oxide. The third branch directly provides ultrashort near-infrared laser pulses serving as gate for the phase-resolved detection of the scattered terahertz field transients by means of electro-optic sampling (EOS, Section 3.4). To avoid water vapour absorption, the entire terahertz beam path is purged with dry nitrogen.

Both the optical pump and the terahertz probe pulses can be delayed with femtosecond precision by optical delay lines, enabling different types of optical pump/terahertz probe measurements to be performed. By varying the pump delay, t_p, while tracking a certain instant of the scattered terahertz transient ($t_\mathrm{EOS} = \mathrm{const}$), one can unveil pump-induced dynamics. Moreover, varying the EOS delay, t_EOS,

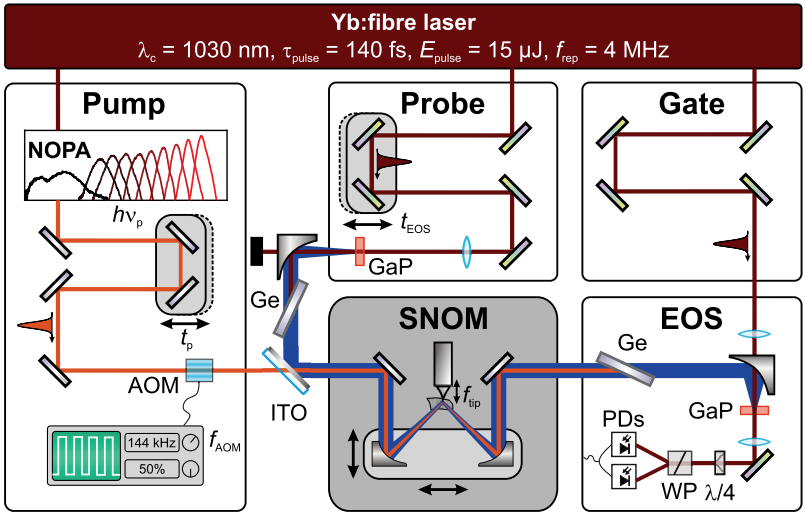

Figure 3.4 | Ultrafast terahertz near-field spectroscopy setup. An ytterbium fibre laser (dark red box) provides femtosecond near-infrared pulses, which are used to generate tunable optical pump pulses (orange) in a noncollinear optical parametric amplifier (NOPA, left), terahertz probe pulses (blue) and ultrashort gate pulses for electro-optic detection (right). The optical pump pulses are modulated by an acousto-optic modulator (AOM) at frequency f_{AOM} for differential measurements. Intense, phase-locked terahertz probe pulses are generated in a gallium phosphide crystal (GaP). A germanium wafer (Ge) filters the residual generation light. The pump and probe pulses are overlapped via transmission through and reflection from an indium tin oxide-coated window (ITO), respectively. An adjustable parabolic mirror couples the pulses to the tip apex in the near-field microscope (SNOM). The terahertz pulses scattered from the tip oscillating at frequency f_{tip} are directed into the setup for electro-optic sampling (EOS), while any residual excitation light is blocked by another germanium wafer. When the terahertz and gate pulses are overlapped in a gallium phosphide detector crystal (GaP), the scattered terahertz waveform can be electro-optically detected. Both the optical pump and the terahertz probe pulses can be delayed using translation stages (t_{p}, t_{EOS}). $\lambda/4$, quarter-wave plate; WP, Wollaston prism; PDs, balanced photodiodes.

allows for resolving the time evolution of the terahertz waveform, giving access to both its spectral amplitude and absolute phase. In this way, one can record the sub-cycle polarisation response of systems in extreme nonequilibrium, which is an elegant method to, for example, directly trace ultrafast dynamics of photo-induced carriers[42,105] or interlayer tunnelling in TMDC heterobilayers[56,64].

Coupling the laser pulses to the tip of an atomic force microscope, allows one to overcome the diffraction limit by orders of magnitude and, thus, investigate samples with (sub-)micron-scale lateral dimensions, such as CrSBr monolayers. Moreover, the experimental setup provides a unique combination of ultrafast, sub-cycle nanoscopy and femtosecond optical excitation, which is tunable across the majority of the visible into the near-infrared spectral domain. The wide range of available excitation wavelengths enables the selective injection of electronic states in CrSBr from the excitonic 1s ground state to continuum states above the single-particle bandgap and unambiguous tracking of their ultrafast dynamics. By fine-tuning the pump photon energy, one may even unveil excitonic states in CrSBr, which originate from lower valence bands and have only been theoretically predicted so far[19], making this scheme a powerful tool for investigation of novel quantum materials.

In the following, I will describe the functional building blocks of the ultrafast nanoscopy setup step-by-step, starting with the generation and phase-resolved detection of phase-locked terahertz probe waveforms.

3.3 Generation of broadband phase-stable terahertz probe pulses

Linear optics describes light-matter interaction based on the assumption that the polarisation in a medium is proportional to the external electric field. This approximation, in which electrons are deflected in a parabolic potential, accurately quantifies phenomena like reflection, transmission and refraction for small electric field strengths. However, at high intensities, which are readily achieved with femtosecond laser pulses, the harmonic approximation collapses. Consequently, the linear dependence of the polarisation, $\boldsymbol{P}$, on the incident electric field, $\boldsymbol{E}$, must be

extended by a series expansion[125],

$$\boldsymbol{P}(t) = \varepsilon_0 \sum_k \chi^{(k)} \boldsymbol{E}^k(t) = \sum_k \boldsymbol{P}^{(k)}, \tag{3.6}$$

where $\chi^{(k)}$ denotes the optical susceptibility of k-th order and ε_0 the vacuum permittivity. The *nonlinear* interaction of intense lightwaves with matter gives rise to a plethora of fascinating phenomena[125], many of which, including second harmonic generation, self-phase modulation, and difference frequency generation, will be exploited throughout this thesis.

Second-order nonlinear effects, which originate from the term associated with $\chi^{(2)}$ in Equation (3.6), can be easily grasped in the following way: In response to two driving fields $\boldsymbol{E}_{\mathrm{mix}} = \boldsymbol{E}_1 \mathrm{e}^{-\mathrm{i}\omega_1 t} + \boldsymbol{E}_2 \mathrm{e}^{-\mathrm{i}\omega_2 t} + \mathrm{c.c.}$, the second-order component of the polarisation, $\boldsymbol{P}^{(2)}$, of a noncentrosymmetric medium gives rise to new Fourier components:

$$\begin{aligned}
\boldsymbol{P}^{(2)}(t) &= \varepsilon_0 \chi^{(2)} \boldsymbol{E}_{\mathrm{mix}}^2 \\
&= \varepsilon_0 \chi^{(2)} \left(\boldsymbol{E}_1 \mathrm{e}^{-\mathrm{i}\omega_1 t} + \boldsymbol{E}_2 \mathrm{e}^{-\mathrm{i}\omega_2 t} + \mathrm{c.c.} \right) \\
&= \varepsilon_0 \chi^{(2)} \Big(\boldsymbol{E}_1 \boldsymbol{E}_1^* + \boldsymbol{E}_2 \boldsymbol{E}_2^* + \boldsymbol{E}_1 \boldsymbol{E}_1 \mathrm{e}^{-2\mathrm{i}\omega_1 t} + \boldsymbol{E}_2 \boldsymbol{E}_2 \mathrm{e}^{-2\mathrm{i}\omega_2 t} \\
&\qquad + 2\boldsymbol{E}_1 \boldsymbol{E}_2 \mathrm{e}^{-\mathrm{i}(\omega_1+\omega_2)t} + 2\boldsymbol{E}_1 \boldsymbol{E}_2^* \mathrm{e}^{-\mathrm{i}(\omega_1-\omega_2)t} + \mathrm{c.c.} \Big)
\end{aligned} \tag{3.7}$$

Equation (3.7) directly illustrates the generation of the second harmonic, $2\omega_{1/2}$, the sum frequency, $\omega_1 + \omega_2$ and the difference frequency, $\omega_1 - \omega_2$. In the photon picture of difference frequency mixing (Figure 3.5a), one photon (ω_2) stimulates the annihilation of another incident photon (ω_1). Simultaneously, a third photon at their beat frequency ($\omega_3 = \omega_1 - \omega_2$) is created.

Optical rectification. For our sub-cycle terahertz nanoscopy experiment, we exploit optical rectification to generate ultrashort, phase-locked terahertz field transients. In this process, a single, ultrashort laser pulse provides both driving fields. The beating of the nonlinear polarisation of all Fourier component pairs of the broadband laser spectrum gives rise to a (multi-)terahertz waveform (Figure 3.5b). Importantly, all shot-to-shot phase fluctuations of the incident pulse train cancel in

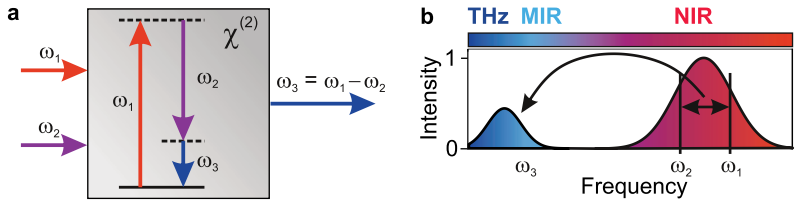

Figure 3.5 | Concept of difference frequency generation and optical rectification. **a**, Difference frequency generation in a $\chi^{(2)}$ medium. Two Fourier components of the frequencies ω_1 and ω_2 can generate a new Fourier component of the polarisation at their difference frequency $\omega_3 = \omega_1 - \omega_2$ in a medium with broken inversion symmetry. **b**, Optical rectification. Also within a single, broadband laser pulse every pair of two frequency components can drive a nonlinear polarisation at their beat frequency, enabling broadband emission in the terahertz and mid-infrared spectral domain.

the mixing process. Therefore, the generated terahertz field transients are passively phase-locked, giving rise to a series of identical field transients.

The centre frequency and bandwidth of the terahertz spectrum are, on the one hand, governed by the bandwidth of the fundamental laser pulse, whose frequency spectrum is typically located in the near-infrared range. On the other hand, efficient generation of Fourier components at ω_3 over the entire crystal length, L, requires the phase matching condition,

$$\Delta k = k(\omega_1) - k(\omega_2) - k(\omega_3) \stackrel{!}{=} 0, \tag{3.8}$$

to be fulfilled, where $k(\omega_i) = \frac{\omega_i n(\omega_i)}{c}$, n is the refractive index and c the speed of light in vacuum. One can show that for $\omega_1, \omega_2 \gg \omega_3$ Equation 3.8 holds, when the group velocity of the generation light is equal to the phase velocity of the terahertz wave[125]. A more rigorous analysis of the phase matching condition yields a quantitative prediction of the generated terahertz field, E_{THz} (Reference 44):

$$\left|\tilde{E}_{\mathrm{THz}}(L, \omega_{\mathrm{THz}})\right|^2 \propto I_{\mathrm{NIR}}^2 d_{\mathrm{eff}}^2 \underbrace{L^2 \mathrm{sinc}^2\left(\frac{\Delta k(\omega, \omega_{\mathrm{THz}})L}{2}\right)}_{\text{phase matching factor}}. \tag{3.9}$$

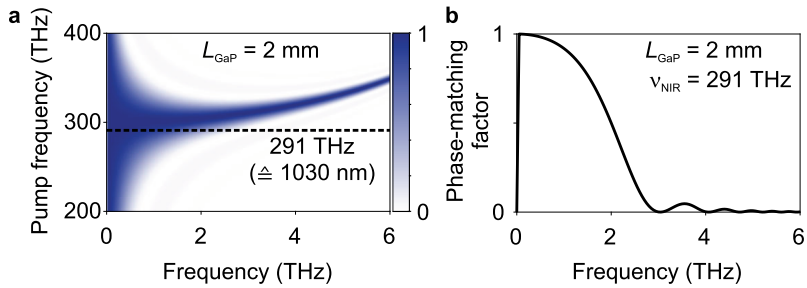

Figure 3.6 | Phase matching in gallium phosphide. a, False-color plot of the phase matching factor in gallium phosphide with a thickness, $L_{\mathrm{GaP}} = 2\,\mathrm{mm}$. The centre frequency of the ytterbium-based laser of 291 THz is indicated with a dashed line. **b**, Phase matching factor for 2 mm-thick gallium phosphide as a function of the terahertz frequency for a pump frequency, $\nu_{\mathrm{NIR}} = 291\,\mathrm{THz}$. For the calculation, the Sellmeier coefficients given in Reference 126 were used.

Here, I_{NIR} denotes the near-infrared intensity, d_{eff} the nonlinear coefficient and $\mathrm{sinc}(x)$ the cardinal sine function. The term $L^2\mathrm{sinc}^2(...)$ in Equation (3.9) is commonly known as the phase matching factor quantifying the conversion efficiency for a given crystal length and pair of near-infrared and terahertz frequencies, ω and ω_{THz}, respectively.

The high-power near-infrared laser (centre wavelength, 1030 nm, pulse duration, 140 fs) used in this work provides high intensities for efficient terahertz generation. Simultaneously, its high repetition rate of 4 MHz far exceeds the typical tip oscillation frequencies in s-SNOM, which are on the order of 100 kHz, therefore facilitating the required demodulation at harmonics of the tapping frequency. As nonlinear medium, we choose a gallium phosphide crystal (thickness, 2 mm) cut in the (110)-plane, since it allows for broadband phase matching at our laser frequency of 291 THz (Figure 3.6). Importantly, as gallium phosphide combines a large nonlinear coefficient, d_{eff}, with a high damage threshold[127], it is ideally suited for our high-power application.

The terahertz probe pulses are generated by focusing the near-infrared laser pulses featuring a pulse energy of 8 µJ into the gallium phosphide crystal. For a beam diameter in the crystal of approximately 300 µm (full width at half maximum, FWHM, of the intensity), the laser field drives the nonlinear mixing process with an

intensity of 80 GW cm^{-2}. At higher intensities, two-photon absorption in the gallium phosphide crystal results in the generation of a free-carrier plasma, which reflects the generated terahertz radiation. Consequently, a decrease of the generated terahertz power is observed, when the intensity is increased above 80 GW cm^{-2}. The highest achievable terahertz pulse energy amounts to 560 pJ, corresponding to an average power of 2.2 mW.

3.4 Phase-resolved detection

Accomplishing sub-cycle resolution in our s-SNOM experiment calls for monitoring the exact temporal evolution of the terahertz field transients. To this end, we perform electro-optic sampling[44,45,124], which acts like an "oscilloscope for light". Femtosecond gate pulses, directly taken from the output of the ytterbium fibre laser, are spatially overlapped with the terahertz pulses in a nonlinear detection crystal. As the gate pulses (pulse duration, 140 fs) are much shorter than an oscillation period of the terahertz transients ($\sim$ 1000 fs), they can be used to sample the waveforms electro-optically (Figure 3.7a). In the nonlinear crystal, the terahertz electric field induces a birefringence due to the Pockels effect. This process can alternatively be interpreted as frequency mixing of gate and terahertz waves, giving rise to near-infrared photons, which are red- or blue-shifted by the terahertz frequency and polarised perpendicular to the incident gate photons[45,128,129]. In both descriptions, the instantaneous terahertz field strength is imprinted in the polarisation state of the gate pulses, which changes from linear to elliptical in the presence of the terahertz field (Figure 3.7b). With the help of a quarter-wave plate, a Wollaston prism and two balanced photodiodes, the gate polarisation and, consequently, terahertz field, can be read out with superior signal-to-noise ratios close to the shot noise limit. Varying the electro-optic delay time (EOS time), t_{EOS}, between terahertz and gate pulses, then allows us to stroboscopically sample the terahertz waveform.

In this work, the gate pulses are directly provided by the near-infrared laser and have a duration of 140 fs. When we focus the gate and the terahertz pulses into a gallium phosphide detector crystal (thickness, 2 mm) and scan t_{EOS} via an optical delay line, we receive the waveform depicted in Figure 3.8a. The field transient consists of two prominent oscillation half cycles peaking at field strengths

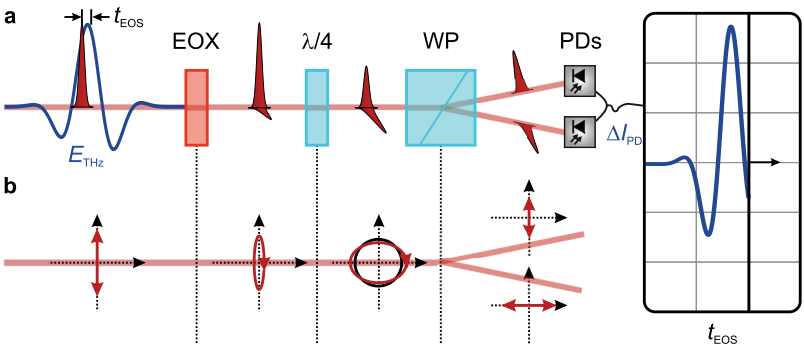

Figure 3.7 | Electro-optic sampling. **a**, Experimental setup for electro-optic detection of phase-stable terahertz waveforms. Terahertz (blue) and gate pulses (red) are spatially overlapped in an electro-optic crystal (EOX). The instantaneous electric field of the terahertz transient induces a birefringence changing the polarisation of the gate pulse from linear to elliptical. The gate pulses pass a quarter-wave plate ($\lambda/4$) and are split into their horizontal and vertical polarised parts, respectively, by a Wollaston prism (WP). The instantaneous terahertz field strength at delay time, t_{EOS}, is encoded in the differential current, ΔI_{PD}, of two balanced photodiodes (PDs). **b**, Polarisation states of the gate pulse after each optical component.

of $\pm 13\,\mathrm{kV\,cm^{-1}}$, respectively, framed by much weaker oscillations of the electric field. As each individual gate pulse samples only a small temporal window of the terahertz waveform and electro-optic measurements are typically averaged over millions of laser pulses, the observation of an electro-optic signal is in itself a proof of the phase stability of the terahertz pulses.

By Fourier transforming the terahertz waveform, we obtain its spectral amplitude and *absolute* phase, which are shown in Figure 3.8b. The broadband amplitude spectrum peaks at 1.3 THz and features Fourier components larger than 10% of the maximum amplitude spanning 0.3 THz to 2.6 THz. In this range, the shape of the spectral phase is approximately parabolic, indicating a slight chirp of the terahertz pulses caused by the dispersion in the gallium phosphide crystal. Note, that the bandwidth towards high frequencies is limited by the phase matching condition (Figure 3.6b). In contrast, the low-frequency cut-off is caused by two factors: First, the electric field emitted by a dipole scales as ω^2, strongly suppressing the emission

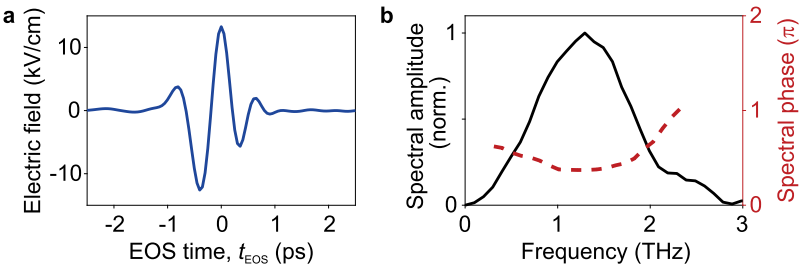

Figure 3.8 | Ultrashort terahertz probe pulses. a, Electro-optically recorded far-field terahertz probe waveform generated in a gallium phosphide crystal with a thickness of 2 mm, corrected for the detector response (see Appendix C.2). **b**, Corresponding spectral amplitude (black solid line). The spectral phase (red dashed line) is depicted at frequencies, where the amplitude exceeds 10% of the maximal amplitude.

efficiency of low frequencies. Furthermore, the strong diffraction of large wavelengths results in only fractions of the generated radiation being collected by the imaging optics.

Conclusion: A new sub-cycle terahertz nanoscopy setup. In conclusion, in this chapter we discussed the experimental foundations and theoretical framework of near-field microscopy, including an analytical model of the light-matter interaction at the nanoscopic tip apex. Furthermore, terahertz polarisation nanoscopy was introduced as a technique to directly probe the ultrafast dynamics of electron–hole pairs in semiconductor samples with micron-scale lateral dimensions, down to the atomically thin limit. I further presented a new, versatile ultrafast near-field nanoscopy setup, which provides intense, broadband and phase-stable terahertz probe pulses that are coupled to the apex of a tip in a commercial near-field microscope. The terahertz electric-field waveforms, which are scattered from the tip, can be sensitively detected in a field-resolved detection scheme, allowing one to trace electron–hole pair dynamics with sub-cycle, femtosecond temporal precision. Moreover, the combination of large bandwidth and high field strengths of the terahertz probe pulses allows us to explore the sub-cycle polarisation response of systems in extreme nonequilibrium in a broad frequency window with high signal-to-noise ratios.

Chapter 4

Tunable pump pulses from a noncollinear optical parametric amplifier

Unveiling the ultrafast dynamics of electron–hole pairs in quantum materials calls for selective photoexcitation of the various accessible electronic states, ranging from the exciton 1s ground state to continuum states above the single-particle bandgap. A tunable excitation source is particularly desirable for the conclusive study of emerging material systems, such as CrSBr, whose fundamental properties such as the magnitude of the bandgap and the exciton binding energies are still under investigation[19,27,91]. Moreover, to guarantee femtosecond temporal resolution in pump-probe measurements, an *ultrafast* excitation trigger is an essential requirement. State-of-the-art mode-locked solid-state lasers routinely provide femtosecond pulses at high average powers. However, laser sources based on population inversion provide a strictly limited range of amplified wavelengths, determined by transition energies and bandwidths of the involved energy levels in the lasing medium.

In contrast, femtosecond optical parametric amplifiers (OPAs)[130,131] driven by near-infrared pump lasers have demonstrated tunability from the mid-infrared[132] to the ultraviolet[133] spectral regime. Furthermore, the broad gain bandwidth of the parametric interaction allows one to generate intense laser pulses, which are substantially shorter than the fundamental pump pulses. The combination of this flexibility and a high level of stability of femtosecond OPAs has established them as a state-of-the-art laser source for ultrafast spectroscopy. In s-SNOM experiments,

laser repetition rates far exceeding the tip oscillation frequency ($\sim 100\,\mathrm{kHz}$) are required to avoid artefacts caused by undersampling. However, the repetition rate of commercially available OPAs is typically limited to a few hundred kilohertz.

In this chapter, the fundamentals of optical parametric amplification will be shortly introduced, before the design of a home-built, dual-stage OPA operating at an exceptionally high repetition rate of 4 MHz is discussed in detail. Subsequently, the widely tunable visible and near-infrared amplified laser pulses, which will be used for femtosecond photoexcitation of electron–hole pairs in CrSBr, are characterised.

4.1 Optical parametric amplification

While amplification in laser active media is facilitated by the linear effect of stimulated emission, optical parametric amplification is a result of a *nonlinear* optical response in crystals with broken inversion symmetry. The following section will provide a brief overview of the key nonlinear optical processes employed in OPAs. A comprehensive review of the theory of optical parametric amplification can be found in References 130 and 131.

Difference frequency generation and parametric amplification. The fundamental principle of optical parametric amplification is the transfer of energy from a high-intensity laser pulse with fixed frequency, ω_p, the so-called *pump*, to a low-intensity pulse with variable frequency, ω_s, typically referred to as *signal* or *seed*. As depicted in Figure 4.1a, the physical process of parametric amplification is based on difference frequency generation, a second-order nonlinearity, which has been introduced in Section 3.3. When two intense lightwaves oscillating at frequencies ω_p and ω_s interact in a noncentrosymmetric crystal, its $\chi^{(2)}$ nonlinear response gives rise to a third, so-called *idler* wave at frequency ω_i. Describing this process from a slightly different perspective reveals the involved parametric *amplification*: Since the interaction satisfies energy conservation,

$$\hbar\omega_\mathrm{p} = \hbar\omega_\mathrm{s} + \hbar\omega_\mathrm{i}, \tag{4.1}$$

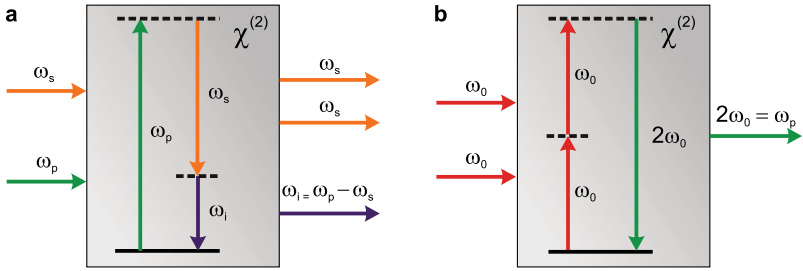

Figure 4.1 | Optical parametric amplification and second harmonic generation. a, Parametric amplification: In a $\chi^{(2)}$ medium, a photon of frequency ω_p of an intense pump pulse is converted into a signal photon of frequency ω_s and an idler photon of frequency ω_i. **b**, Second harmonic generation: Two photons of the fundamental laser frequency ω_0 generate a photon of twice the frequency, $\omega_p = 2\omega_0$, in a $\chi^{(2)}$ medium.

in a corpuscular interpretation, alongside each idler photon, an additional signal photon is created, resulting in amplification of the signal pulse. Note, that the quantum mechanical state of the nonlinear medium is the same before and after the interaction, fundamentally distinguishing the parametric process from amplification based on population inversion.

Second harmonic generation for intense pump pulses. As Equation (4.1) suggests, the pump pulses must exhibit a shorter wavelength than the signal waves. Furthermore, high pump intensities are required for an efficient nonlinear interaction. Since most high-power femtosecond lasers seeding OPAs provide *near-infrared* pulses, parametric amplification of signal pulses in the visible and near-infrared spectral range requires efficient frequency upconversion of the fundamental pulses. Typically, the $\chi^{(2)}$ nonlinear process of second harmonic generation is employed to double the fundamental photon energy, $\hbar\omega_0$ (see Figure 4.1b). In the nonlinear crystal beta-barium borate (BBO), substantial energy conversion on the order of tens of percent can be readily achieved, while the spatio-temporal shape of the fundamental pulses is maintained[134].

Supercontinuum generation for ultrabroadband seed pulses. OPAs stand out from most femtosecond laser systems for the tunability of their output wavelength, which is realised by spectrally selective amplification of an ultrabroadband seed source. The most common technique to generate suitable seed pulses is white-light generation, also known supercontinuum generation[135]: When an intense ultrashort pulse is focused into a nonlinear medium, an intricate interplay of the $\chi^{(3)}$ nonlinearities of self-focusing, self-phase modulation and self-steepening to a shock front as well as diffraction can give rise to a self-focused laser filament. Importantly, in this process, the laser spectrum is vastly broadened, spanning most of the visible and near-infrared spectral domain when generated with ytterbium-based lasers. As the pulse energy required for white-light generation is on the order of 1 µJ and the energy conversion is low, on the order of 0.1%, a supercontinuum is not suited as an intense source for pump-probe measurements. In an OPA, spectral portions of the supercontinuum can be amplified, resulting in a tunable source of intense laser pulses.

Phase matching. In dispersive media, parametric amplification is only efficient within a finite bandwidth interval and only a portion of the ultrabroadband seed spectra can be amplified. This is a consequence of the phase matching condition, which in the photon picture is equivalent to conservation of momentum,

$$\Delta\boldsymbol{k} = \boldsymbol{k}_\mathrm{p} - \boldsymbol{k}_\mathrm{s} - \boldsymbol{k}_\mathrm{i} \stackrel{!}{=} 0. \tag{4.2}$$

Here, $\boldsymbol{k}_\mathrm{p}, \boldsymbol{k}_\mathrm{s}$ and $\boldsymbol{k}_\mathrm{i}$ are the wave vectors of the pump, seed and idler waves, respectively. To achieve a vanishing phase mismatch $\Delta\boldsymbol{k}$ for pulses in distinct spectral domains, typically birefringent nonlinear media are employed. By adjusting the polarisation states of the interacting lightwaves with respect to the optic axis of the mixing crystal, the phase matching condition (4.2) can be fulfilled.

In this work, we utilise so-called type-I or eoo phase matching in the negative uniaxially birefringent crystal BBO: While the pump light is polarised along the extraordinary direction, seed and idler waves are polarised along the ordinary direction. Varying the phase matching angle θ_PM, the angle between the pump polarisation and the optic axis of the nonlinear crystal is fine-tuned for optimal phase matching (see Figure 4.2c).

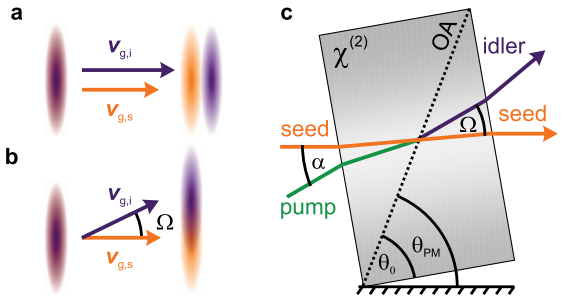

Figure 4.2 | Noncollinear amplification geometry. a, In a collinear geometry, the group velocity mismatch of signal (orange, $\boldsymbol{v}_{g,s}$) and idler pulses (purple, $\boldsymbol{v}_{g,i}$) leads to spatio-temporal walk-off. **b**, In a noncollinear geometry, the walk-off can be compensated along the propagation direction of the seed pulses. **c**, Tuning the angle between signal and pump pulses (green), α, the angle between signal and idler, Ω, can be adjusted to facilitate group velocity matching. Additionally to the cut angle, θ_0, the nonlinear mixing crystal is tilted with respect to the optic axis (OA) in order to adjust the phase matching angle, θ_{PM}.

Noncollinear geometry. In a collinear interaction geometry in a birefringent nonlinear optical medium fulfilling $\Delta\boldsymbol{k} = 0$, the group velocities of the involved pulses are given by the dispersion of the medium and are generally not equal. The group velocity mismatch between the pump and the amplified signal and idler pulses determines the energy conversion efficiency, as it restricts the effective interaction length, over which the parametric amplification occurs[130]. In contrast, the group velocity mismatch between the signal and idler pulses (Figure 4.2a) limits the phase matching bandwidth, which can be grasped as described in Reference 130: We first assume that perfect phase matching is achieved at a given signal frequency, ω_s and the corresponding idler frequency $\omega_i = \omega_p - \omega_s$. When the signal frequency increases by $\Delta\omega$, energy conservation demands that the idler frequency decreases by $\Delta\omega$. This results in a wave vector mismatch, which can in first order be approximated as

$$\Delta k = -\frac{\partial k_s}{\partial \omega_s}\Delta\omega + \frac{\partial k_i}{\partial \omega_i}\Delta\omega = \left(\frac{1}{v_{g,s}} - \frac{1}{v_{g,i}}\right)\Delta\omega, \tag{4.3}$$

where $v_{g,s}$ and $v_{g,i}$ are the group velocities of signal and idler, respectively.

As a consequence of Equation (4.3), for maximally broadband amplification, which is required to generate ultrashort signal pulses, the group velocity mismatch of the signal and idler pulses must be minimised. Using a noncollinear geometry, the walk-off of the pulses can be minimised, resulting in a substantial increase the amplified bandwidth. The idea is to introduce an angle, Ω, between the group velocity vectors of signal and idler, $\boldsymbol{v}_{\mathrm{g,s}}$ and $\boldsymbol{v}_{\mathrm{g,i}}$, respectively, such that the projection of $\boldsymbol{v}_{\mathrm{g,i}}$ on $\boldsymbol{v}_{\mathrm{s}}$ is equal to $\boldsymbol{v}_{\mathrm{g,s}}$ (Figure 4.2b),

$$|\boldsymbol{v}_{\mathrm{g,s}}| = |\boldsymbol{v}_{\mathrm{g,i}}| \cos\Omega. \tag{4.4}$$

Experimentally, one tunes the angle between pump and signal, α, such that inside the $\chi^{(2)}$ medium the angle Ω satisfies Equation (4.4) (see Figure 4.2c). As a result of the minimised walk-off, noncollinear OPAs (NOPAs) enable ultrabroadband amplification and can provide signal pulses, which are much shorter than 100 fs. Thus, NOPAs are ideal sources for tunable ultrashort photoexcitation.

4.2 Setup of the noncollinear optical parametric amplifier

In this work, I conceived and set up a high-repetition-rate NOPA acting as a tunable source of intense and ultrashort visible and near-infrared laser pulses, which can selectively prepare electron–hole pairs. This section provides a detailed description of the design choices and the optical setup exploiting the nonlinear optical phenomena described in the previous section.

Dual-stage NOPA design. Since the stability of the pump source has a significant impact on the sensitivity of a pump-probe experiment, low-noise operation is a key design consideration. In an OPA, the delicate supercontinuum generation is the main source of power fluctuation. The excess noise of the highly nonlinear seed source can be drastically reduced, when an amplification stage is driven into saturation[130]. By depleting the pump in the parametric amplification, the amplified pulse energy is less sensitive to fluctuations of the white-light seed pulses. As noncollinear propagation of the pump and seed pulses limits the effective interaction length in the nonlinear

crystal, pump depletion is realised in a second amplification stage, where already intense seed pulses are amplified with a conversion efficiency beyond 10%.

Optical setup. A detailed sketch of the compact dual-stage NOPA developed and built in this work is shown in Figure 4.3. The fundamental laser pulses (wavelength, 1030 nm; dark red lines) pass through a halfwave plate ($\lambda/2$) tuning the polarisation, such that 2 µJ out of the input pulse energy of 2.4 µJ is transmitted through the subsequent polarising beam splitter (PBS). To generate the pump pulses, the transmitted, horizontally polarised laser pulses are focused into a beta-barium borate crystal (BBO, thickness, 1 mm, cut angle, 23.4°) via a lens (L1) with a focal length, $F = 25$ cm. The generated, vertically polarised second harmonic pulses are collimated via another lens (L2) with a focal length of 15 cm and directed through an adjustable delay path. Subsequently, the pump pulses are split using a 50:50 beam splitter (BS). The transmitted and reflected pulse copies are used as pump in the first and second stage of the NOPA, respectively.

The seed pulses are generated by the portion of the fundamental laser pulses, which is reflected by the polarising beam splitter (pulse energy, 0.4 µJ). To satisfy the phase matching condition in the amplification stages, another halfwave plate rotates the polarisation of the generation light from vertical to horizontal before the pulses are focused into an yttrium aluminium garnet crystal (YAG, thickness, 5 mm) using a lens with $F = 5$ cm (L3). When the pulse energy and distance between L3 and the YAG crystal are fine-tuned, a filamentation process driven by self-focusing can be triggered, generating a supercontinuum via self-phase modulation. Note, that the supercontinuum inherits the horizontal polarisation of the generation pulse. A lens (L4) with a focal length of 3 cm collimates the strongly divergent white-light continuum, before a short-pass filter (SP) with a cut-off wavelength of 975 nm reflects the laser fundamental onto a beam dump.

In both amplification stages, the seed and pump pulses are temporally and spatially overlapped in a noncollinear geometry, sketched in the top left inset of Figure 4.3, which depicts the side view of the setup. While the seed light is steered parallel to the surface of the optical table, the pump pulses propagate under a small angle, α, with respect to the seed. By simultaneously fine-tuning α and the tilt of the BBO crystal (thickness, 5 mm; cut angle, 23.4°), group velocity matching (see Equation (4.4)) of

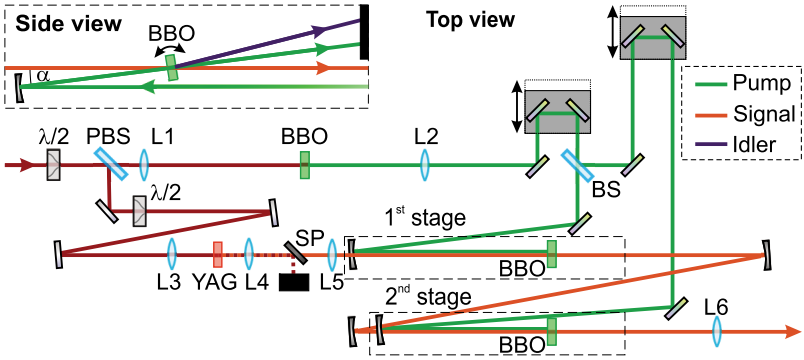

Figure 4.3 | Schematic setup of the dual-stage noncollinear optical parametric amplifier. The near-infrared input pulse (dark red) is split in a polarising beam splitter (PBS) and generates both the signal (orange) and the pump pulses (green) for the parametric amplification via supercontinuum generation in an yttrium aluminium garnet crystal (YAG) and SHG in a beta-barium borate crystal (BBO), respectively. The pump and signal pulses are noncollinearly overlapped in BBO crystals (see panel "side view") twice for parametric amplification. $\lambda/2$, halfwave plate; L1-6, lenses (focal lengths, see main text); BS, 50:50 beam splitter; SP short-pass filter (975 nm).

the seed and the generated idler pules can be achieved, enabling ultrabroadband amplification. As in our NOPA setup, pump, seed and idler propagate in different directions, the pulses needed for further application can be easily separated without additional dichroic optics, which could limit the bandwidth or introduce parasitic dispersion.

For maximal conversion efficiency, the focal diameters of pump and seed should approximately match in size. To this end, in the first stage, the seed and pump pulses are focused with a lens (L5, $F = 30\,\mathrm{cm}$) and a spherical mirror ($F = 25\,\mathrm{cm}$), respectively. In the second stage, two spherical mirrors with focal lengths of 25 cm and 20 cm, respectively, focus seed and pump into the BBO crystal. In this way, both beam waists exhibit a FWHM around 100 µm. Furthermore, the amplification of the ultrabroadband seed pulses is most efficient, when their duration is comparable to that of the pump pulses ($\sim 100\,\mathrm{fs}$). The use of lenses to collimate and focus the supercontinuum (L4 and L5) introduces a group delay dispersion (GDD) of $\sim 250\,\mathrm{fs}^2$,

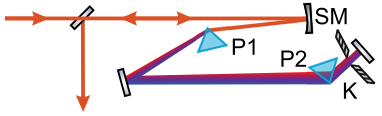

Figure 4.4 | Sketch of the employed four-prism pulse compressor. SM spherical mirror, P1, P2 fused silica prisms, K knives used to cut out flanks of the spectrum.

which is sufficient to approximately match the pulse durations. Simultaneously, utilising lenses enables a maximally compact and, hence, stable setup.

Prism compressor. To ensure that the duration of the amplified signal pulses is bandwidth-limited, they are coupled into a four-prism compressor, which introduces tunable negative GDD and thereby compensates the positive GDD caused by the transmission optics in the NOPA. Moreover, possible GDD caused by optics in later parts of the experimental setup can be pre-compensated in the compressor. A sketch of the employed compressor setup is shown in Figure 4.4: The chirped signal pulses are focused with a spherical mirror ($F = 100\,\mathrm{cm}$), before they enter the first prism, which is placed under Brewster's angle. Consequently, the pulses are spatially dispersed until they are transmitted through a second prism, again under Brewster's angle. A flat mirror placed in the Fourier plane of the signal pulses reflects the beam, such that the two prisms are passed a second time. The back reflection is aligned such that it can be coupled out by a D-shaped mirror, placed marginally below the input beam. By tuning the distance between the prisms and the propagation length of the signal pulses in the prisms, one can adjust the dispersion compensation to optimally compress the pulses. The signal pulses are optimally compressed at a prism distance of 90 cm. The passage through the first prism is fixed to $\sim 5\,\mathrm{mm}$, while for decreasing signal wavelength the passage through the second prism is increased from approximately 5 mm to 10 mm. Moreover, inserting two knives into the spatially dispersed beam, close to the focal plane, allows us to precisely cut the signal spectrum in a dispersion-free manner.

4.3 Characterisation of the amplified laser pulses

Next, we assess the performance of the home-built dual-stage NOPA operating at an exceptionally high repetition rate of 4 MHz. To this end, we characterise the pulse

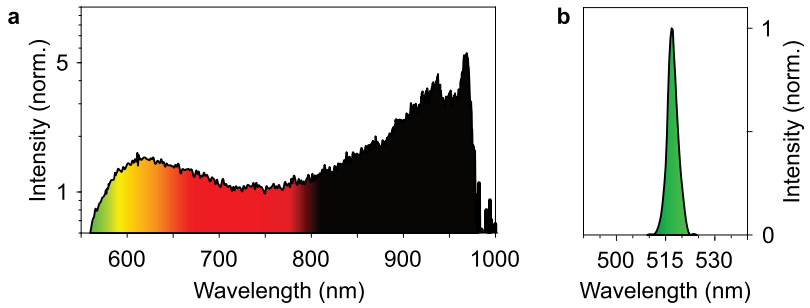

Figure 4.5 | Pump and seed spectrum. **a**, Spectral intensity of the supercontinuum generated in a YAG crystal with a thickness of 5 mm. The ultrabroadband spectrum contains frequency components from 560 nm up to 975 nm and is normalised to the intensity at 750 nm. **b**, Spectral intensity of the pump pulses generated by second harmonic generation in a BBO crystal with a thickness of 1 mm.

energies and time-integrated spectra of the pump and signal pulses before and after amplification in each stage. Lastly, the temporal intensity envelope and dispersion of the amplified signal pulses after the NOPA are retrieved.

Pump and seed pulses. Scattering-type scanning near-field experiments require that *multiple* excitation pulses are coupled into the near field within one oscillation cycle of the tip, which is typically driven at frequencies on the order of 100 kHz. While high-power laser amplifiers based on stimulated emission, operating at high repetition rates of tens of MHz are well established, commercial OPAs are typically limited to repetition rates below 1 MHz. The key factor limiting the repetition rate of an OPA is the amount of thermal stress in the amplification stages and, in particular, in the delicate supercontinuum generation[131]. There, high average optical power can cause instabilities and ultimately even catastrophic crystal damage, when the laser filament collapses as a consequence of thermal fluctuations of the refractive index.

In this work, a YAG crystal is used as nonlinear medium for the white-light generation, which has proven to provide robust supercontinua at high repetition rates[136,137]. Moreover, the exceptionally short pulse duration of our ytterbium pump laser of 140 fs further lowers the threshold pulse energy required to trigger

filamentation. As a result, we can generate stable supercontinuum seed pulses with a comparably low pulse energy of 400 nJ, which allows us to reliably operate the OPA at an outstanding repetition rate of 4 MHz. The ultrabroadband seed spectrum generated in the YAG crystal (thickness, 5 mm) is shown in Figure 4.5a. The spectral intensity spans wavelengths from 560 nm up to 975 nm and is normalised to the intensity of the local minimum at 750 nm. Note, that the spectral edge at 975 nm corresponds to the cut-off wavelength of the employed short-pass filter (see Figure 4.3). The spectrally integrated pulse energy of the white-light continuum amounts to 6 nJ.

The pump pulses for the parametric amplification are obtained by second harmonic generation of the fundamental laser pulses, using a BBO crystal with a thickness of 1 mm as $\chi^{(2)}$ medium. Its cut angle of 23.4° allows for type-I phase matching under normal incidence. By adjusting the beam waist in the BBO crystal the laser intensity is tuned such that at an input pulse energy of 2 µJ, second harmonic pulses with a pulse energy of 500 nJ are generated, providing a pump pulse energy of 250 nJ per amplification stage. The Gaussian-shaped intensity spectrum of the frequency-doubled pulses has a centre wavelength of 517 nm and a FWHM bandwidth of 3 nm, as shown in Figure 4.5b.

Amplified signal spectra. When we spatio-temporally overlap the ultrabroadband signal and intense pump pulses in a BBO crystal with a thickness of 5 mm, phase-matched frequency components of the signal spectrum are amplified via optical parametric amplification. The NOPA is designed for and operated in the so-called "magic-angle geometry", where the angle α between pump and seed is tuned, such that Equation (4.4) is satisfied. The most broadband amplification is achieved with $\alpha \approx 2.3°$. By adjusting the phase matching angle, θ_{PM}, that is, tilting the BBO crystals (see Figure 4.2c) in both amplification stages, the frequency of the amplified signal spectra can be continuously tuned from below 650 nm to 975 nm. Figure 4.6 depicts amplified spectra for centre wavelengths, $650\,\mathrm{nm} \leq \lambda_c \leq 900\,\mathrm{nm}$, recorded after the first amplification stage (Figure 4.6a) and after both stages (Figure 4.6b), respectively. The spectra are normalised to the spectral intensity of the unamplified supercontinuum at $\lambda_c = 750\,\mathrm{nm}$ (see Figure 4.5a). Note, that owing to absorption of wavelengths greater than 2.8 µm in BBO[138], efficient amplification for centre

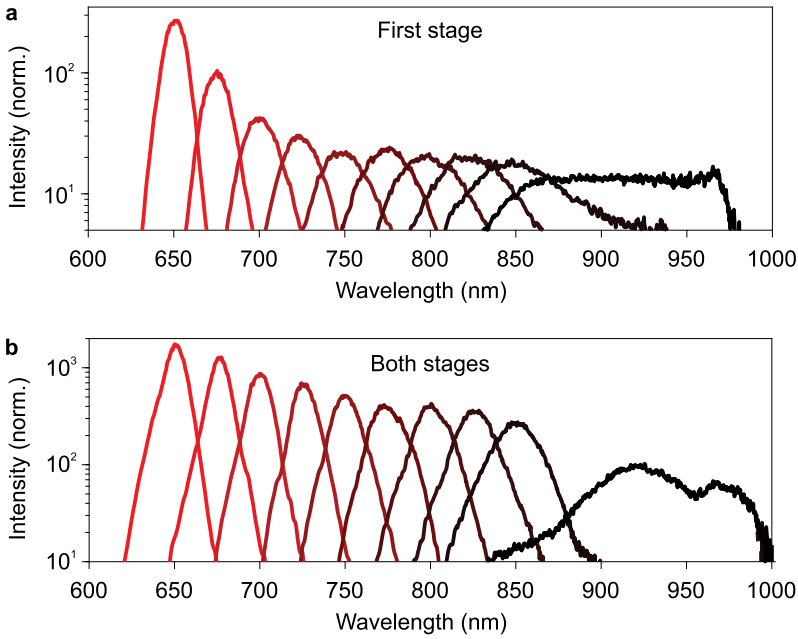

Figure 4.6 | Spectra of the amplified seed pulses. a, Spectral intensities of the amplified seed pulses after the first parametric amplification stage for centre wavelengths between 650 nm and 900 nm. **b**, Spectral intensities after both amplification stages. The spectra are normalised to the intensity of the unamplified supercontinuum at 750 nm.

wavelengths shorter than $\lambda_c = 650\,\text{nm}$ is not possible, as the corresponding idler photons are absorbed in the mixing crystal.

The peak spectral intensity decreases with increasing centre wavelength. This trend is associated with the sum of pump-signal and pump-idler group velocity mismatch, which decreases as the signal wavelength approaches the pump wavelength[130]. After the first amplification stage, the peak intensity is enhanced by a factor of approximately 20 with respect to the unamplified pulses for $700\,\text{nm} \leq \lambda_c \leq 900\,\text{nm}$, while at $\lambda_c = 650\,\text{nm}$, gain of over 200 is achieved. In the second stage, the already

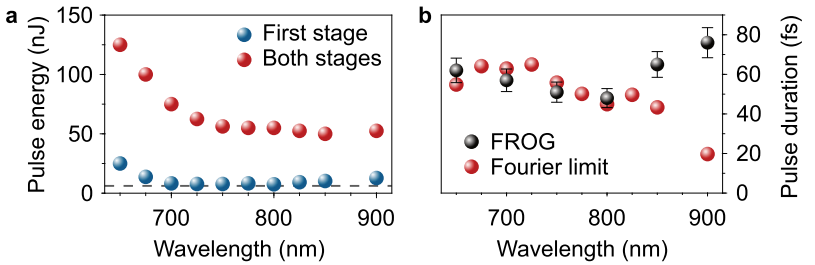

Figure 4.7 | Amplified pulse energy and pulse durations for different centre wavelengths. a, Pulse energies of the amplified signal pulses, after the first stage (blue) and both stages (red) as a function of the centre wavelength of the seed pulse. The pulse energy of the unamplified supercontinuum of 6 nJ indicated as grey dashed line was subtracted from the amplified pulse energies. **b**, Fourier-limited pulse duration of the amplified seed pulses after both stages (red) and pulse durations measured with frequency-resolved optical gating (FROG, black) as a function of the centre wavelength of the seed pulse. The error bars represent the typical variation of the reconstructed pulse durations.

intense seed pulses are amplified again, resulting in an enhancement of the peak intensity between 80 ($\lambda_c = 900\,\text{nm}$) and 1700 ($\lambda_c = 650\,\text{nm}$).

Although in each configuration only a part of the ultrabroadband white-light seed spectrum can be amplified, the initial pulse energy of the supercontinuum of 6 nJ is significantly increased in the NOPA (Figure 4.7a). After the first stage, pulse energies between 25 nJ ($\lambda_c = 650\,\text{nm}$) and 7.5 nJ ($\lambda_c = 800\,\text{nm}$) are attained. Note, that the described pulse energies are obtained after subtraction of the pulse energy of the unamplified supercontinuum. Dual-stage amplification results in signal pulse energies ranging from 50 nJ ($\lambda_c = 850\,\text{nm}$) to 125 nJ ($\lambda_c = 650\,\text{nm}$). Like the peak spectral intensity, the achieved pulse energy rises as the centre wavelength decreases as a consequence of the reduced group velocity mismatches of signal and idler with respect to the pump. Notably, in the second amplification stage, for all seed centre wavelengths, an energy conversion well beyond 10% of the pump pulse energy of 250 nJ is achieved. Therefore, the NOPA operates in the regime of pump depletion, which significantly reduces the influence of power fluctuations of the white-light continuum on the amplified pulse energy (see Appendix A, Figure A.3).

Signal bandwidth and pulse duration. The gain bandwidth of the signal pulses monotonically increases with the centre wavelength. After the first stage, the FWHM bandwidth, $\Delta\lambda$, rises from 14 nm ($\lambda_c = 650$ nm) to 60 nm ($\lambda_c = 850$ nm) and, finally, jumps to 130 nm at $\lambda_c = 900$ nm. Amplification in the second stage slightly reduces the corresponding bandwidths to 12 nm ($\lambda_c = 650$ nm) and 29 nm ($\lambda_c = 850$ nm), respectively. The most broadband spectrum ($\Delta\lambda = 99$ nm) is achieved at the longest centre wavelength, $\lambda_c = 900$ nm, which is closest to the so-called degeneracy condition, $\omega_s = \omega_i$, where the phase mismatch of signal and idler vanishes. As our NOPA is operated in group-velocity-matched geometry, in first order, the gain bandwidth is not limited by temporal walk-off of the laser pulses in the mixing crystal. However, for maximum compactness of the optical setup, transmission optics were utilised in the white-light branch (see Figure 4.3), which disperse the ultrabroadband seed pulses, resulting in a pulse duration of approximately 300 fs. Consequently, only a spectral portion of the dispersed seed pulses temporally overlaps with the pump pulses (pulse duration ~ 100 fs).

Nevertheless, the amplified spectra support Fourier-limited pulse durations, which are substantially shorter than the pump pulses (Figure 4.7b, red spheres). The respective bandwidth-limited pulse durations were obtained by Fourier transform of the signal amplitude spectra after the dual-stage NOPA (Figure 4.6b) and a subsequent fit of the temporal intensity envelope with a Gaussian. For all centre wavelengths, even after the second amplification stage, the signal pulses can be compressed to remarkably short durations (FWHM of the intensity envelope) below 70 fs. At the highest centre wavelength, $\lambda_c = 900$ nm, even pulses with a duration of 20 fs are attainable. Characterisation of the amplified signal pulses with frequency-resolved optical gating (FROG) reveals the actual pulse durations after the NOPA without external compression (Figure 4.7b, black spheres): For centre wavelengths, $\lambda_c \leq 800$ nm, the pulse durations are bandwidth-limited, ranging between 50 fs and 60 fs. Above $\lambda_c = 800$ nm, the actual, uncompressed and bandwidth-limited pulse durations exhibit an opposite trend, with the former increasing up to 76 fs ($\lambda_c = 900$ nm), while the Fourier-limited pulse duration decreases. This discrepancy is a result of residual GDD, which can be readily compensated in the prism compressor described in the previous section.

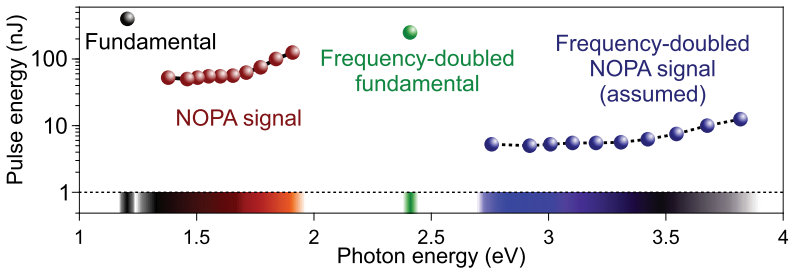

Figure 4.8 | Spectral coverage of the laser source. The presented laser source provides a wide tuning range of the photon energy across the infrared and visible spectral domain (coloured bands), which can be extended into the ultraviolet by second harmonic generation of the NOPA signal pulses. The pulse energy is plotted logarithmically against the respective centre photon energy (spheres). For the fundamental laser pulses, the pulse energy of the generation light for the supercontinuum generation is specified. For the second harmonic generation of the NOPA signal pulses, a feasible power conversion of 10% is assumed.

Conclusion: Widely tunable light pulses for pump-probe experiments. In conclusion, I have presented the concept and experimental setup of a home-built dual-stage noncollinear optical parametric amplifier (NOPA). Its exceptionally high repetition rate of 4 MHz far exceeds typical oscillation frequencies of AFM tips. As a consequence, the NOPA is seamlessly compatible with signal demodulation at harmonics of the tip tapping frequency and thus, ideally suited for use in s-SNOM experiments. Moreover, as the dual-stage NOPA design allows for pump depletion, excitation pulses with low power fluctuations are generated, promising high signal-to-noise ratios in pump-probe experiments. Owing to the broadband amplification in the noncollinear, "magic-angle" geometry, the signal pulse durations are well below 100 fs, facilitating excellent temporal resolution.

The NOPA provides widely and continuously tunable signal pulses centred at photon energies ranging from 1.3 eV to 1.9 eV (650 nm to 950 nm). Owing to the large amplified pulse energies between 50 nJ and 125 nJ, intensities sufficient to generate the second harmonic are readily achieved across the entire tuning range. This option further extends the spectrum of photon energies provided by the NOPA from 2.6 eV to 3.8 eV (Figure 4.8). Additionally, the second harmonic of the laser fundamental,

centred at 2.4 eV, is available as excitation pulse. Consequently, the presented NOPA is a powerful optical source of near-infrared, visible and ultraviolet femtosecond pulses for pump-probe studies of a plethora of quantum materials.

In the next chapter, using the described NOPA as source for ultrafast photoexcitation, we will selectively investigate the femtosecond dynamics and dielectric response of Coulomb-bound electron–hole pairs and continuum states in the van der Waals magnet CrSBr.

Chapter 5

Ultrafast exciton dynamics in atomically thin CrSBr

A unique property of the quantum material CrSBr is the strong Coulomb binding of quasi-one-dimensional electron–hole pairs, which is caused by the tight spatial confinement of carriers in the Cr–S chains and weak interlayer coupling induced by the frontier Br planes[19]. As a result, CrSBr hosts robust excitons in both its bulk and monolayer form, opening the door to applications in optoelectronics and quantum information processing, even at room temperature. However, despite their pivotal role in the investigation of semiconducting van der Waals magnets, the ultrafast dynamics of these electron-hole pairs have remained unexplored. Moreover, the potential influence of short-lived magnetic fluctuations, so-called paramagnons[31,87] on the dynamics has not been considered yet, although they have been reported to provide a scattering channel in van der Waals magnets at temperatures far above the Curie temperature[74].

In this chapter, I will describe how we combined sub-cycle terahertz polarisation spectroscopy with near-field probing and a widely tunable source for photoexcitation to explore the ultrafast dynamics and dielectric response of paramagnetic excitons in bulk and monolayer CrSBr. The discussion in the remainder of this chapter follows a manuscript, which is currently under review. The figures in this chapter are adapted from this manuscript.

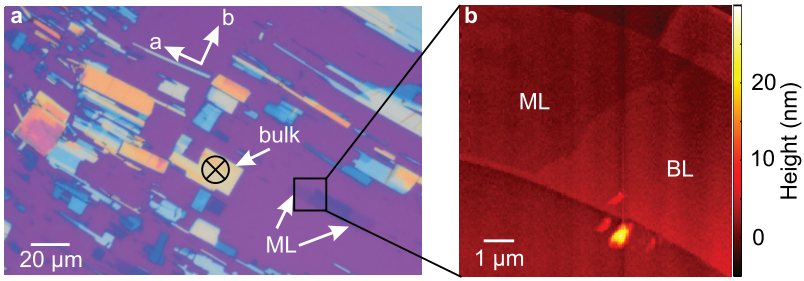

Figure 5.1 | Microscope images of an exfoliated CrSBr sample. a, Optical micrograph of a typical CrSBr sample including bulk flakes oriented along the crystallographic *a*-axis and monolayers (ML). **b**, In-situ atomic force microscopy image of the CrSBr monolayer from **a**, which is adjacent to a bilayer (BL).

5.1 Near-field response of bulk and monolayer CrSBr

Sample fabrication and characterisation. Our samples consist of CrSBr flakes, which are mechanically exfoliated on SiO_2 layers (thickness, 285 nm) fabricated on a p^{++}-doped silicon substrate (boron dopant concentration, $2 \times 10^{19}\,\mathrm{cm}^{-3} \leq n_B \leq 1 \times 10^{20}\,\mathrm{cm}^{-3}$). An optical microscope integrated in the near-field microscope allows us to optically examine the exfoliated CrSBr samples on mesoscopic scales (Figure 5.1a). The depicted area entails both bulk (yellow/blue) and monolayer (ML, faint blue) flakes, which, owing to the structural anisotropy of CrSBr, extend along the crystallographic *a*-axis. Further, we can microscopically image the CrSBr flakes *in situ* with the built-in atomic force microscope using the same metallic tip, to which the optical pump and terahertz probe pulses are coupled to for s-SNOM experiments (25PtIr200BH, Rocky Mountain Nanotechnology, LLC). Importantly, atomic force microscopy (AFM) allows us to identify atomically thin monolayer flakes, as shown in Figure 5.1b depicting an in-situ recorded AFM image of a CrSBr monolayer (left, ML) adjacent to a bilayer (BL, right).

Near-field investigation of CrSBr. The micron-sized lateral dimensions of the monolayer crystals are much smaller than the diffraction limit of terahertz pulses,

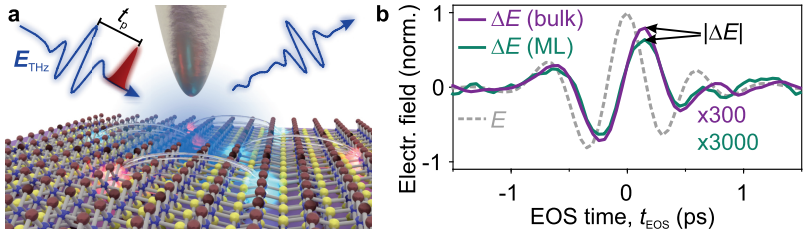

Figure 5.2 | Ultrafast polarisation nanoscopy of CrSBr. a, An optical pump pulse (red) generates electron–hole pairs in CrSBr (interconnected red and blue clouds). After a variable delay time, t_p, a terahertz probe pulse (blue, left) is coupled to the evanescent near field of a metallic tip. By phase-resolved detection of the scattered terahertz waveform (blue, right) information about the nanoscopic dielectric response of the sample is obtained. **b**, Electro-optically detected steady-state scattered terahertz waveform E (bulk, dotted grey line) and pump-induced change ΔE on bulk CrSBr (teal line) as well as a monolayer of CrSBr (pink line) for a pump photon energy of 1.39 eV as well as pump delay times $t_p = 0.5$ ps and $t_p = 0.4$ ps, respectively. The peak value of each pump-induced waveform, $|\Delta E|$, will be a key observable in the experiments presented in the next section.

impeding far-field terahertz spectroscopy. To overcome this mismatch, we focus the terahertz probe pulses (Section 3.3) to the apex of the atomic force microscope tip (Figure 5.2a, Section 3.1). The evanescent near field interacts with the CrSBr sample in a volume defined by the radius of curvature of the tip apex. Consequently, the nanoscale dielectric response of the sample is imprinted in the scattered terahertz transient, which we record by electro-optic sampling (Section 3.4). The tapping amplitude of the tip of 150 nm is kept constant throughout this work. Following our scheme to avoid far field contributions (Section 3.1), the near-field signal is retrieved by demodulation at the tip oscillation frequency, f_{tip}. Figure 5.2b depicts the steady-state waveform, E, which is scattered off a bulk sample (thickness, 400 nm).

Pump-induced response of the photoexcited sample. To investigate the ultrafast dynamics of electron–hole pairs in CrSBr, we photoexcite the sample using ultrashort (pulse durations, < 100 fs), widely tunable optical laser pulses from the noncollinear optical parametric amplifier (Figure 5.2a, red pulse, Chapter 4). The optically injected electron–hole pairs are deflected by the instantaneous terahertz

probe field, such that their polarisability manifests itself as pump-induced change of the scattered electric field, $\Delta E = E_{\mathrm{pumped}} - E_{\mathrm{unpumped}}$ (Section 3.2). Note, that ΔE is retrieved by demodulation at the first positive sideband originating from the pump modulation (frequency, f_{AOM}), that is, at $f_{\mathrm{tip}} + f_{\mathrm{AOM}}$. In this way, the far-field background of the recorded signal is additionally suppressed[56].

Figure 5.2b depicts exemplary electro-optically detected pump-induced traces of a bulk (thickness, 400 nm, purple) and a monolayer (teal) CrSBr flake as a function of the EOS time, t_{EOS}. The corresponding transients were recorded at pump delay times, $t_{\mathrm{p}} = 0.5\,\mathrm{ps}$ and $t_{\mathrm{p}} = 0.4\,\mathrm{ps}$, respectively, after photoexcitation with a photon energy, $h\nu_{\mathrm{p}} = 1.39\,\mathrm{eV}$. For both bulk and monolayer, ΔE roughly traces the steady-state response, E, with a phase shift of $\sim \pi/3$. We will investigate the corresponding spectra in more detail in Sections 5.3 and 5.4.

Importantly, considering the scales of the involved electric-field amplitudes highlights the extraordinary sensitivity of our experimental approach: The pump-induced signal originating from the CrSBr monolayer is smaller than the steady-state scattered terahertz waveform, E, by three orders of magnitude. Meanwhile, the electro-optic signal of E is already three orders of magnitude weaker than that of the incident far-field transient shown in Figure 3.8. Despite these minute signals, we achieve a signal-to-noise ratio of ∼14 for the atomically thin sample, showcasing the capability of our technique to resolve even most subtle changes in the nanoscale dielectric response of CrSBr.

5.2 Ultrafast dynamics and recombination of electron–hole pairs in CrSBr

The optoelectronic properties of CrSBr are dominated by tightly bound excitons. While photoluminescence measurements clearly identified exciton recombination at a photon energy of 1.37 eV in both bulk and monolayer CrSBr[19,27], the magnitudes of the respective single-particle bandgaps is still under debate[91]. Scanning tunnelling spectroscopy measurements estimate the bulk bandgap to be $(1.5 \pm 0.2)\,\mathrm{eV}$. However, in these experiments electronic coupling with the metallic substrate may influence the measured magnitude of the bandgap. The knowledge of the monolayer is limited to

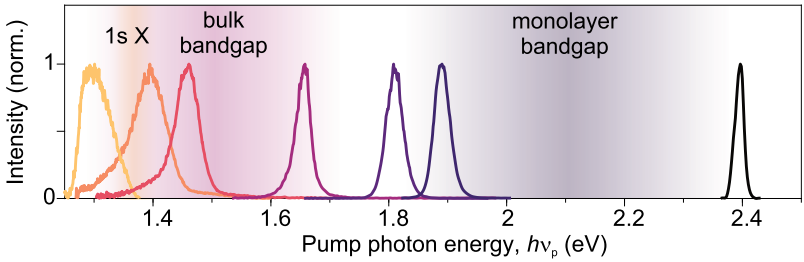

Figure 5.3 | Intensity spectra of the femtosecond pump pulses. The NOPA enables generation of femtosecond pulses centred at 1.30 eV up to 1.91 eV. The spectrum centred at 2.4 eV is the frequency-doubled laser fundamental. For context, the 1s exciton resonance (1s X) as well as the single-particle bandgap of bulk and monolayer CrSBr measured with scanning tunnelling spectroscopy[19,27] and predicted by GW calculations[19], are shown as purple and grey ribbons, respectively. The width of the ribbons represents the uncertainty of the magnitude of the bandgap in the current literature[19,27].

theoretical predictions altogether. Owing to these uncertainties, excitation pulses with variable photon energy, which can selectively inject electron–hole pairs, are mandatory for conclusive studies of ultrafast exciton dynamics. Moreover, polarisation excitation spectroscopy may provide valuable insights into the binding states of the probed electron–hole pairs by distinguishing highly polarisable unbound electron–hole pairs from excitons, whose polarisability is quenched by Coulomb attraction.

Ultrashort tunable pump pulses. Our home-built NOPA (Chapter 4) enables us to vary the photon energy of the pump pulses, $h\nu_p$, from 1.30 eV to 1.90 eV. Additionally, the second harmonic of the fundamental laser pulses ($h\nu_p = 2.41$ eV) can be used for photoexcitation. Figure 5.3 depicts the intensity spectra of the excitation pulses utilised in the ultrafast near-field experiments. The FWHM bandwidth of the spectra ranges from 18 meV ($h\nu_p = 2.41$ eV) to 70 meV ($h\nu_p = 1.39$ eV), while the pulse durations lie between 50 fs and 80 fs for the amplified signal pulses (see Figure 4.7b) and 100 fs for the second harmonic pulses. The 1s exciton resonance determined by photoluminescence measurements (yellow) as well as the reported bulk and monolayer single-particle bandgaps (purple and grey, respectively) are added for

context, where the width of the ribbons illustrates the respective uncertainty in the current literature[19,27]. We set the polarisation of the pump pulses along the b-axis of CrSBr, since the corresponding optical interband transitions are dipole-allowed in this direction, while they are strongly suppressed along the a-axis[97].

Extracting the dynamics and polarisability of the photoexcited electron–hole pairs. As there are no dipole-active phonon modes of CrSBr within the spectrum of our probe pulses[81,82] (Appendix B.2, Figure B.4), the near-field response of the sample is expected to be dominated by the photoexcited electron–hole pairs. Consequently, in a frequency range far from resonant quantum excitations, such as the Lyman-like 1s-2p transition, the peak value of the pump-induced change of the scattered terahertz transient, $|\Delta E|$ (see Figure 5.2b), is proportional to the density of photoexcited electron–hole pairs, n_{eh}, and their respective polarisability, α_{eh},

$$|\Delta E(t_{\mathrm{p}}, \nu_{\mathrm{p}})| \propto \alpha_{\mathrm{eh}}(t_{\mathrm{p}}, \nu_{\mathrm{p}}) \iiint_{V_{\mathrm{sample}}} \xi(\boldsymbol{r})\, n_{\mathrm{eh}}(\boldsymbol{r}, t_{\mathrm{p}}, \nu_{\mathrm{p}})\, \mathrm{d}^3 r. \tag{5.1}$$

Here, ν_{p} is the frequency of the pump light, V_{sample} the volume of the sample and $\xi(\boldsymbol{r})$ is a spatial weighting factor accounting for the probing sensitivity, which depends on experimental parameters such as the radius of curvature of the tip apex, r_{tip}, the tapping amplitude and the dielectric screening in the sample.

Importantly, the absorption and reflection of CrSBr and, thus, n_{eh}, substantially vary between resonant and off-resonant photoexcitation[19]. Thus, to quantitatively compare the polarisability of the photoexcited electron–hole pairs, α_{eh}, for different pump photon energies, one must evaluate the integral in Equation (5.1). Since the beam waist of the photoexcitation pulses ($\approx 7\,\mu\mathrm{m}$), is large compared to the radius of curvature of the tip apex ($r_{\mathrm{tip}} \approx 20\,\mathrm{nm}$), we can assume that in the effectively probed volume, n_{eh} is approximately constant along in-plane directions, x and y, and primarily varies along the out-of-plane direction, z, that is, $n_{\mathrm{eh}}(\boldsymbol{r}) \approx n_{\mathrm{eh}}(z)$. We further approximate the spatial weighting factor $\xi(\boldsymbol{r})$ by separating it into in- and

out-of-plane components, $\xi(\boldsymbol{r}) = \xi_{x,y}(x,y)\,\xi_z(z)$ (see Appendix B.1, Figure B.1):

$$|\Delta E(t_\mathrm{p},\nu_\mathrm{p})| \propto \alpha_\mathrm{eh}(t_\mathrm{p},\nu_\mathrm{p}) \int_0^{d_\mathrm{sample}} \xi_z(z)\, n_\mathrm{eh}(z,t_\mathrm{p},\nu_\mathrm{p})\,\mathrm{d}z \underbrace{\iint_{A_\mathrm{sample}} \xi_{x,y}(x,y)\,\mathrm{d}x\,\mathrm{d}y}_{=\text{const.}}. \quad (5.2)$$

Here, d_sample and A_sample denote the thickness and area of the sample. As $\xi_{x,y}(x,y)$ only depends on unchanged experimental parameters such as r_tip and the tapping amplitude, the second integral in Equation (5.2) can be regarded as a geometric constant. In this way, the dependence of Equation (5.2) on the photoexcitation is reduced to a one-dimensional problem,

$$\begin{aligned} |\Delta E(t_\mathrm{p},\nu_\mathrm{p})| &\propto \alpha_\mathrm{eh}(t_\mathrm{p},\nu_\mathrm{p}) \int_0^{d_\mathrm{sample}} \xi_z(z)\, n_\mathrm{eh}(z,t_\mathrm{p},\nu_\mathrm{p})\,\mathrm{d}z \\ &\equiv \alpha_\mathrm{eh}(t_\mathrm{p},\nu_\mathrm{p})\,\zeta(t_\mathrm{p},\nu_\mathrm{p}). \end{aligned} \quad (5.3)$$

When we divide $|\Delta E(t_\mathrm{p},\nu_\mathrm{p})|$ by the integral in Equation (5.3), ζ, evaluated directly after photoexcitation ($t_\mathrm{p} = t_\mathrm{peak}$), we obtain a quantity, which is independent of the reflection and absorption spectra of the sample:

$$\Delta E_\mathrm{peak}(t_\mathrm{p},\nu_\mathrm{p}) \equiv \frac{|\Delta E(t_\mathrm{p},\nu_\mathrm{p})|}{\zeta(t_\mathrm{p}=t_\mathrm{peak},\nu_\mathrm{p})} = \alpha_\mathrm{eh}(t_\mathrm{p},\nu_\mathrm{p}) \frac{\zeta(t_\mathrm{p},\nu_\mathrm{p})}{\zeta(t_\mathrm{p}=t_\mathrm{peak},\nu_\mathrm{p})}. \quad (5.4)$$

Consequently, ΔE_peak provides a gauged measure of the dynamics and polarisability of the photoexcited electron–hole pairs.

Estimating the electron–hole pair density. We now calculate the integral $\zeta(t_\mathrm{p} = t_\mathrm{peak},\nu_\mathrm{p})$ for bulk and monolayer CrSBr samples. According to the Lambert-Beer law, the density of photoexcited electron–hole pairs directly after photoexcitation ($t_\mathrm{p} = t_\mathrm{p,peak}$) depends on the respective pump fluence $\Phi_\mathrm{p}(\nu_\mathrm{p})$ as

$$n_\mathrm{eh}(z,t_\mathrm{p}=t_\mathrm{p,peak},\nu_\mathrm{p}) = (1-r_\mathrm{s}(\nu_\mathrm{p})^2)\frac{\Phi_\mathrm{p}(\nu_\mathrm{p})}{h\nu_\mathrm{p}}\,\alpha(\nu_\mathrm{p})\,\mathrm{e}^{-\alpha(\nu_\mathrm{p})z}. \quad (5.5)$$

Here, r_s denotes the Fresnel coefficient for reflection of the s-polarised pump light and α is the absorption coefficient, which is calculated directly from the complex-valued

dielectric function as $\alpha^{-1} = \sqrt{\varepsilon}c(2\pi\nu_\mathrm{p}\varepsilon_\mathrm{imag})^{-1}$. Plugging Equation (5.5) into ζ yields

$$\zeta(t_\mathrm{p} = t_\mathrm{p,peak}, \nu_\mathrm{p}) = \frac{\Phi_\mathrm{p}(\nu_\mathrm{p})}{h\nu_\mathrm{p}}(1 - r_\mathrm{s}(\nu_\mathrm{p})^2) \int_0^{d_\mathrm{sample}} \xi_z(z)\alpha(\nu_\mathrm{p})\, \mathrm{e}^{-\alpha(\nu_\mathrm{p})z}\, \mathrm{d}z. \tag{5.6}$$

Note, that for a constant weighting factor, $\xi_z(z) = 1$, ζ is a product of the pump photon fluence and the absorption spectrum of the sample.

In the atomically thin CrSBr monolayer samples, the photoexcited electron–hole pairs are located directly beneath the tip of the near-field microscope. Therefore, we can assume $\xi_z(z) = 1 = \mathrm{const}$. Importantly, to determine n_eh, thin-film interference of the pump light with reflections from the SiO_2 film below the sample and the p^{++}-doped silicon substrate must be taken into account. The multiple reflections in our system comprised of a stack of Air/CrSBr/SiO_2(285 nm)/Si(p^{++}) are implemented by the transfer matrix method following References 139 and 140. We use the dielectric function of CrSBr, ε, calculated with the Bethe-Salpeter equation[19], while the dielectric function of SiO_2 is assumed to be constant at 2.11. For the substrate, the refractive index reported in Reference 141 was used. In the near-field microscope, the angle of incidence of the pump pulses, which are polarised perpendicular with respect to the plane of incidence, is 30° with respect to the sample surface. The calculated absorption spectrum of the monolayer, modelled with a thickness of 1 nm (Reference 32), is shown in Figure 5.4a.

In the bulk, one has to consider the finite probing depth by including the weighting factor $\xi_z(z)$ in Equation (5.6). A good approximation for $\xi_z(z)$ is an exponential decay along z with a decay length given by the ratio of the tapping amplitude and the dielectric function at the probe frequency[108] (Figure 5.4b). In our experiment, the tapping amplitude of 150 nm and the terahertz dielectric constant of bulk CrSBr of 10 (Reference 34) yield a weighting factor, $\xi_z(z) = \mathrm{e}^{-z/15\,\mathrm{nm}}$. Figure 5.4c depicts the calculated absorption spectrum of bulk CrSBr ($d_\mathrm{sample} = 400\,\mathrm{nm}$) alongside the ratio

$$\eta(\nu_\mathrm{p}) = \frac{\int_0^{d_\mathrm{sample}} \xi_z(z)\, \mathrm{e}^{-\alpha(\nu_\mathrm{p})z}\, \mathrm{d}z}{\int_0^{d_\mathrm{sample}} \mathrm{e}^{-\alpha(\nu_\mathrm{p})z}\, \mathrm{d}z.} = \frac{\int_0^{d_\mathrm{sample}} \mathrm{e}^{-z/15\,\mathrm{nm}}\, \mathrm{e}^{-\alpha(\nu_\mathrm{p})z}\, \mathrm{d}z}{\int_0^{d_\mathrm{sample}} \mathrm{e}^{-\alpha(\nu_\mathrm{p})z}\, \mathrm{d}z.}, \tag{5.7}$$

which quantifies the influence of the finite probing depth on the pump-induced signal.

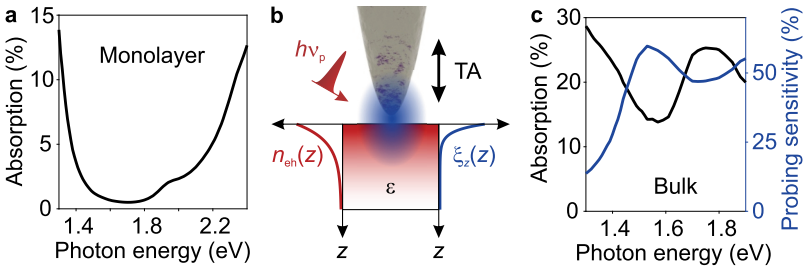

Figure 5.4 | Estimated absorption spectra in CrSBr. a, Absorption spectrum of monolayer CrSBr, calculated with the transfer matrix method. **b**, In bulk CrSBr, the electron–hole density, n_{eh} (red line), exponentially decays along the growth direction, z. Simultaneously, the weighting factor $\xi_z(z)$ representing the probing sensitivity exhibits an exponential decay (blue line) determined by the dielectric function, ε, and the tapping amplitude (TA). **c**, Absorption spectrum of bulk CrSBr (thickness, 400 nm), calculated with the transfer matrix method (black line) and the probing sensitivity, η (blue line).

Ultrafast electron–hole pair dynamics in bulk CrSBr. We now unveil the ultrafast dynamics of photoexcited electron–hole pairs in bulk CrSBr by means of terahertz polarisation nanoscopy. To this end, we trace the maximum pump-induced change of the scattered terahertz transient, ΔE_{peak} ($t_{\mathrm{EOS}} = 0.15\,\mathrm{ps}$), as a function of the pump delay time, t_{p}. Figure 5.5a depicts the pump-probe dynamics of the terahertz near-field response of a bulk flake with a thickness of 400 nm. The sample is photoexcited with various photon energies, $1.30\,\mathrm{eV} \leq h\nu_{\mathrm{p}} \leq 1.81\,\mathrm{eV}$, spanning both the 1s exciton resonance at 1.37 eV and the reported single-particle bandgap of $(1.5 \pm 0.2)\,\mathrm{eV}$, at a constant pump fluence, $\Phi_{\mathrm{p}} = 5\,\mathrm{mJ\,cm^{-2}}$.

Regardless of the photon energy, the pump-induced signal abruptly increases upon photoexcitation and reaches its maximum at $t_{\mathrm{p}} = 0.5\,\mathrm{ps}$, before it decays with a biexponential behaviour. Fitting the pump-probe dynamics (dashed lines), we extract a slow decay time, $\tau_{\mathrm{slow}} = (15 \pm 3)\,\mathrm{ps}$, common to all datasets. However, the initial decay strongly depends on the excitation photon energy: For energies, $h\nu_{\mathrm{p}} = 1.39\,\mathrm{eV}$, $1.46\,\mathrm{eV}$ and $1.65\,\mathrm{eV}$, we observe an initial decay time, $\tau_{\mathrm{fast}} = (1.6 \pm 0.3)\,\mathrm{ps}$. In contrast, for $h\nu_{\mathrm{p}} = 1.81\,\mathrm{eV}$, this decay is much shorter, taking place within $\tau_{\mathrm{fast}} = (1.0 \pm 0.1)\,\mathrm{ps}$. Furthermore, the amplitude of ΔE_{peak} is

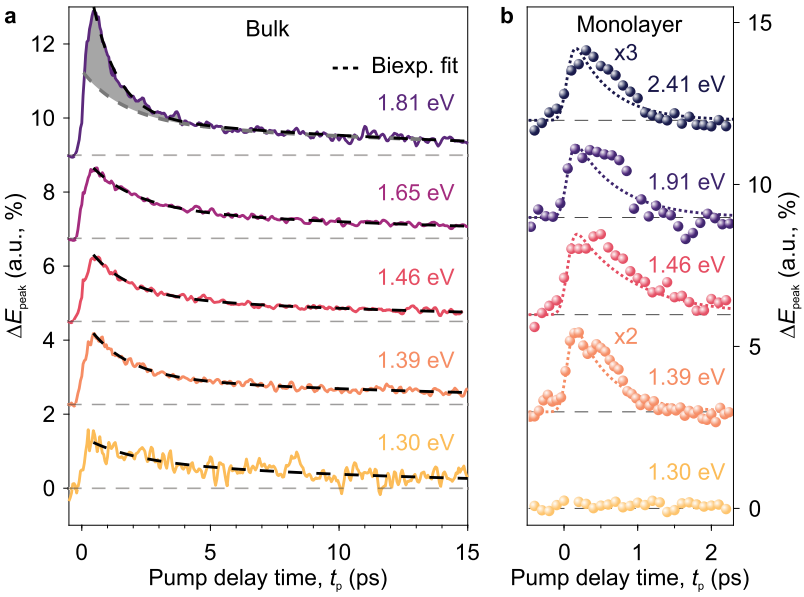

Figure 5.5 | Ultrafast electron–hole pair dynamics in bulk and monolayer CrSBr. **a**, Maximal pump-induced change of the near-field response along t_{EOS}, ΔE_{peak} as a function of the pump delay time, t_{p}, for various excitation photon energies (solid lines). The decay of ΔE_{peak} is fitted with a biexponential function (dashed lines). The grey shaded area in the topmost dataset indicates the excess of the pump-induced signal compared to lower photon energies. The data is offset for clarity. **b**, Analogous to panel **a** for the monolayer limit. The experimental data is shown as spheres, while the dashed lines are calculated with a rate equation model described in the main text.

significantly larger than for smaller photon energies, illustrated by the grey area in Figure 5.5a.

The dependence of the decay on the photon energy suggests that we observe the ultrafast dynamics of different species of electron–hole pairs. Photoexciting below the single-particle bandgap, we expect to prepare initially hot excitons, which relax into the 1s ground state within approximately 1.6 ps. Interestingly, short-range spin correlations, that is, paramagnons, have been shown to provide an important scattering channel in paramagnetic crystals far above their respective magnetic ordering temperature[74,87,88]. Moreover, as paramagnons provide a significant contribution to the heat capacity of paramagnets[87], we expect that the thermalisation of the photoexcited excitons is caused by scattering with paramagnons or phonons. In contrast, the fast decay of the polarisation signal at $h\nu_\mathrm{p} = 1.81\,\mathrm{eV}$ indicates the formation of 1s excitons; when excitons from energetically more distant bands or unbound electron–hole pairs bind into 1s excitons, their polarisability is quenched by Coulomb attraction. We will investigate the different excitation scenarios in more detail by means of near-field spectroscopy in Section 5.3. We attribute the slow decay common to all photon energies to the recombination of 1s excitons with a lifetime of $\sim 15\,\mathrm{ps}$.

Femtosecond exciton recombination in a monolayer of CrSBr. Next, we use our nanoscopic approach to unveil the ultrafast electron–hole pair dynamics in CrSBr monolayers, whose lateral dimensions are much smaller ($\sim 10\,\mu\mathrm{m} \times 10\,\mu\mathrm{m}$) than the diffraction limit of our terahertz probe pulses ($\sim 300\,\mu\mathrm{m} \times 300\,\mu\mathrm{m}$). We estimate that, depending on the excitation photon energy, only few tens to hundreds of electron–hole pairs are probed by the evanescent near field below the tip apex. Owing to the outstanding sensitivity and stability of the experimental setup, we can still reveal their femtosecond dynamics after photoexcitation. Analogous to the pump-probe study of bulk CrSBr, we trace ΔE_peak as a function of t_p for pump photon energies of 1.30 eV (below the 1s exciton resonance) 1.39 eV, 1.46 eV, 1.91 eV (above the 1s exciton resonance) and 2.41 eV (above the calculated bandgap), as shown in Figure 5.5b. The applied pump fluences were restricted to $\Phi_\mathrm{p} \leq 2.5\,\mathrm{mJ\,cm^{-2}}$, safely below the damage threshold of the monolayer. No pump-induced change of the scattered terahertz waveform is detected at $h\nu_\mathrm{p} = 1.30\,\mathrm{eV}$, below the exciton

resonance. In stark contrast, when the pump photon energy is sufficient to generate excitons, we observe an abrupt rise of ΔE_{peak}, followed by an ultrafast, sub-picosecond decay. Therefore, the observed dynamics can be attributed to the ultrafast excitation and recombination of excitons in a monolayer of CrSBr.

Since ΔE_{peak} evolves on timescales, which are comparable to the duration of our pump and gate pulses ($\sim 100\,\mathrm{fs}$), for a quantitative investigation, we simulate the dynamics with a rate equation model incorporating the finite laser pulse durations. First, we assume, that the polarisability of the excitons does not change as a function of time. Consequently, the dynamics of ΔE_{peak} are given by the electron–hole pair density, n_{eh} (see Equations (5.3) and (5.4)). We calculate the temporal evolution of n_{eh} with a straightforward rate equation,

$$\frac{\mathrm{d}n_{\mathrm{eh}}(t_{\mathrm{p}})}{\mathrm{d}t_{\mathrm{p}}} = S_{\mathrm{pump}}(t_{\mathrm{p}}) - \frac{n_{\mathrm{eh}}(t_{\mathrm{p}})}{\tau}, \tag{5.8}$$

where S_{pump} is a source term following the temporal intensity envelope of the pump pulse, modelled as a Gaussian with a FWHM of 100 fs. The photoexcited exciton population recombines with the lifetime, τ, representing the only fit parameter in the model. In order to account for the finite detection bandwidth, the modelled dynamics are convoluted with the Gaussian intensity envelope of the electro-optic gate pulses featuring a duration of 140 fs. In this way, both the onset and the decay of ΔE_{peak} can be reliably reproduced (dashed lines), allowing us to directly gauge the lifetime of excitons in atomically thin CrSBr, for the first time. We find, that the best agreement with the experimental data ($h\nu_{\mathrm{p}} = 1.39\,\mathrm{eV}$) is achieved with an exciton lifetime of $\tau = 0.5\,\mathrm{ps}$, which is 30 times faster than the decay we revealed in the bulk.

Owing to the large oscillator strength of quasi-one-dimensional excitons, an ultrashort radiative exciton lifetime in CrSBr is expected. We obtain a first estimate of the intrinsic radiative lifetime of excitons in monolayer CrSBr, τ^0_{rad}, with a simplistic two-band model in two dimensions, following Reference 142:

$$\tau^0_{\mathrm{rad}} = \frac{4\pi\varepsilon_0\varepsilon\hbar}{2k_0}\left(\frac{E_{\mathrm{X}}}{e\hbar v}\right)^2\left(a^{\mathrm{2D}}_{\mathrm{B}}\right)^2. \tag{5.9}$$

Here, $k_0 = E_{\mathrm{X}}\sqrt{\varepsilon}/(\hbar c)$ is the wavevector of the emitted light, E_{X} the exciton transi-

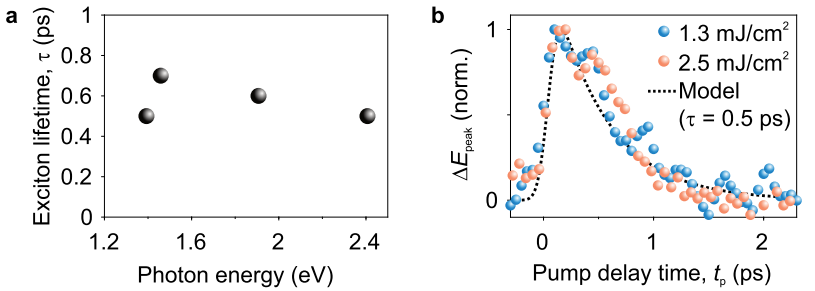

Figure 5.6 | Dependence of the exciton lifetime in monolayer CrSBr on the pump photon energy and fluence. a, The exciton lifetime, τ, obtained by fitting the decay dynamics with a rate equation model, only slightly varies as a function of the excitation photon energy. **b**, The dynamics of ΔE_{peak} ($h\nu_{\mathrm{p}} = 1.39\,\mathrm{eV}$) are equal for pump fluences of $\Phi_{\mathrm{p}} = 1.3\,\mathrm{mJ\,cm^{-2}}$ (blue spheres) and $\Phi_{\mathrm{p}} = 2.5\,\mathrm{mJ\,cm^{-2}}$ (orange spheres) and are accurately reproduced with a lifetime of $\tau = 0.5\,\mathrm{ps}$ (black dashed line).

tion energy, c the speed of light, $v = \sqrt{E_{\mathrm{g}}/2m^*}$ the so-called Kane velocity and $a_{\mathrm{B}}^{\mathrm{2D}}$ the two-dimensional exciton Bohr radius. The anisotropy of the exciton wavefunction is caused by the distinct effective masses along the a- and b- crystallographic axes, which result in the Bohr radii, r_a and r_b, respectively. In a first approximation, we estimate the effective Bohr radius by describing the exciton as an ellipse with principal radii r_a and r_b, yielding $a_{\mathrm{B}}^{\mathrm{2D}} = \sqrt{r_a r_b}$. Analogously, following Reference 143, the average effective electron mass, $m^* = \sqrt{m_a^* m_b^*}$ is obtained by equating the area of an ellipse in momentum space with principal radii m_a^* and m_b^* with the one of a circle with radius m^*. For the effective masses given in Reference 19, $\varepsilon = 10$ (Reference 34), $E_{\mathrm{X}} = 1.37\,\mathrm{eV}$ and $E_{\mathrm{g}} = 2.10\,\mathrm{eV}$ (Reference 19), a radiative lifetime, $\tau_{\mathrm{rad}}^0 \approx 0.8\,\mathrm{ps}$, is obtained.

This estimate is close to the measured exciton lifetime of 0.5 ps, however, the decay of ΔE_{peak} is barely affected by the pump photon energy (Figure 5.6a), suggesting a significant contribution also from nonradiative recombination. As the dynamics are further independent of the pump fluence (Figure 5.6b), Auger processes can be ruled out, leaving radiative recombination and recombination at defects and surface impurities as the most important decay channels.

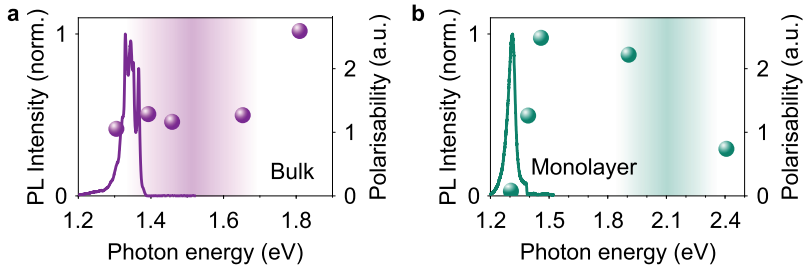

Figure 5.7 | Excitation polarisation spectroscopy of bulk and monolayer CrSBr. **a**, Polarisability of the photoexcited electron–hole pairs in bulk CrSBr as a function of the pump photon energy (purple spheres). For context, the low-temperature photoluminescence spectrum (solid purple line) and bandgap measured with scanning tunnelling spectroscopy (purple ribbon) are shown. **b**, Polarisability of the photoexcited electron–hole pairs in a monolayer of CrSBr as a function of the pump photon energy (teal spheres). The low-temperature photoluminescence spectrum (solid teal line) and bandgap predicted by GW calculations (teal ribbon) are shown for context.

Polarization excitation spectroscopy. Polarisation excitation spectroscopy can offer valuable insights into how the polarisability of the initially photoexcited electron–hole pairs is influenced by their binding state. To this end, the maximum of ΔE_{peak} at $t_{\mathrm{p}} = 0.5\,\mathrm{ps}$ (bulk) and $t_{\mathrm{p}} = 0.4\,\mathrm{ps}$ (monolayer) is traced as a function of the pump photon energy (Figure 5.7). The normalisation of ΔE_{peak} (Equation (5.4)) allows us to gauge the polarisability of the initially photoexcited electron–hole pairs. The data are overlaid with the measured low-temperature photoluminescence spectra (solid lines) as well as the single-particle bandgaps obtained by scanning tunnelling spectroscopy[27] (bulk) and GW calculations[19] (monolayer), respectively.

The polarisability of the photoexcited bulk sample (Figure 5.7a, purple spheres) is constant for photon energies $1.30\,\mathrm{eV} \leq h\nu_{\mathrm{p}} \leq 1.65\,\mathrm{eV}$. At $h\nu_{\mathrm{p}} = 1.81\,\mathrm{eV}$, the polarisability substantially increases, suggesting a dominant contribution of electron–hole pairs featuring weak or no Coulomb binding. In the monolayer, the polarisability increases upon photoexcitation above the 1s exciton ground state at 1.37 eV. After a plateau at $h\nu_{\mathrm{p}} = 1.46\,\mathrm{eV}$ and $h\nu_{\mathrm{p}} = 1.91\,\mathrm{eV}$ the polarisability decreases by a factor of three, when the pump photon energy is tuned to 2.41 eV. This reduction strongly

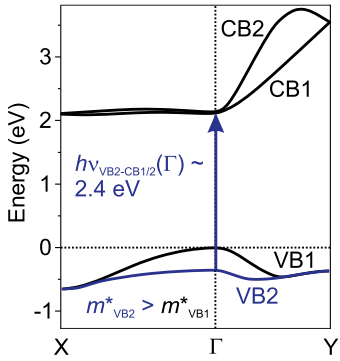

Figure 5.8 | Excitons from a lower valence band. Simplified calculated band structure of monolayer CrSBr, adapted from Reference 19. The lowest two conduction bands (CB1, CB2) and highest two valence bands (VB1, VB2) are shown. Electron–hole pairs can be photoexcited from the lower valence band, VB2 (blue) into one of the conduction bands, CB1 or CB2, with a photon energy of $\sim 2.4\,\mathrm{eV}$. Note, that along both the Γ-X and Γ-Y directions, VB2 exhibits a much smaller curvature than VB1 (black), corresponding to a higher effective mass, $m^*_{\mathrm{VB2}} > m^*_{\mathrm{VB1}}$.

contrasts with the bulk polarisability spectrum and suggests that we observe less polarisable, more strongly bound excitons originating from a lower valence band with higher effective masses, which have been theoretically predicted[19] (Figure 5.8).

5.3 Near-field spectroscopy of photoexcited electron–hole pairs in bulk CrSBr

As demonstrated in the previous section, analysing ΔE_{peak} provides valuable insights into the polarisability and ultrafast dynamics of photoexcited electron-hole pairs. However, thoroughly studying their binding states requires complete near-field spectroscopy making use of the large parameter space of our experimental scheme.

Terahertz time-domain nanospectroscopy. To this end, the terahertz field waveform scattered off a bulk CrSBr sample (thickness, 400 nm) is electro-optically sampled for various pump photon energies and pump delay times. We focus on photoexcitation close to the 1s exciton resonance ($h\nu_{\mathrm{p}} = 1.39\,\mathrm{eV}$) and above the single-particle bandgap ($h\nu_{\mathrm{p}} = 1.81\,\mathrm{eV}$). Based on the dynamics presented in Section 5.2 (Figure 5.5a), the initial, ultrafast decay of ΔE_{peak} for $h\nu_{\mathrm{p}} = 1.81\,\mathrm{eV}$ was associated with the dynamics of electron–hole pairs binding into 1s excitons. To test this hypothesis, we compare the pump-induced terahertz near-field response at $t_{\mathrm{p}} = 0.5\,\mathrm{ps}$ and $t_{\mathrm{p}} = 2.5\,\mathrm{ps}$, which would originate from excitons from energetically more distant

bands or continuum states and 1s excitons, respectively. The pump-induced change at $h\nu_\mathrm{p} = 1.39\,\mathrm{eV}$ and $t_\mathrm{p} = 0.5\,\mathrm{ps}$ serves as reference for the terahertz response of 1s excitons.

Figure 5.9a depicts the steady-state scattered terahertz waveform, E (grey), alongside the pump-induced change, ΔE ($\Phi_\mathrm{p} = 4\,\mathrm{mJ\,cm^{-2}}$), for $h\nu_\mathrm{p} = 1.39\,\mathrm{eV}$ and $t_\mathrm{p} = 0.5\,\mathrm{ps}$ (orange), $h\nu_\mathrm{p} = 1.81\,\mathrm{eV}$ and $t_\mathrm{p} = 0.5\,\mathrm{ps}$ (purple) as well as $h\nu_\mathrm{p} = 1.81\,\mathrm{eV}$ and $t_\mathrm{p} = 2.5\,\mathrm{ps}$ (blue). The first maximum and second maximum of all ΔE waveforms are located close to zero crossings of the steady-state response. However, at later electro-optic delay times, differences between the transients appear, as highlighted in Figure 5.9b. Both the minimum at $t_\mathrm{EOS} = 0.45\,\mathrm{ps}$ and the maximum at $t_\mathrm{EOS} = 0.70\,\mathrm{ps}$ are much more pronounced for $h\nu_\mathrm{p} = 1.81\,\mathrm{eV}$ and $t_\mathrm{p} = 0.5\,\mathrm{ps}$ than for the other waveforms sharing comparable amplitudes.

This difference is characteristic of distinct pump-induced changes of the dielectric function. To quantitatively relate the microscopic spectral response with the time-domain traces observed in Figure 5.9a, we Fourier transform the waveforms ΔE and E and analyse the relative spectral amplitude, $\Delta\tilde{E}/\tilde{E}$ (Figure 5.9d-f, top left panels) and phase, $\Delta\phi - \phi$ (Figure 5.9d-f, bottom left panels). Note, that the effective probe frequency range in our experiment, given by the Fourier components of E exceeding 10% of the maximum of the spectral amplitude, ranges from 0.6 THz to 2.2 THz. The relative spectral amplitude for $h\nu_\mathrm{p} = 1.81\,\mathrm{eV}$ and $t_\mathrm{p} = 0.5\,\mathrm{ps}$ exhibits a minimum around 1.6 THz and rises towards the spectral edges, while $\Delta\phi - \phi$ monotonically increases with frequency (Figure 5.9d). This pump-induced response contrasts with the other two cases (Figure 5.9e,f), where $\Delta\tilde{E}/\tilde{E}$ monotonically decreases with frequency and the spectral phase remains constant at $\sim 0.3\pi$.

Modelling the spectral near-field response. We now examine the relation of the dielectric response of the sample to the measured spectral signatures by modelling near-field scattering off the photoexcited bulk CrSBr sample with the finite-dipole model (Appendix B.1). The near-field response of the photoexcited sample at $h\nu_\mathrm{p} = 1.81\,\mathrm{eV}$ and $t_\mathrm{p} = 0.5\,\mathrm{ps}$ can be reproduced best with a Drude dielectric function (Figure 5.9d, right panel). The good agreement of the modelled spectrum with the experimental data indicates a dominant contribution of unbound electron–hole pairs after photoexcitation.

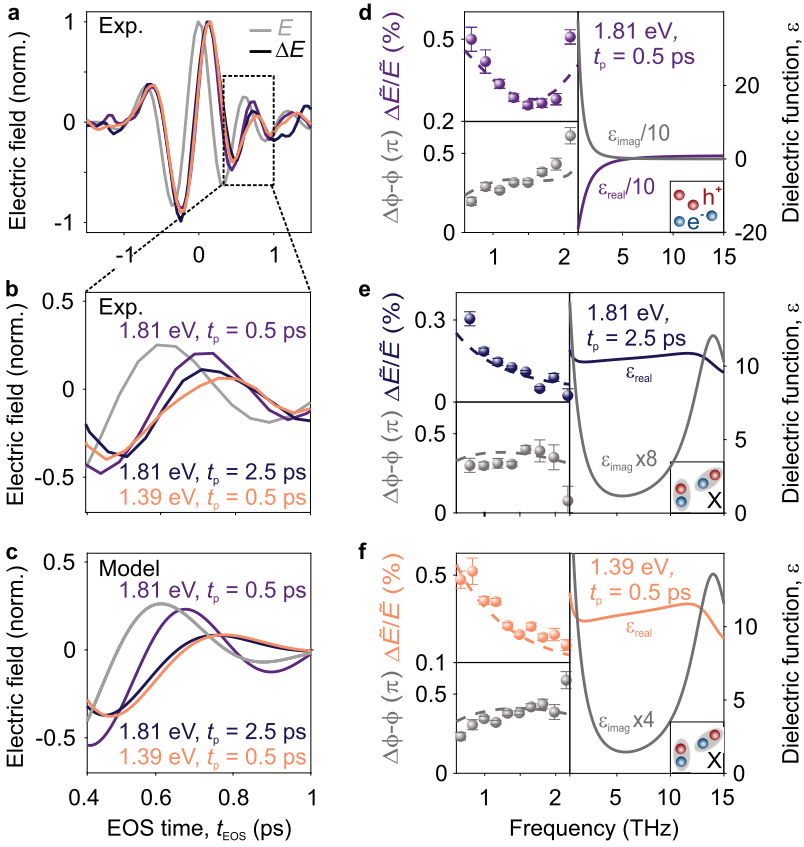

Figure 5.9 | Identifying binding states of electron–hole pairs in bulk CrSBr by terahertz near-field spectroscopy. **a**, Experimental pump-induced changes of the scattered terahertz waveform, ΔE, on bulk CrSBr as a function of the EOS time, t_{EOS} for different pump photon energies and pump delay times, t_{p}. The steady-state near-field response, E, is shown in grey. **b**, Zoom-in to the EOS time window between 0.4 ps and 1 ps. **c**, Time-domain near-field response modelled with the finite-dipole model. **d-f**, Relative spectral amplitude, $\Delta\tilde{E}/\tilde{E}$, (top left panels) and phase, $\Delta\phi - \phi$, (bottom left panels) of the near-field response. The modelled data (dashed lines) calculated with Drude (**d**) and Lorentzian (**e**, **f**) dielectric functions (right panels) excellently reproduce the experimental data (spheres).

In contrast, a Drude response fails to explain the terahertz spectra for $h\nu_p = 1.39\,\mathrm{eV}$ and $t_p = 0.5\,\mathrm{ps}$ as well as $h\nu_p = 1.81\,\mathrm{eV}$ and $t_p = 2.5\,\mathrm{ps}$. Thus, we model the corresponding dielectric functions with two Lorentzian lines. The first oscillator represents the strong, off-resonantly probed excitonic 1s-2p transition, which has been identified in terahertz time-domain spectroscopy experiments to lie at 14 THz (Reference 144), while the second, low-energy resonator at 1 THz comprises all intra-excitonic transitions from states with large principal quantum numbers (Figure 5.9e,f, right panels). Employing this exclusively excitonic dielectric response, we can model both near-field spectra in excellent agreement with the experiment. Moreover, the contrast between the Drude and the excitonic terahertz response is evident in the modelled time-domain data (Figure 5.9c), which is consistent with the experimental relative amplitudes of the peaks around $t_{EOS} = 0.45\,\mathrm{ps}$ and $t_{EOS} = 0.70\,\mathrm{ps}$. Consequently, our findings provide strong evidence, that at a pump photon energy of 1.81 eV, unbound electron–hole pairs dominate the nanoscale dielectric response at $t_p = 0.5\,\mathrm{ps}$ before they bind into excitons on the timescale of 1 ps.

5.4 Extracting the nonequilibrium dielectric function of a CrSBr monolayer

In the monolayer sample, effects of finite probing depths and interlayer tunnelling are negligible, enabling us to reliably extract the complex-valued nonequilibrium dielectric function in a model-free manner. To this end, we first sample the steady-state scattered terahertz waveform, E, and the pump-induced change, ΔE, on a monolayer flake $t_p = 0.4\,\mathrm{ps}$ after photoexcitation of the exciton ground state ($h\nu_p = 1.39\,\mathrm{eV}$) with a fluence $\Phi_p = 1.6\,\mathrm{mJ\,cm^{-2}}$ (Figure 5.10a). With respect to the waveform E, ΔE is delayed and the first minimum is enhanced, while the second minimum is suppressed. The relative spectral amplitude, depicted as red spheres in Figure 5.10b decreases monotonically with frequency. Simultaneously, the relative phase (black spheres) is almost constant at 0.3π.

By inverting the finite-dipole model[108], we can directly retrieve the complex-valued dielectric function of the photoexcited monolayer, ε, from the spectral near-field response. The only required assumption is the equilibrium dielectric function, ε_{eq},

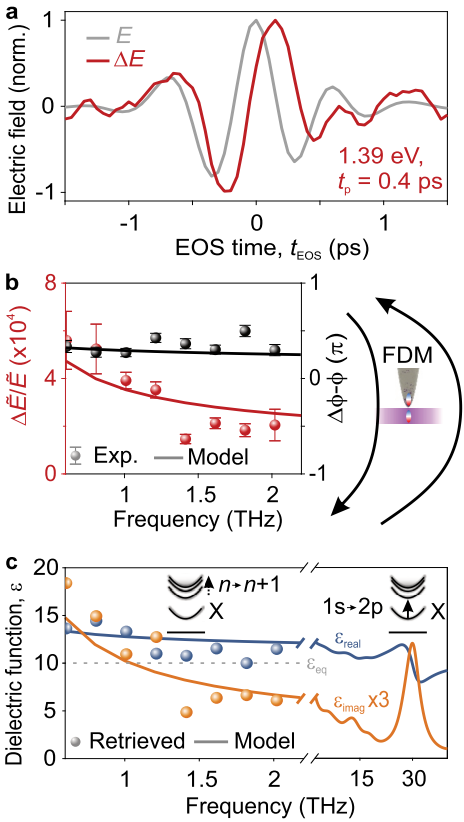

Figure 5.10 | Direct retrieval of the complex-valued nonequilibrium dielectric function of a photoexcited CrSBr monolayer. a, Experimental pump-induced change of the scattered terahertz waveform, ΔE, (red) along t_{EOS}. The steady-state near-field response, E, is shown in grey. **b**, Relative spectral amplitude, $\Delta\tilde{E}/\tilde{E}$, (red spheres) and phase, $\Delta\phi - \phi$, (black spheres) of the near-field response. **c**, Dielectric function obtained for an anisotropic Rytova-Keldysh confinement potential (solid lines) used to calculate the near-field response shown in **b** (solid lines). The dielectric function is marked by transitions between highly excited excitons (X, $n \to n+1$) and the 1s-2p transition at 27 THz. By numerically inverting the finite-dipole model (FDM), we retrieve the complex-valued dielectric function, ε, of the photoexcited monolayer (spheres). The assumed equilibrium dielectric function, $\varepsilon_{eq} = 10$, is shown as grey dashed line.

which we found to be constant throughout our probe spectrum (see Appendix B.2). The retrieved dielectric function for $\varepsilon_{\mathrm{eq}} = 10$ (Reference 34) is shown in Figure 5.10c. Below 1.2 THz, the real part of ε, $\varepsilon_{\mathrm{real}}$ (blue spheres), is increased by approximately 30% with respect to the steady state (grey line), while for higher frequencies, is only slightly enhanced. Meanwhile, the imaginary part, $\varepsilon_{\mathrm{imag}}$ (orange spheres), decreases with increasing frequency. The increase of both $\varepsilon_{\mathrm{real}}$ and $\varepsilon_{\mathrm{imag}}$ towards smaller frequencies is comparable to the excitonic dielectric response in the bulk (Figure 5.9f) and, thus, reminiscent of transitions between highly excited excitons.

Modelling the nonequilibrium dielectric function of a CrSBr monolayer. To test this hypothesis, we model the nonequilibrium dielectric function of the CrSBr monolayer by calculating the exciton eigenstates and eigenenergies for a modified Rytova-Keldysh potential[145,146],

$$V(r) = -\frac{1}{4\pi\varepsilon_0}\frac{e^2}{r_0}\frac{\pi}{2}\left[H_0\left(\frac{\kappa r}{r_0}\right) - Y_0\left(\frac{\kappa r}{r_0}\right)\right]. \tag{5.10}$$

Here, H_0 and Y_0 denote the zero-order Struve and Neumann special functions and $\kappa = (\varepsilon_{\mathrm{air}} + \varepsilon_{\mathrm{SiO_2}})/2$ represents the screening of the hemispheres of air and SiO_2 the monolayer is embedded in. Finally, $r_0 = 2\pi \times 1\,\mathrm{nm}$ is a measure of the dielectric screening length in the CrSBr monolayer, taken from Reference 26. To account for the strong anisotropy of the reduced effective mass, μ, we perform a transformation of coordinates following References 145 and 147:

$$r \to r\sqrt{1 + \beta\cos\theta}, \tag{5.11}$$

where $\beta = (\mu_a - \mu_b)/(\mu_a + \mu_b)$ and θ is the polar angle. The respective reduced effective masses along the a- and b-axis, μ_a and μ_b are taken from Reference 19. We use the transition matrix elements as measure of the oscillator strength of Lorentz lines, which are centred at the respective transition energies. Assuming a thermal distribution ($k_{\mathrm{B}}T = 40\,\mathrm{meV}$) of the photoexcited exciton states, the pump-induced change of ε is obtained (see Appendix B.2 for details).

The real (blue) and imaginary part (orange) of the modelled dielectric function are depicted as solid curves in Figure 5.10c. The 1s-2p transition is imprinted in the

dielectric response as a peak in $\varepsilon_{\mathrm{imag}}$ at approximately 27 THz. At lower frequencies, the transitions between the more narrowly spaced exciton states with large principal quantum number manifest as steep increase of both real and imaginary part for decreasing frequency, which is in good agreement with the retrieved dielectric function. Moreover, calculating the spectral near-field response of the photoexcited monolayer sample using the modelled dielectric function closely matches the experimental data. Therefore, our findings provide strong evidence, that the room-temperature terahertz dielectric response of monolayer CrSBr is dominated by transitions between highly excited, quasi-one-dimensional excitons.

Conclusion: Femtosecond relaxation and recombination of excitons in the quantum material CrSBr. In summary, we explored the ultrafast dynamics of electron–hole pairs in CrSBr by means of terahertz polarisation nanoscopy, marking the first study of femtosecond dynamics in CrSBr. In the bulk, an ultrafast relaxation of hot excitons was observed, which may originate from scattering with phonons or short-lived magnetic fluctuations, that is, paramagnons. Furthermore, an ultrashort recombination of excitons on the timescale of 0.5 ps was unveiled, which is 30 times shorter than the lifetime in the bulk of 15 ps. By performing near-field spectroscopy combined with tunable photoexcitation, the spectral fingerprints of Coulomb-bound and unbound electron–hole pairs in bulk CrSBr are differentiated. Furthermore, the nonequilibrium dielectric function of a photoexcited monolayer of CrSBr has been extracted in a model-free manner, revealing the signatures of internal transitions between highly excited excitons. In the future, the employed ultrafast terahertz spectroscopy scheme may facilitate investigating the temporal and spectral signatures of coupling of excitons to the various magnetic phases in CrSBr. Moreover, the nanoscopic capabilities of our approach could ultimately allow one to explore the femtosecond dynamics of magnetic domains during phase transitions on the nanoscale.

Chapter 6

A novel versatile laser source for lightwave-driven nanoscopy

In the previous chapter, making use of the nanoscale resolution of sub-cycle terahertz near-field microscopy we studied the ultrafast dynamics of strongly correlated electron–hole pairs in CrSBr monolayers, whose lateral dimensions are much smaller than the diffraction limit of the terahertz probe pulses. Moreover, we found signatures of scattering of excitons with paramagnons, highlighting the strong interplay of magnetic and electronic structure in van der Waals magnets[24,25], even in the absence of long-range spin order. To gain deeper insights into spin–charge coupled quantum dynamics, ultimately, it is vital to explore them on their intrinsic, that is, *atomic* length scales. Moreover, the possibility to deliberately induce local, atom-scale disorder[148] and investigate it with Angstrom precision would be a powerful tool to shine light into the intricate interplay of the spin order and Coulomb-correlated electronic structure. Van der Waals layered magnets provide access to two-dimensional spin phenomena, and are thus an ideal test bed to investigate these strongly correlated quantum phenomena. With the exception of CrSBr, many currently known two-dimensional magnets are chemically unstable in ambient conditions and their magnetic order emerges at temperatures below 50 K[15,16]. Therefore, probing techniques operating at cryogenic temperatures and in vacuum are required.

Scanning tunnelling microscopy (STM) and spectroscopy are ideally suited to tackle all of these challenges: They combine operation at cryogenic temperature

and in ultra-high vacuum with single-quantum sensing and, importantly, control. Additionally, scanning tunnelling microscopes are compatible with spin-polarised tips and external magnetic fields, facilitating studies of spin currents with atomic spatial resolution. In the last years, lightwave-driven STM[58–62,149,150] has ushered in a new era of ultrafast nanoscopy. By coupling ultrashort, phase-stable terahertz pulses to the tip-sample junction, state-selective single-electron tunnelling with femtosecond temporal and sub-Angstrom spatial precision has been demonstrated in individual molecules[58]. Moreover, these terahertz pulses have been used as atom-scale femtosecond forces controlling the dynamics of a molecular frame[59]. Extending this scheme to semiconducting van der Waals magnets holds unprecedented possibilities of disentangling their strongly correlated quantum phases and discovering new emergent phenomena.

In collaboration with the group of Prof. Jascha Repp, we are currently realising a next-generation lightwave-driven scanning tunnelling microscope in Regensburg. Importantly, this experimental setup requires an optimised terahertz source. In this chapter, I will introduce a novel, flexible scheme for generation of ultrashort terahertz waveforms, which are ideally suited for the use in lightwave electronics and ultrafast scanning probe microscopy, particularly lightwave-driven STM. Exploiting an intriguing interplay of femtosecond shift currents and ultrafast screening in custom-tailored semiconductor heterostructures we generate phase-locked field transients featuring a unique combination of high repetition rate, large field strength and sub-cycle waveform. The fundamental principle of lightwave-driven STM will be briefly introduced in Section 6.1. The advantages and limitations of current sources of intense sub-cycle terahertz pulses are briefly discussed (Section 6.2), before our novel quantum well emitter concept is introduced and tested in Section 6.3.

6.1 Lightwave-driven scanning tunnelling microscopy

Scanning tunnelling microscopy (STM) caused a paradigm shift in nanoscience by introducing a technique capable of probing the electronic structure of nanoobjects with atomic resolution[151]. The ability to both resolve and even artificially assemble[152]

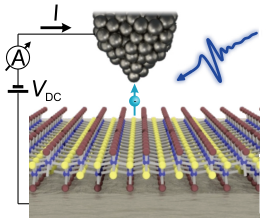

Figure 6.1 | Basic principle of steady-state and lightwave-driven STM. An atomically sharp tip rasters across the sample, while a bias voltage, V_{DC}, drives a tunnelling current, I. Replacing V_{DC} with a phase-stable light pulse (blue) coupled into the tip-sample junction allows one to drive currents with sub-cycle temporal definition.

surfaces with atom-scale precision has made STM an indispensable tool for solid-state research. Modern STM has facilitated, for example, imaging of individual molecules[153], read-out and writing of single spins[154] as well as resolving domain walls of correlated phases in solids[155].

Steady-state scanning tunnelling microscopy. The basic idea of STM is to utilise an atomically sharp metallic tip as a probe, which can be rastered across a sample (Figure 6.1). When the electronic wave functions of the tip apex and the sample overlap, an external bias voltage, V_{DC}, can drive a tunnel current, I, that sensitively depends on the tip-sample distance and the atom-scale density of states. Consequently, when the tip is scanned across the sample, a steady-state map of the sample topography can be retrieved via the tunnel current. Modern scanning tunnelling microscopes routinely allow imaging of surfaces with angstrom lateral and picometre vertical resolution. However, the bandwidth of the electronic circuitry limits the temporal definition of the tunnel currents to time windows on the order of nanoseconds[156].

In the last decades, a multitude of schemes has been developed attempting to combine ultrafast lasers with STM to trigger tunnelling events confined to (sub-)picosecond time windows[157–160]. However, optical excitation of either photoconductive switches transiently closing the tunnelling circuitry or the tip-sample junction directly come with limitations such as capacitive charging, a restricted choice of samples and thermal input leading to expansion of the tip. Moreover, local electron heating and multiphoton excitation may drive the tip-sample system out of equilibrium, such that the dynamics of the sample and the microscope need to be disentangled.

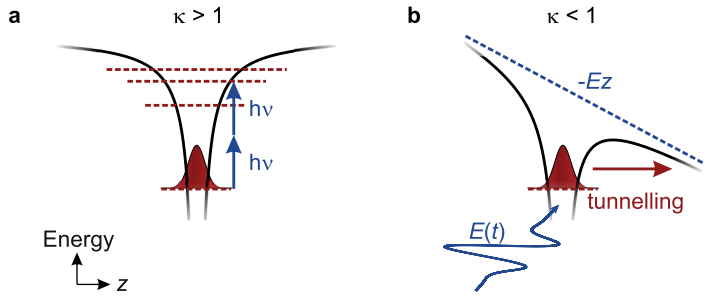

Figure 6.2 | Regimes of light-matter interaction. An electromagnetic wave can interact with an electronic state (red wavepacket) bound to a schematic potential landscape (black lines) in two extreme ways: **a**, At a Keldysh parameter $\kappa > 1$, (multi-)photon excitation (blue arrows) to energetically higher states dominates. **b**, In the strong-field regime, $\kappa < 1$, the electric field $E(t)$ tilts the potential landscape (black line) with a slope $-Ez$ (dashed blue line), such that electron tunnelling (red arrow) is possible.

Lightwave control. One can avoid these complications by directly replacing the DC bias between tip and sample with the instantaneous electric field of an ultrashort light pulse. This idea can be realised in a regime of light-matter interaction, where an intense lightfield even competes with the inter-atomic Coulomb interaction. In contrast to the diametrically opposed pole of light-matter interaction dominated by mutliphoton absorption (Figure 6.2a), strong lightwaves can be harnessed to steer electron motion within fractions of an oscillation cycle (Figure 6.2b). This concept is the foundation of lightwave electronics[161,162], where lightwave-driven electronic coherences are driven much faster than scattering. In this way, extremely sub-cycle currents have been driven[163–166] down to atomically thin solids[167–169] and even individual molecules[58,59], providing an ideal framework for ultrafast, *lightwave-driven* STM.

Lightwave-driven tunnelling. The key idea of lightwave-driven STM is to couple a suitable light pulse to the tunnelling junction, where the carrier wave translates into a quickly oscillating electric bias. In this way, under certain conditions, even sub-cycle control of the tunnelling current is feasible. To ensure that the laser pulse

interacts like a classical wave with the tip-sample system, the Keldysh parameter[170],

$$\kappa = \sqrt{\frac{\varepsilon}{2U_\mathrm{p}}} = \frac{\omega\sqrt{2m\varepsilon}}{eE}, \tag{6.1}$$

which specifies the regime of light-matter interaction, is a helpful measure. It compares the excitation energy, ε, to the ponderomotive energy, $U_\mathrm{p} = \frac{e^2E^2}{4m\omega^2}$, which is the kinetic energy a free electron would acquire by field-induced acceleration within one optical cycle. E and ω describe the amplitude of the electric field and the frequency of the driving field, respectively. m and e are the electron mass and charge. A Keldysh parameter, $\kappa > 1$, indicates a dominant contribution of (multi-)photon excitation, while in the strong-field regime ($\kappa < 1$) the electromagnetic wave accelerates charges and distorts the potential landscape. Lightwave-driven processes are associated to the latter regime and achieved by relatively low oscillation frequencies, ω and large field strengths, E.

(Multi-)Terahertz pulses are ideally suited to drive ultrafast, sub-cycle tunnel currents for a number of reasons: First, while the frequency is low compared to optical waves, promoting field-driven light-matter interaction, the corresponding (sub-)picosecond oscillation periods are fast enough to resolve the dynamics of a plethora of low-energy excitations in condensed matter. Moreover, nonlinear optics provides a powerful toolbox to generate extremely intense and tailorable terahertz waveforms for flexible and precise lightwave control. A first demonstration of terahertz-driven STM has been given in Reference 171, where an intense terahertz pulse drove large rectified tunnel currents through metallic nanoobjects in ambient air in a sub-picosecond time window. Later, phase-locked sub-cycle terahertz transients enabled lightwave-driven, *state-selective* tunnelling through an individual molecule with single-electron control and combined angstrom spatial and femtosecond temporal definition[58].

The principle of state-selective lightwave-driven tunnelling is depicted in Figure 6.3a-c. An external bias, tilts the potential landscape of the system encompassing substrate (s), molecule (m) and tip (t). For a voltage, V, which aligns the Fermi energy of the tip with a molecular resonance, for example the highest occupied molecular orbital (HOMO), sequential tunnelling through the HOMO is allowed (Figure 6.3a). This process manifests itself as a peak in the differential conductance

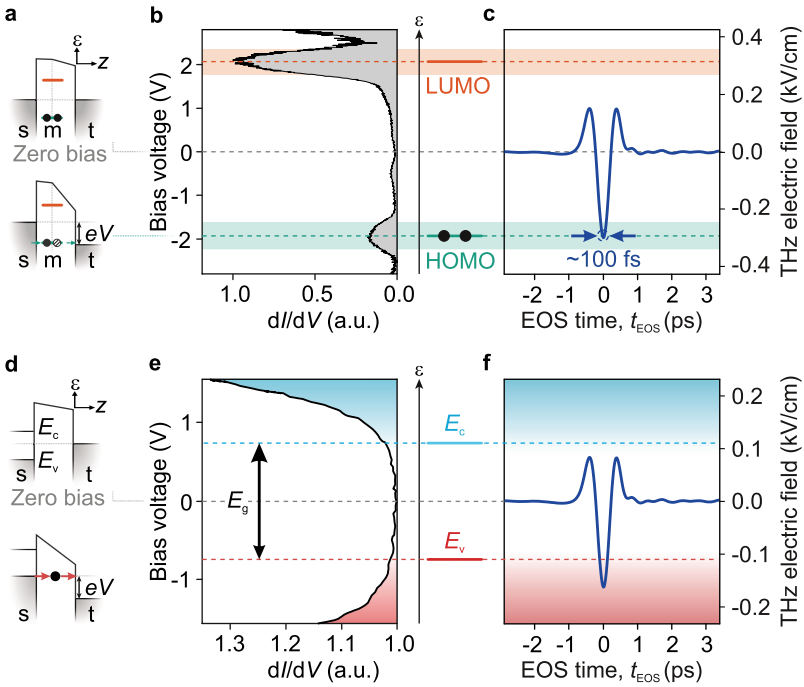

Figure 6.3 | Lightwave-driven tunnelling. **a**, One-dimensional potential landscape of a single-molecule tunnelling junction. At zero bias no tunnelling can occur via molecular resonances (m). A bias voltage, V, matching a resonance triggers sequential tunnelling from the substrate (s) into the tip (t) via the molecular orbital. **b**, Differential conductance spectrum featuring molecular orbitals appearing as peaks. **c**, An intense phase-stable electric-field transient can replace the DC bias, resulting in a state-selective tunnelling window of ∼100 fs. **d**, Potential landscape for a semiconducting sample (s) with conduction and valence band energies, E_c and E_v, respectively. A bias voltage, V, exceeding the difference of either E_c or E_v and the Fermi energy drives a tunnel current. **e**, Differential conductance map of the semiconductor CrSBr from Reference 19. **f**, A highly asymmetric waveform is required to drive unidirectional tunnel currents. Adapted from Reference 58.

(Figure 6.3b). An electric field waveform coupled to the tip-sample junction can provide a transient bias, which, when the peak bias is fine-tuned to a molecular resonance, opens a tunnelling window confined to the field crest of the waveform (Figure 6.3c). At a terahertz centre frequency of 1 THz this time window can be as short as 100 fs (Reference 58), corresponding to one tenth of an optical cycle.

Similarly, solids featuring electronic bands can be imaged with the help of lightwave-driven STM, although the microscopic picture slightly differs. The electronic structure of semiconductors is characterised by continua of states below the valence band edge, E_v and above the conduction band edge, E_c, separated by the bandgap, E_g. When a bias exceeding the difference of the Fermi energy and either E_v or E_g is applied, electrons can tunnel from the valence band into the tip or, vice versa, from the tip into the conduction band, respectively (Figure 6.3d). This is reflected as a steep increase of the differential conductance above the respective band edge energy, depicted in Figure 6.3e for the example of bulk CrSBr[19]. In the lightwave picture (Figure 6.3f), the electric-field transient will drive electron tunnelling from a continuum described by the atom-scale local density of states rather than an individual state.

Requirements for the laser source. The functional principle of lightwave-driven STM relies on a multitude of technologically demanding features of the optical source. First, already evident in Figure 6.3c, the electric-field transient must exhibit a duration much shorter than an oscillation cycle of the carrier wave. In the frequency domain, such a pulse consists of an *octave-spanning* spectrum of Fourier components, which, importantly, have to oscillate in phase. Simultaneously, an *asymmetric*[a] waveform is required to drive *unipolar* lightwave-steered tunnel currents into or through well-defined states, only once per laser pulse. The asymmetry gains even more significance, when one wishes to investigate semiconductors with lightwave-driven STM: While molecular resonances can be shifted with respect to the Fermi level of the tip-sample system by choice of the substrate[58,153], in semiconductor samples the onset of tunnelling occurs at fairly equal magnitudes of the bias voltage. Furthermore, for experiments using laser pulse trains, the carrier-envelope phase of the electric field waveforms must be fixed (Figure 6.4), such that every pulse opens an identical tunnel window.

[a] In this thesis, the asymmetry of a waveform is defined with respect to the time axis.

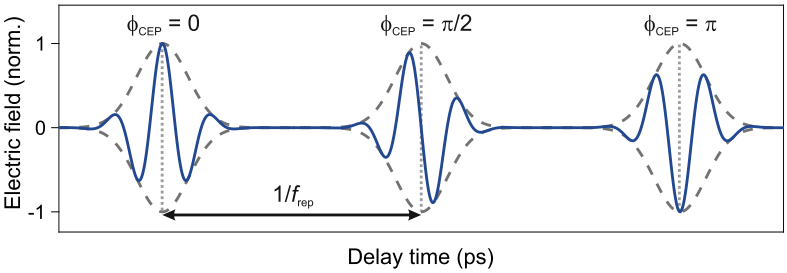

Figure 6.4 | The carrier-envelope phase. The carrier-envelope phase, ϕ_{CEP}, between the carrier wave (blue line) and the field envelope (grey dashed lines) of an ultrashort pulse drastically influences the waveform. The vertical grey dotted lines indicate the maximum of the field envelope. Consecutive pulses are delayed by the inverse repetition rate, f_{rep}, which is strongly understated here for illustration purposes.

A further fundamental requirement for lightwave control in STM is a high field strength: In the tunnel junction, the lightwave has to provide a peak electric field that translates into a voltage on the order of 1 V. Consequently, for a tip-sample distance of 1 Å, an electric field of $\sim 1\,\mathrm{V\,Å^{-1}} = 100\,\mathrm{MV\,cm^{-1}}$ is needed. Since the extreme confinement of the lightfield to the atom-scale tip-sample junction results in a large field enhancement[61] on the order of 10^5, far field amplitudes of around $1\,\mathrm{kV\,cm^{-1}}$ will induce atomically strong fields across the tunnel junction.

Lastly, the lightwave-driven current is directly proportional to the laser repetition rate. In the regime of state-selective tunnelling, where typically less than one electron is tunnelled per pulse[58,61], a high laser repetition rate is indispensable to achieve practical signal-to-noise ratios. State-of-the-art scanning tunnelling microscopes can be operated at a noise level of $\sim 100\,\mathrm{fA}$, which, in a single-electron tunnelling regime, corresponds to a tunnelling rate of $\sim 600\,\mathrm{kHz}$. Therefore, an ideal optical source enabling feasible acquisition times should operate at megahertz repetition rates. While individually, the requirements listed above are routinely met by contemporary terahertz sources, simultaneously fulfilling them poses a serious challenge, even for state-of-the-art laser technology.

6.2 Generation of intense sub-cycle terahertz pulses at high repetition rates

The ideal ultrashort bias for lightwave-driven STM resembles a spike function, which is usually modelled as a Dirac delta distribution. However, in the far field, Maxwell's equations require that the integral over the field transient must vanish[172]. Therefore, we aim for a maximally asymmetric, strongly sub-cycle terahertz pulse, whose positive field maximum greatly exceeds any negative field excursion. To realise such a waveform, an ultrabroadband, octave-spanning frequency spectrum featuring a flat, zero-valued phase is required. This section will elaborate on established techniques to generate sub-cycle terahertz waveforms. Subsequently, a novel, scalable scheme for the generation of intense sub-half-cycle terahertz pulses at high repetition rates, which was developed in this work, is presented.

Generating ultrashort terahertz pulses. Generally, to generate an electromagnetic wave oscillating at terahertz frequencies ω_{THz}, either a time-dependent charge current density, $\boldsymbol{j}_{\mathrm{c}}(t)$, or polarisation featuring Fourier components at ω_{THz} is required[125]. Most techniques to generate ultrashort terahertz waveforms employ femtosecond visible or near-infrared laser pulses as a pump source. As their optical carrier waves oscillate at frequencies of multiple 100 THz, only a *nonlinear* response to the driving field can trigger the desired frequency downconversion over two orders of magnitude.

Over the last decades, a wide variety of nonlinearities in dielectrics, metals and gases have been exploited to efficiently generate broadband phase-locked terahertz pulses. We now consider the most relevant techniques for generating phase-locked terahertz pulses in terms of bandwidth, intensity and achievable repetition rate. Based on these figures of merit, the eligibility as a source for lightwave-driven STM is assessed. The following brief discussion is based on the more comprehensive review given in Reference 173.

Photoconductive antennas. Photoconductive switches are a wide-spread approach to generate broadband terahertz pulses. The emission principle is based on the acceleration of photoexcited carriers in a semiconductor by an external bias

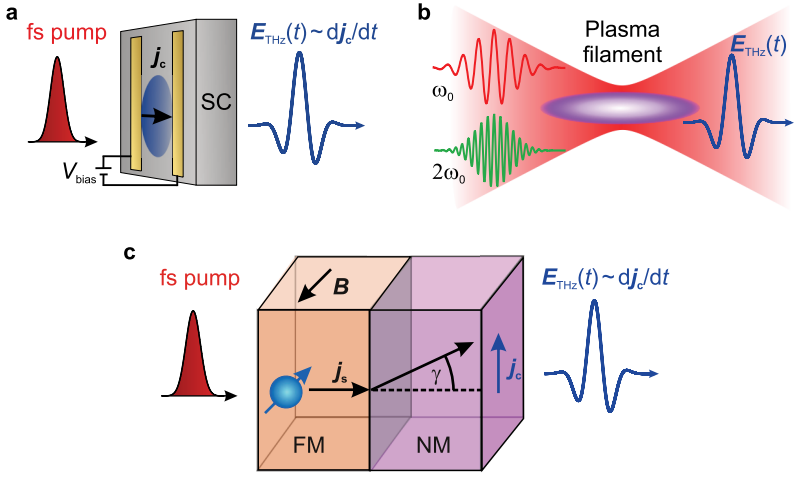

Figure 6.5 | Established techniques for generation of intense sub-cycle terahertz waveforms. **a**, Photoconductive switches. An external bias voltage, V_{bias}, accelerates carriers (blue) generated by a femtosecond laser pulse (red). The resulting in-plane charge current, $\boldsymbol{j}_{\mathrm{c}}$, leads to emission of a terahertz transient, $\boldsymbol{E}_{\mathrm{THz}}$, to the far field. **b**, Two-color laser filaments. In a plasma filament (purple) driven by an intense laser field (red, frequency ω_0) and its second harmonic (green, frequency $2\omega_0$) tunnelionised electrons are accelerated by the two-color field. The transversal plasma current exhibits a finite quasi-DC component generating a terahertz waveform, $\boldsymbol{E}_{\mathrm{THz}}$. **c**, Spintronic emitters. A femtosecond pump pulse excites electrons of majority spin (blue) in an in-plane magnetised ferromagnetic layer (FM). The inverse spin Hall effect (spin Hall angle, γ) converts the resulting superdiffusive spin current, $\boldsymbol{j}_{\mathrm{s}}$, into a transversal charge current, $\boldsymbol{j}_{\mathrm{c}}$, in the adjacent nonmagnetic layer (NM) generating a terahertz transient, $\boldsymbol{E}_{\mathrm{THz}}$.

(Figure 6.5a). The resulting in-plane current leads to the emission of a phase-stable terahertz pulse into the far field, as demonstrated by Auston *et al.*[174] in a silicon antenna. Recently, sub-cycle mid-infrared transients with a gapless spectrum were generated in germanium photoconductive antennas[175]. Scaling these emitters to high pulse energies, however, has proven to be difficult as the photogenerated carriers screen the external bias resulting in a reduced conversion efficiency for large pump intensities[176].

Difference frequency generation. One of the most multifaceted and widely used techniques to generate intense terahertz pulses is difference frequency generation. Optical rectification, a special case of difference frequency generation, has already been introduced in Chapter 3: When a broadband laser pulse containing frequencies ω_1 and ω_2 interacts with a noncentrosymmetric dielectric, its second-order nonlinear response causes the re-emitted radiation to contain Fourier components at the difference frequency $\omega_{\mathrm{THz}} = \omega_1 - \omega_2$. Difference frequency generation allows one to generate intrinsically phase-locked, (multi-)terahertz waveforms with atomically strong fields[177,178] and ultrabroadband spectra[45,179]. However, the presence of optical phonons in $\chi^{(2)}$ media gives rise to the so-called Reststrahlen band, preventing the generation of gapless ultrabroadband spectra.

Two-color laser plasmas. Extremely intense and intrinsically sub-cycle terahertz pulses can be generated in laser-induced gas plasmas, first demonstrated in a terawatt laser system[180]. The originally low conversion efficiency was drastically improved by mixing the laser fundamental with its second harmonic[181], facilitating the use of table-top laser amplifiers for this emission scheme. As shown in Figure 6.5b, the generation process is based on focusing intense laser pulses and their second harmonic, creating a long plasma filament. There, bound electrons are tunnelionised and coherently driven by the two-color laser field. Since the resulting current contains a quasi-DC component, strongly asymmetric multi-terahertz field transients[182] featuring ultrabroadband, gapless spectra can be generated with an exceptional energy conversion efficiency of several percent[183]. Due to the large pulse energies required for plasma generation on the order of 1 mJ, the repetition rate is limited to the kilohertz range in current table-top setups.

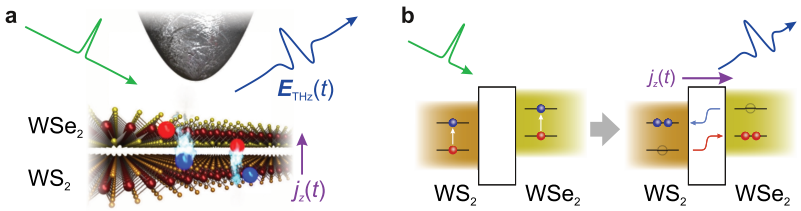

Figure 6.6 | Terahertz emission from spatially indirect interband transitions. a, Photoexcitation of electron–hole pairs in a WSe_2/WS_2 heterostructure with a pump pulse (green) is followed by interlayer tunnelling giving rise to a terahertz waveform detected in a near-field experiment. **b**, Due to the type-II band alignment of the WSe_2/WS_2 heterostructure electrons and holes spatially separate after photoexcitation. The resulting ultrashort current spike, $j_z(t)$, generates a terahertz transient. Adapted from Reference 56.

Spintronic emitters. Spintronic emitters have marked a breakthrough for the generation of intense sub-cycle terahertz pulses with gapless spectra at high repetition rates[184]. In their simplest form, these metallic heterostructures consist of a ferromagnetic and a nonmagnetic layer (Figure 6.5c). When a femtosecond laser pulse excites the magnetised ferromagnetic layer, the majority spin carriers are excited into high-mobility *sp*-like states, whereas the minority spin carriers are promoted to *d*-like states with much lower mobility[185]. As a result, a superdiffusive spin current is launched towards the nonmagnetic layer. There, the inverse spin Hall effect converts the spin current into a transversal charge current, which gives rise to an intrinsically phase-locked, sub-cycle terahertz waveform. Owing to the absence of infrared-active phonons in these metallic heterostructures terahertz waveforms with gapless, octave-spanning spectra have been demonstrated at megahertz repetition rates[184]. Therefore, spintronic emitters are the current gold standard for the generation of ultrabroadband terahertz transients at high repetition rates. However, the small optical skin depth of metals prevents effective scaling of these emitters by stacking multiple active layers[186].

Spatially indirect interband transitions. An intriguing alternative mechanism for generation of ultrashort terahertz waveforms has recently been observed in van

der Waals heterostructures[46,56,106] (Figure 6.6): When a femtosecond optical pulse (green) excites electron–hole pairs in a WSe_2/WS_2 heterobilayer featuring type-II band alignment, interlayer transfer of the photogenerated carriers gives rise to an out-of-plane shift current pulse. This process results in emission of a strictly sub-cycle terahertz waveform (blue), which has been revealed by near-field probe techniques[56,106]. As a result of the atomically thin nature of the heterostructure, the emitted field strengths are weak, only on the order of $1\,\mathrm{V\,cm^{-1}}$ (Reference 56). Moreover, the delicate stacking of monolayer crystals curtails the scalability of the emitter. Nevertheless, owing to the intrinsically phase-locked and sub-cycle nature of the generated terahertz waveforms, spatially indirect interband transitions are a promising generation scheme.

Encouraged by this potential, we developed a novel, *scalable* shift-current-based scheme to generate intense ultrashort terahertz pulses, which will be presented in the next section. The discussion of the results in the remainder of this chapter follows the presentation in Reference 187.

6.3 Novel terahertz emitters based on spatially indirect interband transitions

The inherently fixed resonances of van der Waals heterostructures demand a specific pump wavelength and offer little freedom of design to custom-tailor the terahertz emission. In contrast, epitaxially grown semiconductor heterostructures provide a flexible platform to match transition energies to a pump source of choice: By controlling the material composition, thickness of the quantum wells and barriers with atomic precision, one can engineer the bandgap and offsets as well as subband energies and wavefunctions such that the probability densities of electrons and holes are localised at opposite sides of the heterostructure. Resonant optical excitation of spatially separated electron–hole pairs is then expected to launch a quasi-instantaneous shift current. As opposed to schemes that require tunnelling through a barrier, limiting the charge transfer[188], one can then expect efficient emission of an ultrabroadband, phase-locked and sub-cycle terahertz transient. Furthermore, when lattice-matched

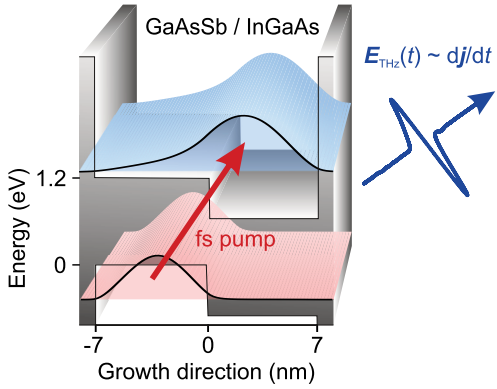

Figure 6.7 | Concept of terahertz generation from a quantum well emitter. When an intense femtosecond laser pulse (red arrow) resonantly generates electron–hole pairs (blue and red envelopes, respectively) in a type-II aligned quantum well, an ultrafast dipole moment is expected, which gives rise to emission of an intrinsically sub-cycle terahertz waveform.

alloys are employed, strain-free growth allows one to readily scale a potential emitter by stacking multiple repetitions of the layer structure.

Shift-current-based terahertz emitters. Shift current sources of ultrashort terahertz pulses have been realised by photoexcitation of electron–hole pairs in DC-biased quantum wells[189,190] and intersubband transitions in asymmetric quantum wells[191]. Hitherto, no shift current source has been scaled to high-power pump lasers to generate intense terahertz pulses at high repetition rates. In this work, a scalable source of strongly asymmetric terahertz waveforms was designed by transferring the concept of spatially indirect interband transitions in type-II aligned nanostructures to asymmetrically coupled epitaxial heterostructures[187]. The novel emitter scheme is shown in Figure 6.7: The confinement potential of a semiconductor quantum well (grey area) is engineered such that the electronic wavefunctions are separated by several nanometres without any external bias. When the lowest conduction subband (blue) and highest valence subband (red) are populated via resonant interband excitation (red arrow), an ultrafast shift current is expected. As a result of the large separation between electron and hole wavefunction of multiple unit cells, a large dipole moment can be generated, giving rise to an intense terahertz pulse (blue).

Expected terahertz waveform. First, we employ a simplistic model to grasp the expected terahertz waveform. As the out-of-plane motion in the quantum wells

is fully quantised, carrier diffusion plays no role as opposed to schemes utilising in-plane shift currents[192,193]. Thus, when the confinement potential is assumed to be static, femtosecond interband excitation creates an ultrashort unidirectional shift current burst. According to Maxwell's equations, the terahertz electric field E_{THz} follows the time derivative of the shift current, j, which, in a minimalistic model, can be described with a rate equation,

$$j(t) \sim \frac{\mathrm{d}n_{\mathrm{eh}}(t)}{\mathrm{d}t} \sim S_{\mathrm{pump}}(t) - \frac{n_{\mathrm{eh}}(t)}{\tau}, \tag{6.2}$$

where n_{eh} and τ are the density and recombination time of photoexcited electron–hole pairs, respectively. S_{pump} is a source term with the temporal shape of the intensity envelope of the pump laser. Figure 6.8 shows the calculated out-of-plane current and emitted electric field for a pump pulse duration of 140 fs. Owing to the small transition matrix element of the electron and hole wavefunction resulting from their spatial separation, the recombination times should greatly exceed the pump pulse duration. For both $\tau = 1\,\mathrm{ps}$ (black) and $\tau = 1\,\mathrm{ns}$ (blue) photoexcitation of spatially separated electron-hole pairs produces a prominent positive current spike, which is followed by a significantly weaker negative current stretched over a long duration determined by the recombination time (see Figure 6.8a). For both values of τ, the emitted electric field waveform, which is obtained by taking the time derivative of j, comprises only two equally strong oscillation half cycles without any leading or trailing oscillations (Figure 6.8b). Although the carrier-envelope phase of the transient is not yet ideal for lightwave-driven STM, such an ultrashort terahertz pulse featuring an intensity envelope much shorter than an oscillation cycle provides an excellent foundation to drive sub-cycle tunnelling currents. In Section 6.3.3, we will discuss an elegant way to control the phase of the terahertz waveform.

The next section introduces the compact, high-repetition-rate experimental setup, which was specifically designed to pump the novel quantum well emitters with intense, ultrashort near-infrared pulses.

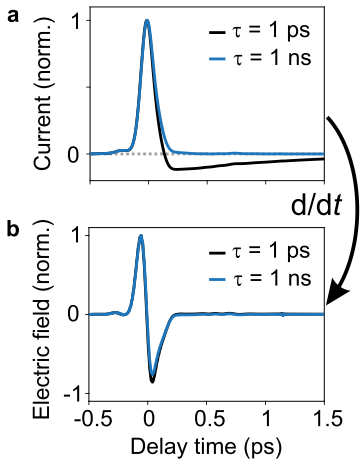

Figure 6.8 | Simplistic model of the emitted terahertz waveform. **a**, Calculated time-dependent shift current resulting from photoexcitation of spatially indirect electron–hole pairs by a laser pulse with a duration of 140 fs, assuming a static quantum well potential. The ultrashort positive current spike is followed by a slowly decaying negative current caused by recombination (black curve: recombination time, $\tau = 1$ ps, blue curve: $\tau = 1$ ns.) **b**, For recombination times much larger than the duration of the excitation pulse, the emitted waveform consists of only two equally strong oscillation half cycles.

6.3.1 Experimental setup for terahertz generation and phase-resolved detection

To put the proposed quantum well terahertz emitter to the test, a simultaneously maximally flexible and stable, high-power and high-repetition-rate table-top laser setup is required to both generate and detect intense terahertz waveforms featuring octave-spanning spectra. The building blocks of our experimental terahertz generation and diagnostics setup uniting these capacities are depicted in Figure 6.9. In order to achieve field strengths sufficient to drive sub-cycle tunnelling currents, the quantum well emitter scheme described above is designed to be compatible with a high-power pump source. Here, we make use of bandgap engineering in epitaxial semiconductor heterostructures to tune the interband transitions to the wavelength of a state-of-the-art ytterbium fibre laser (1030 nm $\hat{=}$ 1.2 eV). As the bandwidth of the terahertz pulses is expected to scale inversely with the pump pulse duration, the shortest pump pulses possible are desirable. We therefore utilise a flexible and highly efficient pulse compression scheme based on self-phase modulation in a multipass cell. The compressed pulses are then used both to pump the quantum well emitters and to gate the generated terahertz waveforms in an ultrabroadband electro-optic sampling

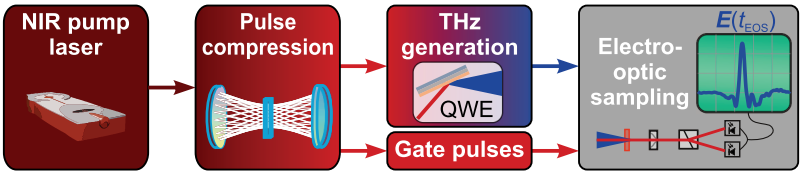

Figure 6.9 | Schematics of the experimental setup for generation and field-resolved of terahertz waveforms from quantum well emitters. Near-infrared (NIR) femtosecond pulses from an ytterbium fibre laser are compressed in a multipass cell and act both as pump for the quantum well emitter (QWE) and gate pulses in the electro-optic sampling that enables tracing the exact terahertz electric-field waveform, $E_{\mathrm{THz}}(t_{\mathrm{EOS}})$.

scheme that allows us to retrieve the electric field waveform. This section provides a step-by-step description of the functional units of the setup and the underlying nonlinear optical techniques.

Spectral broadening and compression of intense laser pulses. Generating terahertz pulses with large peak fields on the order of $1\,\mathrm{kV\,cm^{-1}}$ at megahertz-level repetition rates calls for a near-infrared pump source capable of generating high average powers. For this purpose, ytterbium-based ultrafast laser systems are the ideal choice as they can provide femtosecond pulses with large pulse energies at high repetition rates[194–197]. However, owing to the finite gain bandwidth in ytterbium fibre lasers, the pulse duration of these lasers is usually well above 100 fs, limiting the achievable terahertz bandwidth. This constraint has triggered significant progress in development of highly efficient external pulse compression schemes[198–204] that typically rely on nonlinear spectral broadening via self-phase modulation. The latter is a consequence of the optical Kerr effect, a $\chi^{(3)}$ nonlinearity, which at sufficiently high intensities gives rise to an intensity-dependent refractive index,

$$n(I(t)) = n_0 + n_2 I(t), \tag{6.3}$$

where n_0 and n_2 denote the linear and nonlinear refractive index, respectively and $I(t)$ is the intensity envelope of the laser pulse (see Figure 6.10a, red solid line). As a result, a linearly polarised electromagnetic wave oscillating at frequency ω_0 and

propagating along the z axis undergoes a nonlinear phase shift[125]

$$\varphi_{\mathrm{NL}} = \frac{\omega_0}{c} n_2 I(t) z, \tag{6.4}$$

where c denotes the vacuum speed of light (see Figure 6.10b, red solid line). As the instantaneous frequency, ω_{inst}, is given by

$$\omega_{\mathrm{inst}} = \omega_0 - \frac{\partial \varphi_{\mathrm{NL}}}{\partial t}, \tag{6.5}$$

new frequency components are generated and the spectrum is symmetrically broadened around the centre frequency (see Figure 6.10c, red solid line). At higher intensities, the effect of self-steepening[205] has to be taken into account: Since the most intense, central part of the laser pulse experiences a higher refractive index, it is delayed with respect to the leading edge of the pulse. As a result, the temporal intensity distribution and, thus, the nonlinear phase shift φ_{NL} are distorted (Figure 6.10a,b, black dashed lines). Consequently, as seen in Figure 6.10c (black dashed line), self-steepening leads to an asymmetric broadening of the laser spectrum, where the steepened back of the laser pulse generates a stronger blue shift compared to the red shift induced by the smoothed front of the temporal intensity envelope.

Self-phase modulation of intense laser pulses is always accompanied by self-focusing, which is another effect of the intensity-dependent refractive index. Most lasers emit light in a Gaussian beam profile and, according to Equation (6.3), the change in the refractive index assumes an identical spatial shape (Figure 6.10d,e). Hence, the light-induced gradient of the refractive index in the nonlinear medium along the radial coordinate of the beam focuses the laser pulse. Above a so-called critical power, self-focusing outweighs diffraction, leading to deterioration of the beam quality or even damaging of the nonlinear medium[125]. Therefore, it is imperative for efficient compression schemes to mitigate the effect of self-focusing, while maximising spectral broadening by self-phase modulation. Gas-filled hollow-core photonic crystal fibres[198] are an elegant way to achieve extreme spectral broadening with low losses[199,200,204,206]. Owing to the large critical power of gases, degradation of the beam quality caused by self-focusing can be averted. However, at simultaneous high average and peak powers,

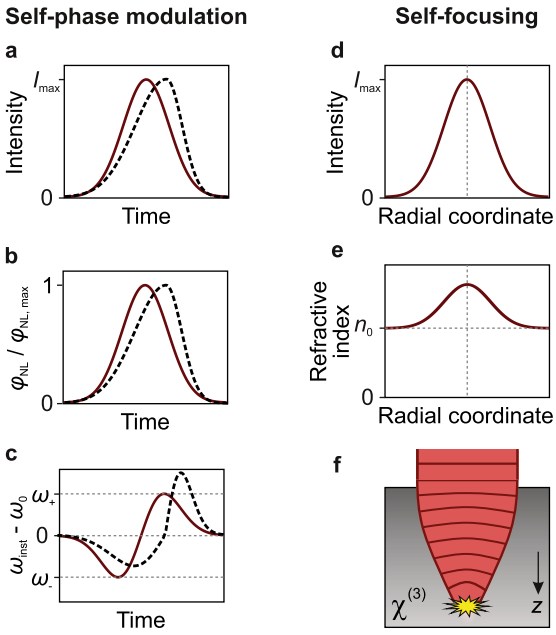

Figure 6.10 | Self-phase modulation and self-focusing a, Gaussian intensity envelope (red) of an intense laser pulse as a function of time. **b**, The nonlinear phase shift φ_{NL} induced by self-phase modulation has the same temporal structure as the intensity envelope and leads to **c**, generation of new frequency components. Simultaneously, owing to the Gaussian shape of φ_{NL} the centre of the pulse is delayed with respect to the low-intensity flanks, resulting in self-steepening (black dashed lines in **a**-**c**). **d**, The spatial intensity distribution of a Gaussian beam transversal to the direction of propagation in a $\chi^{(3)}$ medium induces **e**, an equally shaped change of the refractive index. **f**, As a consequence of the intensity dependent refractive index, the wavefronts become convergent (red lines), causing so-called self-focusing.

photonic crystal fibres are sensitive to alignment and prone to damage, impairing the longevity and stability of the optical setup.

Nonlinear spectral broadening in bulk media inside multipass cells[201–203] is a more robust technique to compress ultrashort laser pulses with high efficiency and excellent output beam quality. The basic idea is sketched in Figure 6.11: An intense laser pulse is repeatedly focused into a nonlinear $\chi^{(3)}$ medium, where it is broadened by self-phase modulation. For each pass through the broadening medium, the focal diameter is chosen to be large enough for the peak power to be well below the critical power and thus, self-focusing can be neglected. The corresponding optical transfer matrix, T_{SP}, which entails a focusing element L and free-space propagation over the distance, d, can be transferred to a more compact and stable resonator configuration.

A suitable multipass geometry is the Herriott cell[207], which consists of two concave mirrors facing each other on a common optical axis (see Figure 6.11b). When a beam is coupled into the cell via a small pickoff mirror in front of one of the cell mirrors, the reflections on each cell mirror form an elliptical pattern (see Figure 6.11c). By tuning the distance, d, between the mirrors, one can adjust the angle θ between two consecutive reflections. In this way, the laser pulses to be broadened can traverse a nonlinear medium placed within the cell multiple tens of times before they are coupled out via the pickoff mirror. Notably, to emulate the beam caustic depicted in Figure 6.11a, where the beam waist is located in the centre between the two focusing elements, mode matching is required to keep the focus in the symmetry plane of the Herriott cell for every pass. To this end, the Gaussian beam parameter, q_0, outside the cell is conditioned with a telescope, such that q_k is constant for every single pass, k, inside the multipass cell, which is described by the transfer matrix, T_{SP}. In a mode-matched Herriott cell, the amount of spectral broadening can then be tuned without changing the input pulse energy: By moving the $\chi^{(3)}$ medium along the optical axis of the cell, the laser intensity inside the medium and thus, the nonlinear phase shift can be readily varied. This flexibility can later be exploited to test the achievable bandwidth of terahertz pulses from our novel quantum well emitters.

In this work, in collaboration with Prof. Oleg Pronin and Kilian Fritsch, we designed and built a compact, home-built Herriott compression cell to spectrally broaden and simultaneously compress intense near-infrared pump pulses from an ytterbium fibre amplifier. Both spherical cell mirrors have a radius of curvature of

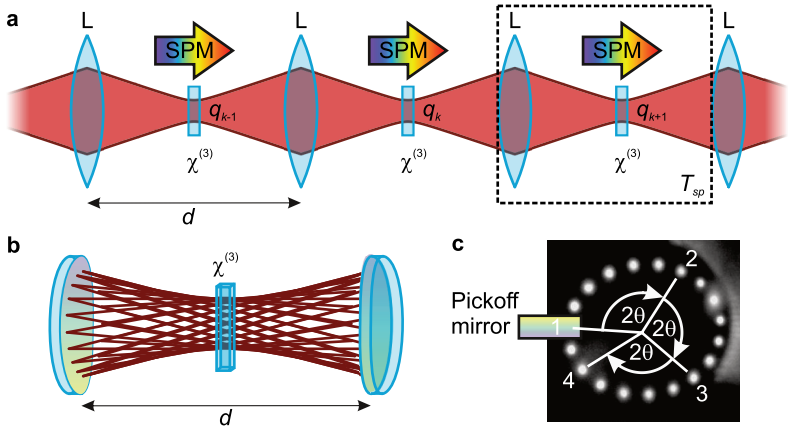

Figure 6.11 | The multipass or Herriott cell. **a**, An intense laser pulse with Gaussian beam parameter, q, is repeatedly focused into a $\chi^{(3)}$ medium, where it is broadened by self-phase modulation (SPM). A single pass through the cell can be described by a transfer matrix, T_{SP}, including a focusing optical element (L) and free-space propagation over the distance d. **b**, Compact realisation of the beam path in a Herriott cell with 38 passes. **c**, Mode pattern on a cell mirror, imaged by an infrared camera. The first four reflections on the mirror are numbered exemplarily. The constant angular separation between two subsequent reflections is denoted as 2θ. The pulses are coupled in and out via a rectangular mirror (pickoff mirror).

500 mm and are placed $d = 773$ mm apart. In this geometry, the nonlinear medium, a fused silica window with a thickness of 6.35 mm, which is coated with an anti-reflection coating, is passed 38 times by the laser pulses. Notably, even though the optical path in the Herriott cell exceeds 30 m, as a result of the self-imaging resonator geometry, the beam pointing stability is not significantly affected. When we couple laser pulses from an ytterbium fibre laser (pulse duration, 140 fs; pulse energy, 10 µJ; repetition rate, 4 MHz) into the multipass cell, they are spectrally broadened in the $\chi^{(3)}$ medium as shown in Figure 6.12: The fundamental laser spectrum is centred at 1.19 eV and has a FWHM bandwidth of 25 meV (6 THz). The most spectrally broadened spectrum, which is achieved when the broadening medium is placed in the centre of the multipass cell, exhibits a FWHM bandwidth of 47 meV (11 THz).

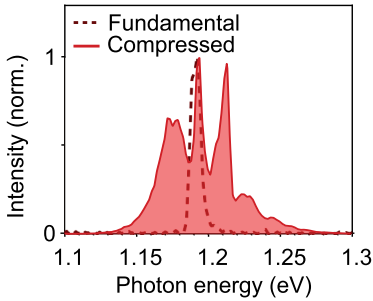

Figure 6.12 | Broadened pump and gate spectrum. Spectral intensity of the unbroadened fundamental (dashed dark red line) laser pulses and the compressed (solid red line) laser pulses, acting both as pump and gate. The full width at tenth maximum bandwidth is increased from 30 meV (7.2 THz) to 92 meV (22.4 THz), supporting a compressed pulse duration of 30 fs.

Owing to the structured spectrum of the broadened pulses, the full width at tenth maximum (FWTM) of the intensity provides a more accurate characterisation: While the fundamental spectrum features a FWTM width of 30 meV (7.2 THz), the pulses after the compression cell support a significantly larger FWTM bandwidth of 92 meV (22.4 THz).

Typically, to temporally compress the spectrally broadened pulses one utilises either a prism or grating compressor or a pair of chirped mirrors, which compensate for the group delay dispersion. Here, we operate the multipass cell in the self-compression regime, which is realised by chirped cell mirrors with a group delay dispersion of $-150\,\mathrm{fs}^2$ compensating both the linear dispersion of the broadening medium of ca. $130\,\mathrm{fs}^2$ (Reference 208) and the quadratic part of the nonlinear phase induced by self-phase modulation. As a consequence, the laser pulses are compressed within the cell and coupled out with a duration close to the Fourier limit. The most compressed pulses have a duration of 30 fs, corresponding to a compression by a factor of almost five (see Appendix C.1 for details). Furthermore, an outstanding power efficiency of 90% is achieved, which is only limited by the quality of reflective coatings of the cell mirror and the anti-reflection coating of the fused silica medium.

Terahertz generation and phase-sensitive detection. The combination of a high-power ytterbium fibre laser and an efficient pulse compression constitutes an ideal pump source to generate simultaneously intense and sub-cycle multi-terahertz field transients. Furthermore, employing the compressed pulses as gate in electro-optic sampling facilitates ultrabroadband detection bandwidth. Figure 6.13 depicts

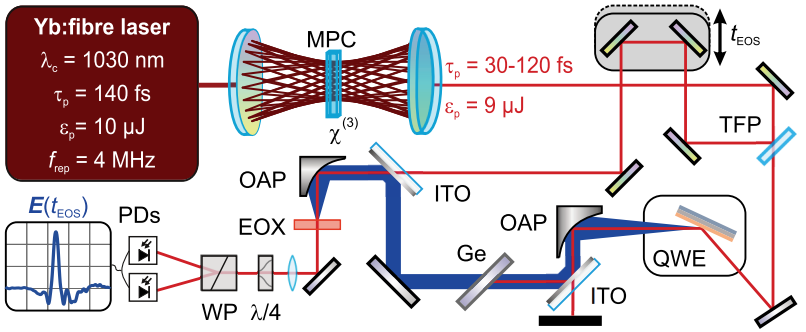

Figure 6.13 | Experimental setup for terahertz generation from quantum well emitters. Femtosecond near-infrared laser pulses of an ytterbium fibre laser (centre wavelength, $\lambda_c = 1030\,\mathrm{nm}$; pulse duration, $\tau_p = 140\,\mathrm{fs}$; pulse energy, $\varepsilon_p = 10\,\mu\mathrm{J}$; repetition rate $f_{rep} = 4\,\mathrm{MHz}$) are spectrally broadened and compressed in a multipass cell (MPC) via self-phase modulation in a fused silica $\chi^{(3)}$ medium. The pulses are used as both pump of the quantum well emitter and gate in the electro-optic sampling. EOX, electro-optic crystal; TFP, broadband thin-film polariser; τ_{EOS}, delay time; OAP, off-axis parabolic mirror; ITO, indium tin oxide coated fused silica window; Ge, germanium window; $\lambda/4$, quarter-wave plate; WP, Wollaston prism; PDs, balanced photodiodes.

the setup for the generation and phase-resolved detection of terahertz pulses from the novel quantum well emitters. The laser pulses from the ytterbium fibre laser are efficiently compressed as discussed in the previous paragraph, such that from the initial pulse energy of 10 µJ, 9 µJ can be used to pump the emitters. By shifting the nonlinear medium within the multipass cell (MPC) relative to the focal position, the pulse duration can be varied between 30 fs and 120 fs (see Appendix C.1). After compression, the near-infrared pulses are split by a broadband thin-film polariser (TFP). The weaker copy of the pulses acts as gate for electro-optic sampling, while the majority of the pulse energy is used for the terahertz generation.

As the dipole moment of the photoinduced electron–hole pairs in the quantum well emitter is directed parallel to the growth direction, so is the polarisation of the emerging terahertz radiation. In reflection geometry, the dipole radiation constructively interferes along the direction of the specular reflection of the near-infrared

pulses. To simultaneously maximise the outcoupling efficiency of the terahertz dipole radiation and minimise the reflection losses of the pump pulses, we choose an angle of incidence of 65°, close to Brewster's angle (Figure 6.14). The backside of the quantum well emitter is contacted to a water-cooled copper mount to reduce the thermal load induced by the absorbed optical power. An indium foil placed at the interface of the emitter and the mount improves the thermal contact. The generated terahertz pulses are collimated by an off-axis parabolic mirror (OAP) with a focal length of 203 mm. Subsequently, a fused silica window coated with indium tin oxide (ITO) reflects the terahertz pulses, while the near-infrared light is mostly transmitted. The residual pump light is absorbed in a germanium wafer with a thickness of 500 µm (Ge), placed at Brewster's angle for loss-free transmission of the terahertz radiation. A parabolic mirror with a focal length of 51 mm focuses the terahertz waveforms into the electro-optic crystal (EOX). Via an ITO window, the terahertz pulses are spatially overlapped with the gate pulses to electro-optically resolve the electric carrier field as a function of the delay time, t_{EOS}. The electro-optic detection is analogous to the setup discussed in Section 3.3. Here, we employ a gallium selenide crystal with a thickness of 6 µm as electro-optic crystal, which, in combination with the ultrashort gate pulses, supports detection of the true transient field without the detector response markedly distorting the waveform[178]. To suppress optical reflections inside the detector, which would render retrieval of the actual waveform difficult, the gallium selenide is mounted on an index-matched diamond substrate[178].

In the remainder of this chapter, the flexible high-repetition-rate generation and detection setup providing ultrashort pump and gate pulses will be used to test the novel quantum well emitters. Furthermore, a comparison of the quantum well emitters with a benchmark spintronic emitter will assess the usability for experimental techniques relying on intense sub-cycle terahertz waveforms, particularly lightwave-driven STM.

6.3.2 Scalable sub-half-cycle terahertz waveforms at high repetition rates

In the next step, the novel quantum well emitter scheme introduced above will be adapted to and optimised for the high-power near-infrared laser source presented

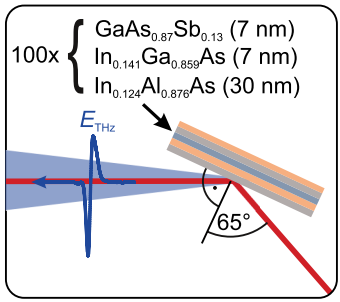

Figure 6.14 | Terahertz generation from quantum well emitters in reflection geometry. The quantum well emitter consisting of 100 $GaAs_{0.87}Sb_{0.13}/In_{0.141}Ga_{0.859}As$ quantum wells separated by $In_{0.124}Al_{0.876}As$ barriers is pumped in reflection geometry under an angle of incidence of 65°. The generated terahertz dipole radiation (E_{THz}) constructively interferes along the specular reflection of the pump beam.

in the previous section. To this end, in a collaboration with Prof. Dr. Dominique Bougeard, Dr. Dieter Schuh and Dr. Michael Prager, we engineer the material composition as well as the quantum well and barrier thickness of the epitaxial semiconductor heterostructures such that the pump pulses resonantly photoexcite exclusively *spatially separated* electron–hole pairs. Furthermore, to attain scalable emitters, all employed alloys must be lattice-matched to allow for strain-free epitaxial growth of multiple active layers.

Emitter design. An emitter design perfectly meeting these conditions is shown in Figure 6.15a: The confinement potential of the $GaAs_{0.87}Sb_{0.13}/In_{0.141}Ga_{0.859}As$ quantum wells separated by $In_{0.124}Al_{0.876}As$ barriers is depicted as grey area. While the thickness of the quantum wells amounts to 7 nm each, the $In_{0.124}Al_{0.876}As$ barriers measure 30 nm along the growth direction. The corresponding probability envelopes of electrons (e) and holes (h) in the first two subbands along the growth direction are represented by blue and red lines, respectively. Note, that in our samples, the highest-energy valence band is formed by heavy-hole states, which, for simplicity, will be called holes in the remainder of this thesis. A Schrödinger-Poisson solver was employed to calculate the quantum well potential, subband energies and probability distributions.

Notably, only the transitions from h1 and h2 to e1 can give rise to a significant shift current. Therefore, the heterostructure has been designed such that the transition energy from h1 to e1 matches the centre of the pump pulse spectrum of 1.2 eV. In contrast, the spatially direct interband transition h1 to e2 requires photoexcitation

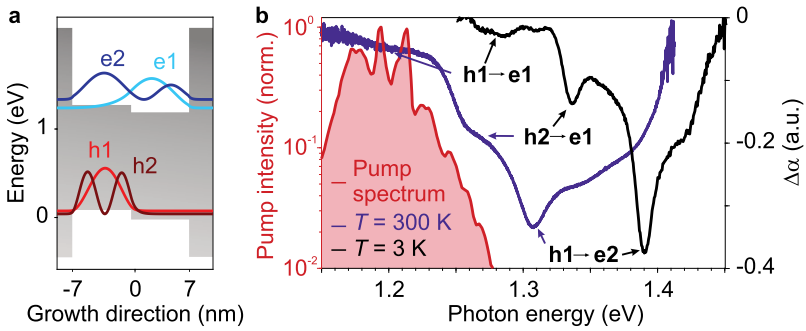

Figure 6.15 | Modulation spectroscopy of the quantum well emitter. a, Confinement potential of the quantum well structure (grey area) and probability densities of the two lowest (highest) electron (hole) subbands, e1 and e2 (h1 and h2), shown in blue (red). **b**, Pump-induced change of the absorption coefficient, $\Delta\alpha$, at room temperature (purple) and 3 K (black). At room temperature, the broadened pump spectrum (red) only overlaps with the spatially indirect transitions from h1 and h2 to e1.

with a photon energy of 1.3 eV. Thus, it cannot be driven by single-photon absorption of the pump. Moreover, as the constituents of the epitaxial heterostructure are lattice-matched, the emitters are grown in a strain-free manner (see Appendix D), allowing us to readily scale them by stacking multiple growth repetitions.

Modulation spectroscopy of the quantum well emitter. Modulation spectroscopy of the emitter structure allows one to experimentally verify the calculated band alignment. To this end, in a measurement performed by our collaboration partner Dr. Markus Stein at the Justus Liebig University Giessen, the heterostructure is pumped by femtosecond pulses with a photon energy of 1.46 eV at a fluence of 90 µJ cm^{-2}. A white-light continuum delayed with respect to the pump pulse is transmitted through the emitter, and the pump-induced change of the absorption, $\Delta\alpha$, is extracted. At room temperature, three dips emerge in $\Delta\alpha$ around 1.20 eV, 1.26 eV and 1.31 eV at a delay time of 1 ps (Figure 6.15b, purple line). The negative sign of $\Delta\alpha$ is a consequence of Pauli blocking leading to bleaching of strongly excited transitions. To unambiguously associate the broadened dips in $\Delta\alpha$ to the inter-

band transitions in the emitter, it is helpful to perform modulation spectroscopy at cryogenic temperatures. At a temperature of 3 K, the broadening of the transitions is drastically reduced and three clearly separated, distinct dips can be recognised at 1.28 eV, 1.34 eV and 1.39 eV (Figure 6.15b, black curve). Notably, a blueshift of 80 meV occurs for all transitions, which agrees with the temperature dependence of the bandgap of GaAs[209].

Analysing the amplitude of the dips, we obtain further insight on the transition matrix elements, and thus, on the spatial separation of the photoexcited electron–hole pairs: The transition at 1.31 eV at room temperature causes the largest pump-induced change, providing clear evidence that the latter corresponds to the excitation of spatially direct electron–hole pairs. In contrast, the relatively weak change in the absorption at 1.20 eV and 1.26 eV suggests spatially indirect transitions featuring a comparably small matrix element. This observation perfectly agrees with the calculated subband energies shown in Figure 6.15a. Consequently, every dip in $\Delta\alpha$ can unambiguously be assigned to an interband transition. At room temperature, the spatially indirect quantum leaps h1 to e1 at 1.20 eV and h2 to e1 at 1.26 eV overlap with the pump spectrum (Figure 6.15b, red area). Conversely, photoexcitation of the transition from h1 to e2 at 1.31 eV, which results in an insignificant shift current, will be negligible.

Hence, this configuration of $GaAs_{0.87}Sb_{0.13}$(7 nm)/$In_{0.141}Ga_{0.859}As$(7 nm) quantum wells is ideally suited for shift-current-based terahertz emission. The electrons and holes are separated by over 5 nm, which promises strong dipole moments in each active layer. In combination with the scalability of the emitter, emission of intense terahertz waveforms is expected.

Sub-half-cycle terahertz pulses. We now generate terahertz waveforms by photoexciting spatially indirect interband transitions in type-II aligned epitaxial heterostructures, for the first time. To this end, the emitter comprising 100 repetitions of $GaAs_{0.87}Sb_{0.13}$/$In_{0.141}Ga_{0.859}As$ quantum wells separated by $In_{0.124}Al_{0.876}As$ barriers is pumped under an angle of 65° (see Figure 6.14) with a pump fluence of 1 mJ cm^{-2}, at a repetition rate of 4 MHz. By varying the delay between the gate and the terahertz pulse, t_{EOS}, the electric-field waveform of the latter is stroboscopically sampled. Subsequently, we correct the electro-optic signal for the detector response

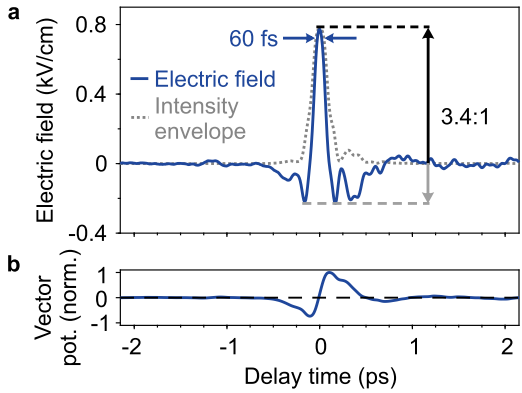

Figure 6.16 | Strongly asymmetric, intense terahertz transient from a quantum well emitter. a, Electric-field waveform (blue) detected by electro-optic sampling in a GaSe crystal with a thickness of 6 µm, corrected for the detector response. The positive field peak of 0.77 kV cm^{-1} exceeds the strongest negative excursion by a factor of 3.4. The width of the waveform at 90% of the maximum is as short as 60 fs. The FWHM duration of the intensity envelope (dotted grey line) is 183 fs. **b**, The vector potential of the waveform vanishes at large delay times.

to retrieve the actual waveform (see Appendix C.2 for details). The terahertz transient generated with a pump pulse duration of 75 fs (see Appendix C.1) follows a surprising waveform, shown in Figure 6.16a: An extremely sharp, single, positive field peak at $t_{\mathrm{EOS}} = 0$ ps, reaching a field strength of 0.77 kV cm^{-1} dominates two weak negative excursions at $t_{\mathrm{EOS}} = -0.16$ ps and $t_{\mathrm{EOS}} = 0.17$ ps exhibiting electric fields of 0.22 kV cm^{-1} and 0.23 kV cm^{-1}, respectively. When we compare the peak electric fields of each sign, we obtain an exceptional asymmetry ratio of 3.4:1. At first glance, it might not be readily apparent, whether the integral over this extraordinarily sub-cycle waveform vanishes, as required by Maxwell's equations for electromagnetic far-field waves propagating in free space[172]. This is equivalent to a vanishing vector potential at infinite positive and negative delay times, which actually is the case for the measured field transient (Figure 6.16b).

The electric field strength was calibrated in the following way: We assume that the terahertz focus describes a Gaussian TEM$_{00}$ profile, where the field strength at

a distance of $d_{e^{-1}}$ is lower by $1/e$ compared to the center of the mode. Then, the electric field waveform, E_{THz}, in the center of the mode fulfils

$$\int_{-\infty}^{\infty} E_{\mathrm{THz}}^2(t)\,\mathrm{d}t = \frac{2\varepsilon_{\mathrm{THz}}}{\varepsilon_0 c \pi d_{e^{-1}}}, \tag{6.6}$$

where ε_0 denotes the vacuum permittivity and c the speed of light. The terahertz pulse energy, $\varepsilon_{\mathrm{THz}} = 0.8\,\mathrm{pJ}$, was measured with a calibrated pyroelectric detector. By determining the portion of the terahertz power transmitted through a pinhole with well-known diameter, $d_{e^{-1}}$ was determined to be 500 µm, resulting in a terahertz peak field of $0.77\,\mathrm{kV\,cm^{-1}}$.

Notably, at its centre frequency of 2.47 THz the terahertz pulse features only 0.45 optical cycles within the FWHM of its intensity envelope of 183 fs (Figure 6.16a, grey dotted line, see Appendix C.3 for details). Such a sub-half-cycle waveform, which consists of one dominant positive field peak, only accompanied by feeble negative excursions, is the ideal transient bias for lightwave-driven STM. Furthermore, many lightwave-electronics applications, require ultrashort main maxima. Typically the temporal width, $\Delta\tau$, of the field crest at 90% of the peak field is used as figure of merit. In the context of lightwave-driven STM, $\Delta\tau$ is a good measure of the tunnelling time window, determining the temporal resolution of the experiment. For our pulses, this window is as short as $\Delta\tau = 60\,\mathrm{fs}$.

Octave-spanning multi-terahertz spectrum. A strongly sub-cycle waveform must be composed of Fourier components, which span multiple optical octaves and oscillate in phase. The ultrabroadband frequency spectrum of the terahertz transient obtained by Fourier transform is shown in Figure 6.17a. Its amplitude peaks at 1.34 THz, while the FWHM spans over 2.6 optical octaves from 0.68 THz to 4.3 THz. Note, that owing to the asymmetric shape of the spectrum, the centre frequency with respect to energetic weight of 2.47 THz (see Appendix C.3) is substantially higher than the frequency featuring the maximum amplitude. Containing Fourier components from 0.25 THz to 5.5 THz exhibiting amplitudes larger than 10% of the spectral peak, this spectrum covers a vast portion of the far-infrared window, making our multi-terahertz pulses a powerful probe for ultrabroadband spectroscopy.

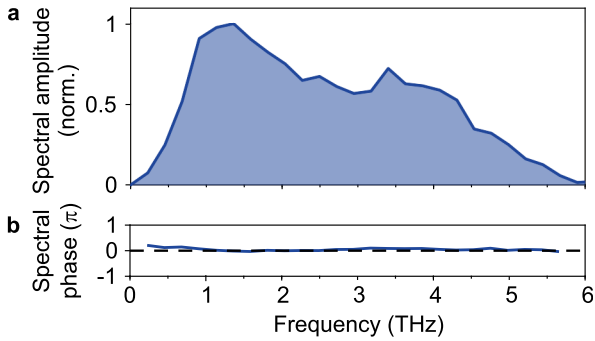

Figure 6.17 | Octave-spanning multi-terahertz spectrum. **a**, The spectral amplitude of the transient shown in Figure 6.16 spans over 2.6 optical octaves within its FWHM (0.68 to 4.3 THz) and includes Fourier components up to 6 THz. **b**, The spectral phase is flat in a range of frequencies featuring a spectral amplitude larger than 10% of the maximum, indicating a Fourier-limited pulse duration.

Furthermore, the spectral phase is flat over this frequency range, indicating that the pulse duration is Fourier-limited (Figure 6.17b).

Comparison with the simplistic model. The maximally asymmetric shape of the terahertz transients (Figure 6.16a) stands in stark contrast to the simplistic model introduced at the beginning of this chapter. There, for a static confinement potential, the emitted waveform was expected to comprise two equally strong oscillation half cycles (Figure 6.8b). Intriguingly, both the measured and the calculated transients showcase a similar, sub-cycle duration, while the main disparity lies in their carrier-envelope phase: The sine-like modelled waveform is shifted by $\pi/2$ with respect to the measured cosine-like transient. Thus, to ensure this discrepancy is inherently caused by the emission mechanism, artefacts induced by the geometrical Gouy phase[210], an intrinsic property of Gaussian beams, must be excluded. Close to its beam waist located at $z = 0$ along the propagation direction, a Gaussian beam undergoes a phase shift,

$$\phi_G(z) = \arctan \frac{z}{z_R}, \tag{6.7}$$

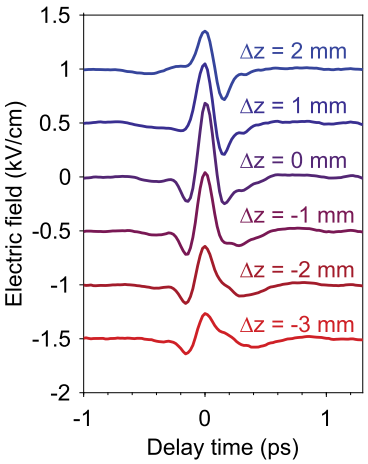

Figure 6.18 | Effect of the Gouy phase shift on the sub-cycle terahertz waveform. Terahertz waveforms detected with a gallium phosphide electro-optic crystal with a thickness of 250 µm, which was moved along the beam axis by a distance of Δz. Positive Δz denotes a larger distance between the crystal and the focusing mirror. The transients show a clear shift of the carrier-envelope phase, the so-called Gouy phase shift and are offset for clarity. The most asymmetric waveform at $\Delta z = 0$ is simultaneously the one with the highest intensity, indicating that it is detected in the focal plane.

where z_R is the Rayleigh length. As a consequence of Equation (6.7), the Gouy phase shift $\phi_G(z)$ from the beam waist to the far field ($|z| \gg z_R$) amounts to $\pi/2$. Since the quantum well emitter is placed in the beam waist of the pump pulses, the emitted terahertz transient must also be detected at its beam waist to retrieve the actual waveform.

To ensure that the detector is placed in the terahertz focus, waveforms were electro-optically detected for various positions of the detector crystal along the beam axis, relative to the focusing mirror, Δz (Figure 6.18). A clear, continuous shift of the carrier-envelope phase is observed as a function of Δz: The recorded waveform undergoes a transition from a symmetric, sine-like shape at $\Delta z = 2\,\text{mm}$ (blue) to the most asymmetric, cosine-like transient at $\Delta z = 0\,\text{mm}$ (purple). When the distance to the focusing mirror is further decreased, the transient becomes more symmetric again. Moreover, the field strength substantially depends on the position of the detector, allowing us to determine the focal position of the terahertz pulses, as the smallest beam diameter corresponds to the largest intensity. Using the integral over the square of the electro-optic signal as a relative measure of the intensity, we find that the most intense transient is simultaneous the most asymmetric one ($\Delta z = 0$), clearly indicating that our waveforms are detected in the terahertz focus.

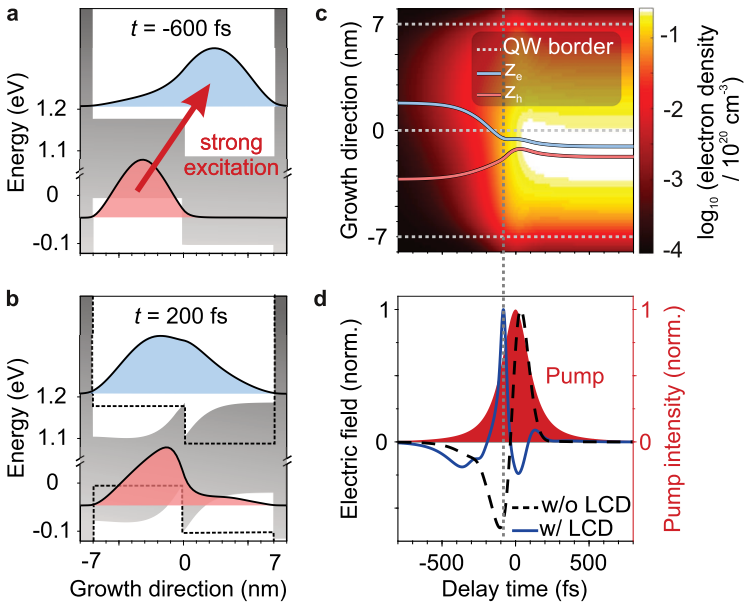

Figure 6.19 | Quantum mechanical calculation of the emission process. a, Computed quantum well confinement potential (grey area) as well as electron (blue) and hole (red) probability density $t = -600$ fs before the pump pulse. **b**, After strong optical excitation, local charging dynamics (LCD) drastically modifies both the confinement potential (grey area, static potential shown as dashed black line) and probability functions (blue, electrons, red, holes), shown $t = 200$ fs after the pump pulse. **c**, Color-coded plot of the electron density within one quantum well as a function of time along the growth direction. The quantum well interfaces are denoted by grey horizontal lines. The mean electron (hole) position is traced as blue (red) line, showing that the spatial separation between electrons and holes is lifted. The resulting quenching of the initial dipole moment results in **d**, emission of an almost unipolar terahertz waveform (blue). Without LCD, a symmetric transient (black dashed line) would be predicted. The intensity of the pump pulse with a FWHM duration of 130 fs is shown in red.

Revealing the microscopic emission process. Consequently, the maximally asymmetric shape of the terahertz transient must be inherent to the microscopic emission mechanism. To resolve the discrepancy with respect to the simplistically modelled waveform, a self-consistent, quantum mechanical model is utilised to simulate the terahertz emission[187]. Collaborating with Prof. Dr. Mackillo Kira and Qiannan Wen, we simultaneously solve the Maxwell's equations, the semiconductor Bloch equations and local charging dynamics[211,212]. In this way, they systematically describe the ultrafast optical excitation, many-body Coulomb interaction of photoexcited electron–hole pairs and the resulting shift currents. We find that intense photoexcitation results in many-body Coulomb correlations, which dynamically alter the quantum well potential as well as the subband energy levels and wavefunctions. Figure 6.19a,b compares the confinement potential (grey area) as well as the electron (blue) and hole (red) probability envelopes of the lowest subband before ($t = -600\,\mathrm{fs}$) and after ($t = 200\,\mathrm{fs}$) optical excitation by a pulse with a duration of 130 fs. The initial spatial separation of electrons and holes is lifted by Coulomb repulsion causing a redistribution of the electrons to the left side of the quantum well.

As a result, the dipole moment of the electron–hole pairs is quenched, drastically influencing the terahertz emission. This becomes clear in Figure 6.19c tracing the full temporal evolution of the total electron density (false-colour map) inside the quantum well, together with the centre of mass of the electron (blue) and hole (red) probability function. At negative delay times, t, with respect to the centre of the pump pulse (Figure 6.19d, red area), the photoexcited electrons and holes are separated by 5 nm, in perfect agreement with the simplified analysis of Figure 6.15a. As the pump intensity rises, the carrier density massively increases on the femtosecond timescale. Simultaneously, local charging dynamics pull the electrons and holes back together, resulting in an abrupt decrease of the electron–hole separation around $t = 0$.

This sudden quenching of the dipole moment generates a pronounced positive field peak (Figure 6.19d, blue line), as it is observed in the experiment. Calculating the emission neglecting local charging dynamics results in the same symmetric terahertz waveform as predicted by the simplistic model in Figure 6.8 (see Figure 6.19d, black dashed line). Hence, the measured asymmetric terahertz transients originate from a novel emission mechanism featuring an intriguing interplay of ultrashort shift currents and many-body Coulomb correlations.

Scalable pulses up to the mid-infrared. In contrast to heterostructures separated by finite tunnelling barriers[188], the novel emitter scheme does not rely on inherently bandwidth-limiting scattering processes to spatially separate photoexcited electrons and holes. Therefore, the terahertz pulses can be tailored by the pump pulse duration. We test this hypothesis experimentally, making use of our flexible pulse compression scheme, which allows us to gradually increase the bandwidth of the pump pulses. By moving the nonlinear medium relative to the focal position inside the multipass cell, we tune the full width at tenth of the maximum (FWTM) from 7.3 THz up to 22.3 THz (Figure 6.20b) and simultaneously reduce the duration of the pump pulses from 120 fs to 30 fs (see Appendix C.1). All spectra were obtained for a constant input pump pulse energy of 10 µJ, such that the pump fluence at the emitter remains fixed at 1 mJ cm^{-2}. Figure 6.20a shows the corresponding electro-optically detected terahertz waveforms after correction for the detector response (Appendix C.2). All transients maintain a strongly asymmetric shape. The ratio of strongest positive to negative field excursion increases from 2.8:1 (lowest, red waveform) for the narrowest pump spectrum to 3.7:1 (highest, blue transient) for the most broadband pump spectrum, even surpassing the asymmetry of the waveform shown in Figure 6.16a. This trend corroborates our microscopic model, where decreasing the pump pulse duration accelerates the dynamic quenching of the dipole moment, triggering the dominant positive oscillation half cycle of the terahertz waveform.

Moreover, when the duration of the pump pulses is decreased, the terahertz peak field monotonically increases from 0.5 kV cm^{-1} up to 1.1 kV cm^{-1}. Simultaneously, the width of the field crest, $\Delta\tau$, is compressed from 70 fs down to only 20 fs. This is a result of higher terahertz frequencies emerging at larger pump bandwidths. As shown in Figure 6.16c, although the terahertz spectra are marked by phonon absorption in the emitter around 8 THz, the highest terahertz Fourier component scales with the spectral width of the pump spectrum: Pump FWTMs of 7.3 THz, 13.2 THz, 17.4 THz, 18.8 THz, and 22.3 THz (Figure 6.20b) yield spectral terahertz components up to 5.0 THz, 11.2 THz, 12.2 THz, 17.9 THz, 21.4 THz (Figure 6.20c, black arrows), respectively. This correlation confirms that the terahertz bandwidth and pulse duration can be controlled via the pump pulse duration.

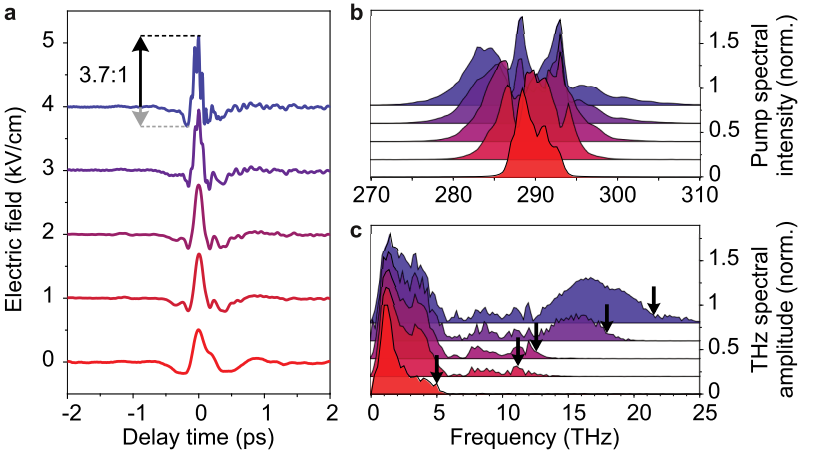

Figure 6.20 | Scalability of the terahertz bandwidth. **a**, Electro-optically detected terahertz waveforms (corrected for the detector response) for differenct pump pulse durations and spectra. **b**, Spectral intensity of the corresponding pump pulses. **c**, Terahertz spectral amplitudes of the respective waveforms shown in **a**. The largest Fourier component (10% of the maximum spectral amplitude) are indicated by black arrows. All waveforms and spectra are offset for clarity.

Scaling the terahertz field strength. Beyond the almost freely tunable bandwidth of our novel emission scheme, the terahertz field strength should be scalable as well. The strain-free epitaxial growth of the quantum wells facilitates stacking multiple active layers, decoupled by potential barriers (see Appendix D). This allows us to assess the scalability of the terahertz field amplitude by comparing emitters consisting of 20 and 100 quantum wells, respectively. At a pump pulse duration of 75 fs, the general shape of the transient remains unchanged, while the peak field is increased by a factor of 4.7, when the number of active layers is scaled from 20 to 100 (Figure 6.21a). Furthermore, the peak field scales linearly with the pump pulse energy (Figure 6.21b). Above a pump pulse energy of 7 µJ, first signs of saturation appear, which can be overcome by increasing the diameter of the pump beam, effectively reducing the pump fluence.

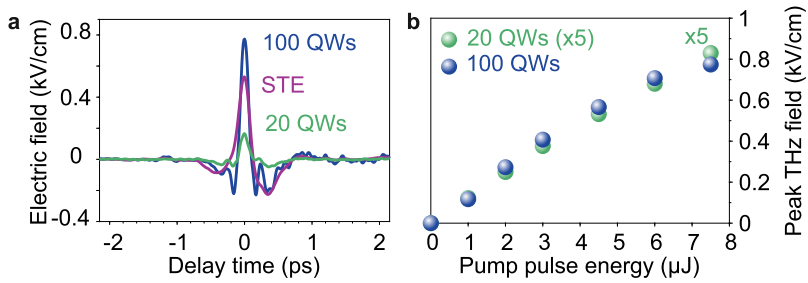

Figure 6.21 | Scaling the peak field. a, Increasing the number of growth repetitions from 20 (green) to 100 (blue) increases the electro-optically detected field strength by a factor of 4.7. The peak field of 0.77 kV cm^{-1} exceeds that generated from a spintronic terahertz emitter (purple). **b**, The peak field of both emitters with 20 (green, multiplied by a factor of 5 for better comparability) and 100 (blue) quantum wells scales linearly with the pump pulse energy. Only at very high intensities saturation sets in.

To benchmark the achieved field strength, we compare the generated terahertz waveform with that obtained from a commercially available spintronic emitter (*T-Spin1*, TeraSpinTec GmbH), composed of W(2 nm)/$Co_{40}Fe_{40}B_{20}$(1.8 nm)/Pt(2 nm)[184] (see Section 6.2, Figure 6.5c). This trilayer structure features two non-nomagnetic layers (W and Pt) with opposite sign of the respective spin Hall angle, θ_{SH}, which convert both the backward- and forward-flowing spin current from the centred ferromagnetic CoFeB layer to a unidirectional charge current[184]. In this way, the generated terahertz field is approximately doubled compared to the simple bilayer emitter introduced in Figure 6.5c.

Unprecedented optical pumping with an enormous average power of 30 W requires optimising the thermal transport inside the emitter. To this end, we cool the emitter to cryogenic temperatures with liquid nitrogen, increasing the thermal conductivity of the sapphire substrate by a factor of 30 compared to room termperature[213], while the terahertz emission is barely influenced[214]. When we photoexcite the spintronic emitter with the same pump pulses used for the quantum well emitters in transmission geometry, the waveform shown in Figure 6.21a (pink) is detected. The sub-cycle terahertz transient peaks at 0.53 kV cm^{-1}, exceeding the strongest negative excursion

by a factor of 2.3. The quantum well emitter comprising 100 quantum wells surpasses both the peak field (0.77 kV cm^{-1} vs. 0.53 kV cm^{-1}) and the asymmetry ratio (3.4:1 vs. 2.3:1) of the spintronic emitter, making it an attractive source for many applications, most importantly lightwave-driven STM.

6.3.3 Predicting and shaping the atom-scale near-field waveform

Confining light to extremely sub-wavelength scales substantially influences the time evolution of the electric carrier field[59–61,171,215–219]. Light-matter interaction in nanostructures sensitively depends on the coupling efficiency, plasmonic effects, near-field screening and geometrical phase shifts. Furthermore, fields confined to the *atomic* scale can be influenced by quantum dynamics such as tunnelling[220,221]. Thus, for experiments employing the carrier wave of tip-confined light pulses, it is indispensable to anticipate the confinement-induced changes to the waveform. This applies particularly to lightwave-driven STM, as its functionality poses strict, tightly defined requirements on the atomically confined terahertz waveform: only an asymmetric, sub-cycle field transient can drive a unidirectional tunnelling current via a well-defined resonance, once per laser pulse.

While electro-optic detection allows one to routinely resolve far-field electromagnetic waveforms, recording nanoscopic or even atomic fields has posed a serious challenge. In the last few years, enormous progress has been made in phase-resolved detection of terahertz waveforms in tip-sample junctions[60,149]. Moreover, even quantitative sampling of atom-scale near fields in a tunnel junction has been pioneered[61]. This breakthrough has facilitated to precisely determine the time evolution of the atom-scale voltage induced by the electric carrier wave, in a parameter-free manner.

Far-to-near-field transfer. By comparing a gauged near-field waveform with the corresponding far-field transient, one can directly deduce the far-to-near-field correlation. In the linear regime of electrodynamics, where all spectral components are independent, the far-to-near-field transfer is described by a complex-valued

transfer function, T_{NF}, in the frequency domain,

$$\tilde{E}_{\mathrm{NF}}(f) = \tilde{E}_{\mathrm{FF}}(f) \cdot T_{\mathrm{NF}}(f). \tag{6.8}$$

Here, $\tilde{E}_{\mathrm{NF}}$ and $\tilde{E}_{\mathrm{FF}}$ denote the complex-valued amplitude spectra of the near- and far-field waves, respectively. In Reference 61, Peller *et al.* extracted the transfer function of a lightwave-driven STM tip-sample junction both experimentally and theoretically by solving Maxwell's equations with the finite-element method. Intriguingly, despite the atomic nature of the investigated tunnel gap, the classical simulation accurately reproduces the experimental results. The lack of quantum mechanical effects on the near-field waveform is a consequence of single-electron tunnelling in lightwave-driven STM, since an individual electron does not alter its own potential.

The gauged field enhancement, that is the absolute value of the transfer function, $|T_{\mathrm{NF}}|$, increases steeply for lower frequencies, which is in good agreement with the typical f^{-1}-like response of nanoantennas[222]. At a frequency of 1 THz, the electric field is enhanced by a factor of 2×10^5 within the tunnelling junction. The order of magnitude of the field enhancement can be intuitively grasped relating the length scales, to which the light is confined: The terahertz far-field waveform is focused to a diameter comparable to its wavelength ($\sim 10^{-4}$ m), while the tunnel gap extends on the order of 10^{-9} m, effectively localising the electric fields by five orders of magnitude. Furthermore, the spectral phase in the tip-sample junction is shifted by approximately $-\pi/3$.

Modelling the atom-scale terahertz waveform. This knowledge of the far-to-near-field transfer allows us to predict the time evolution of the lightwave-driven bias, when terahertz pulses from the quantum well emitter are coupled into an atom-scale tunnel junction (Figure 6.22). We employ an analytical transfer function,

$$T_{\mathrm{NF}}(f) = \frac{2 \times 10^5 \cdot 1\,\mathrm{THz}}{f} \cdot \exp\left(-i\frac{\pi}{3}\right), \tag{6.9}$$

which reproduces the key characteristics of the discussed, experimentally calibrated transfer function[61] (Figure 6.22e). Applying our transfer function to the Fourier spectrum of the terahertz pulse generated in a quantum well emitter (Figure 6.22b),

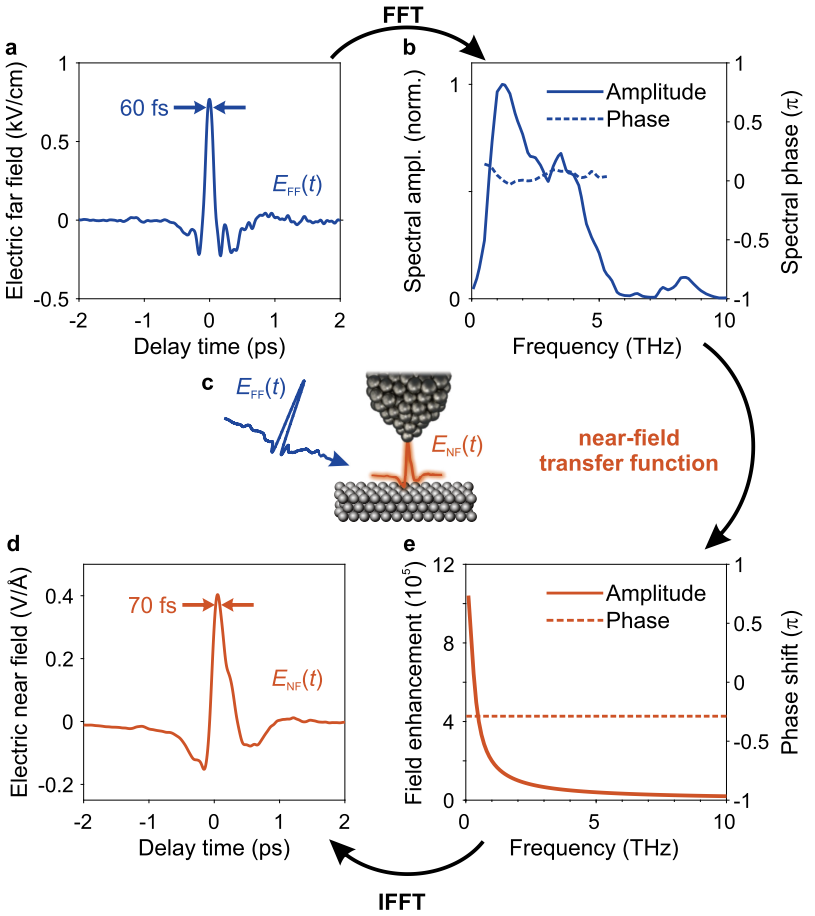

Figure 6.22 | Far-to-near-field transfer of terahertz waveforms. a, When a far-field terahertz field transient is coupled onto an STM tip, **b**, its spectral amplitude (solid line) and phase (dashed line) are strongly influenced by **c**, confinement to nanoscopic length scales. The far-to-near-field transfer can be described by **e**, a transfer function of the tip-sample junction, which typically shows a f^{-1} dependence in the spectral amplitude and induces a phase shift of about -π/3. **d**, The positive field peak of the obtained near-field waveform exceeds the strongest negative field excursion by a factor of 2.6 and the width of the field peak amounts to 70 fs.

we obtain the time evolution of the atom-scale near-field in the STM tunnel gap (Figure 6.22d). We find that the field enhancement promotes the expected field strengths to the atomically strong regime on the order of $1\,\mathrm{V\,Å^{-1}}$. Thus, for a typical tip-sample distance of 10 Å, a transient bias of multiple volts can be achieved, facilitating lightwave-driven tunnel currents through resonances of molecules and solid-state samples. Importantly, the near-field waveform maintains an asymmetric sub-cycle shape, where a dominating positive field peak with an electric field of $0.4\,\mathrm{V\,Å^{-1}}$ exceeds all negative field excursions by at least a factor of 2.6. Although the f^{-1}-field enhancement of the tip-sample junction suppresses the high-frequency components, the width of the field peak barely increases compared to the far-field waveform, such that a time window for tunnelling of $\Delta\tau = 70\,\mathrm{fs}$ can be expected.

Shaping the near-field waveform. A well-known far-to-near-field transfer allows us not only to anticipate the near-field time evolution for a given far-field transient, but to precondition it to achieve a desired near-field waveform. While lightwave-driven STM using the laser pulse as transient bias demands a maximally asymmetric lightwave-driven bias, for schemes exploiting femtosecond atomic forces[59] the atom-scale electric field exerting the force could be tailored at will. Here, I will demonstrate how terahertz pulses from our novel quantum well emitters can be readily pre-shaped to counteract the dispersion of the far-to-near-field transfer. We deliberately disperse the extremely asymmetric far-field transient by transmission through a GaAs wafer with a thickness of 500 µm, placed at an angle of incidence of 60° to reduce the reflection losses. Note, that since the emitter itself predominantly consists of GaAs alloys, additional phonon absorption is negligible. As a result of the dispersion of GaAs, the transmitted far-field waveform, which was detected with a GaP detector (thickness, 250 µm), exhibits a symmetric shape (Figure 6.23a). The transient features trailing oscillations, which are attributed to strongly dispersed Fourier components close to the frequency of transverse optical phonons in GaAs.

Applying the transfer function given in Equation (6.9) according to Equation (6.8), results in the near-field waveform depicted in Figure 6.23b. In contrast to the symmetric far field, it has a maximally asymmetric shape, where the positive peak of $0.37\,\mathrm{V\,Å^{-1}}$ exceeds both negative extrema featuring electric fields of $0.11\,\mathrm{V\,Å^{-1}}$, each, by a factor of 3.5. Furthermore, the high-frequency trailing oscillations are

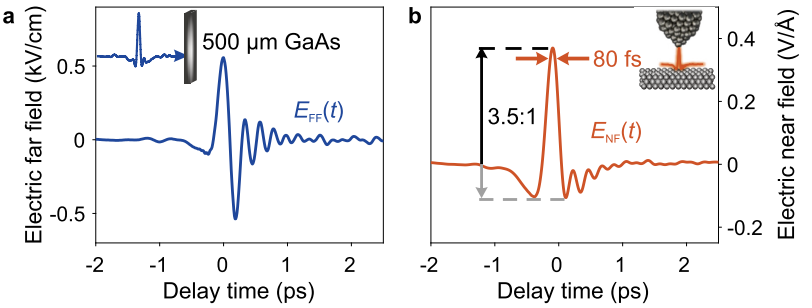

Figure 6.23 | Shaping the near-field waveform. **a**, The far-field waveform generated in the novel quantum well emitter is deliberately dispersed in a GaAs wafer with a thickness of 500 µm (inset). The transmitted transient, E_{FF}, detected with a GaP detector (thickness, 250 µm) exhibits a symmetric shape. **b**, The corresponding near-field waveform, E_{NF}, is maximally asymmetric, featuring an asymmetry ratio of 3.5:1. The width of the field peak amounts to 80 fs.

strongly suppressed as a consequence of the f^{-1}-field enhancement. The width of the field crest, $\Delta\tau = 80$ fs is only slightly increased compared to the undispersed near-field waveform, which has a respective width of 70 fs (Figure 6.22d). This result clearly demonstrates that we are able to precondition the far-field carrier wave in an almost loss-free manner, such that the initial, remarkably asymmetric far-field waveform is maintained in the near field of the tip-sample junction.

Outlook: Towards gapless multi-terahertz spectra. In this chapter, I presented a novel, scalable terahertz emitter concept based on spatially indirect interband transitions. Electronic wavefunctions in type-II aligned heterostructures are tailored, such that intense, resonant interband photoexcitation by a high-power femtosecond laser launches ultrafast shift currents, which are quenched by many-body Coulomb correlations. In this way, extremely asymmetric, sub-half-cycle terahertz waveforms are generated at a high repetition rate of 4 MHz. Exploiting the scalability of the scheme, we achieve peak fields exceeding 1.1 kV cm^{-1} and octave-spanning spectra covering frequencies from 0.2 THz to 21.4 THz. Owing to the versatility of our approach, we envision that it may be adapted for many more applications including

nonlinear light-matter interaction as well as ultrabroadband far-field and near-field spectroscopy.

Importantly, the concept of terahertz generation from spatially indirect interband transitions is yet far from being fully exhausted. As the timescale in which the shift currents are quenched by ultrafast screening has not yet been reached by the utilised pump source, excitation pulses shorter than 30 fs are expected to give rise to even more broadband and more asymmetric waveforms. Furthermore, the in- and outcoupling efficiency of the terahertz pulses can be substantially increased by index-matched prisms, enabling much higher field strengths. Lastly, transferring the emitter scheme to non-polar materials such as silicon or germanium may even pave the way to generation of gapless spectra spanning the entire terahertz and mid-infrared spectral range.

Outlook: Towards femtosecond videography of individual spins. The novel terahertz emitter concept introduced in this chapter paves the way for the next generation of lightwave-driven microscopy. The single positive field excursion dominating the generated terahertz transients is perfectly suited to drive unipolar, state-selective tunnelling currents in an atom-scale tip-sample junction in a time window as short as 70 fs, thereby enhancing the temporal resolution of the scheme compared to previous pioneering studies[58,59,61]. Moreover, the extremely sub-cycle waveform lacking considerable leading or trailing oscillations allows one to conclusively evaluate pump-probe experiments directly after excitation. Finally, the high repetition rate of our source of 4 MHz enables large lightwave-driven currents, guaranteeing high signal-to-noise ratios.

Lightwave-driven STM is ideally suited to explore ultrafast spin phenomena in atomically thin systems. Spin-resolved lightwave-driven STM would provide an unmatched toolkit for the investigation of quantum phenomena in condensed matter and individual molecules by combining femtosecond temporal and atom-scale spatial resolution with control over single spins. In the pursuit of this ambitious goal, we collaborate with with the group of Prof. Dr. Jascha Repp to merge the flexible ultrafast laser sources presented in this thesis, that is, the quantum well terahertz emitters and the high-repetition-rate noncollinear optical parametric amplifier, with a new scanning tunnelling microscope. This state-of-the-art, ultra-high vacuum microscope,

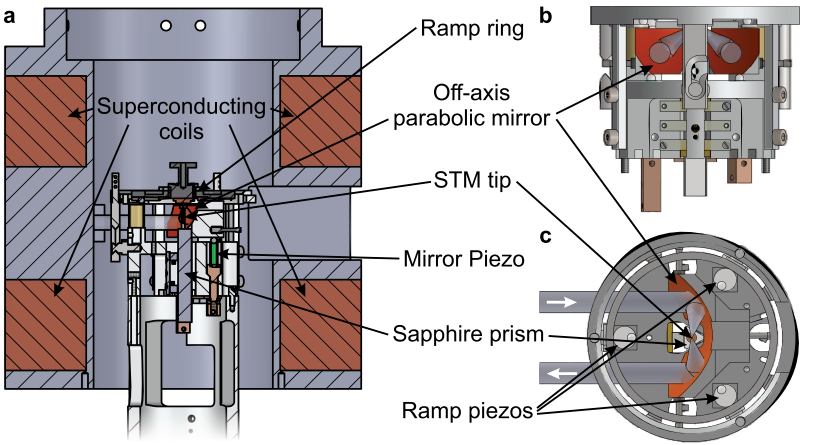

Figure 6.24 | Scan head design of the new spin-resolved lightwave-driven scanning tunnelling microscope. a, Side view of the scan head design including the superconducting coils (brown), which can generate strong out-of-plane magnetic fields. **b**, Front and **c**, top view of the scan head design. Courtesy of Prof. Dr. Jascha Repp and Christoph Rohrer.

which has been developed by Prof. Dr. Jascha Repp's group, is nearing completion, as of February 2024. The integration of superconducting coils (Figure 6.24a) facilitates tunable spin polarisation of the sample with magnetic fields up to 3 T. Moreover, the scan head has been fundamentally redesigned and optimised for operation with an external laser source (Figure 6.24). The ramp ring enables complete three-dimensional freedom of motion of the sample, while the tip position can remain fixed, eliminating the need for frequent realignment of the laser, therewith greatly increasing the available measurement time. Importantly, the new design allows one to collect and couple out radiation, which is scattered or even emitted from the tip-sample junction, opening the door to ultrafast multi-messenger nanoscopy. We anticipate that this optimised, spin-resolved lightwave-driven scanning microscope will allow us to record the first-ever real-space, *atom-scale* movies of the femtosecond dynamics of *individual* spins. Consequently, this unique experimental toolset has the potential to profoundly advance our understanding of strongly correlated magnetic systems.

Chapter 7

Conclusion and outlook: Towards spin-resolved atom-scale videography

In this thesis, I presented, how we revealed the femtosecond dynamics of excitons in atomically thin crystals of the magnetic quantum material CrSBr. A unique experimental technique was implemented, which combines sub-cycle terahertz polarisation nanoscopy with tunable optical pump pulses, allowing us to selectively photoexcite and probe unbound electron–hole pairs and excitons. Our study marks the first terahertz investigation of quasi-one-dimensional excitons in monolayer materials and the first observation of femtosecond excitonic dynamics in a two-dimensional paramagnet. Moreover, we unveiled a novel, scalable terahertz emission mechanism based on the intricate interplay of ultrafast shift currents and femtosecond screening in semiconductor heterostructures[187]. We generate intense and extremely asymmetric phase-stable field waveforms, which are powerful tools for lightwave control of charge carriers. In particular, the sub-half-cycle terahertz pulses are the perfect femtosecond bias for lightwave-driven scanning tunnelling microscopy, which may advance sub-cycle nanoscopy of van der Waals magnets to the atomic scale.

Tracing femtosecond electron–hole pair dynamics in an atomically thin paramagnet. A new flexible experimental setup has been designed and built for ultrafast scattering-type near-field spectroscopy of quasi-one-dimensional electron–hole pairs in the strongly correlated van der Waals crystal CrSBr. A high-power

ytterbium fibre laser generates phase-locked terahertz probe pulses featuring spectral components up to 3 THz, which are coupled to the tip apex of a near-field microscope. This allows us to overcome the diffraction limit and investigate CrSBr monolayers, whose lateral dimensions are much smaller than the terahertz probe wavelength. A home-built noncollinear optical parametric amplifier provides femtosecond optical pump pulses, whose photon energy is widely tunable from 1.3 eV to 2.4 eV, enabling selective photoexcitation of excitons and continuum states. The high repetition rate of 4 MHz makes this flexible laser source compatible with scattering-type near-field microscopy. Field-resolved detection of the scattered terahertz waveforms enables us to explore the nanoscale dielectric response of the sample and, in particular, the polarisability of photoexcited electron–hole pairs, providing valuable information on their binding state. By analysing the pump-induced polarisation signal, we directly trace the femtosecond dynamics of photoexcited electron–hole pairs in CrSBr bulk and monolayer crystals. We observe an ultrashort exciton lifetime of 500 fs in atomically thin CrSBr, which is 30 times shorter than the lifetime determined in the bulk. In bulk crystals, two distinct decay dynamics suggest scattering of excitons with phonons or paramagnons. Performing terahertz near-field spectroscopy, we reveal the hallmark dielectric signatures of unbound electron–hole pairs and excitons in the bulk. These findings allow us to link a fast decay of the polarisation signal with a decay time of ~ 1 ps to the binding of continuum states into 1s excitons. By extracting the nonequilibrium dielectric function of monolayer CrSBr in a model-free manner, we observe the spectral characteristics of internal transitions between excitonic states with high principal quantum numbers. Our experiments showcase how combining ultrafast near-field microscopy with tunable photoexcitation can unveil the spectral fingerprints and femtosecond dynamics of exotic quasiparticles in microscopic quantum materials.

Outlook: Resolving magnetic phase transitions on the nanoscale. We envision that our approach may elucidate the dynamics of complex excitonic correlations with the lattice and various magnetic phases of CrSBr. For complementary near-field experiments, multi-terahertz pulses are of particular interest, as they can couple to infrared-active phonons in CrSBr and directly probe the internal structure of excitons[14,36]. Ultimately, our experimental method could facilitate imaging of magnetic

domains during phase transitions with femtosecond temporal and nanometre spatial resolution. Moreover, polarisation nanoscopy poses an ideal probe for moiré-stacked van der Waals magnets, which have attracted tremendous attention[223–225], as they open a new frontier in research of two-dimensional magnetism, offering exciting new pathways for novel spintronic and optoelectronic devices.

A new scalable approach for emission of asymmetric terahertz waveforms. Pushing towards exploring the femtosecond dynamics of strongly correlated magnetic systems on the *atomic* scale, we are collaborating with the group of Prof. Dr. Jascha Repp to realise *spin-resolved* lightwave-driven scanning tunnelling microscopy. As an optimised ultrafast laser source for the new microscope conceived by Prof. Dr. Jascha Repp's group, we have developed a novel scheme for the generation of intense phase-locked multi-terahertz pulses. In collaboration with the research group of Prof. Dr. Dominique Bougeard, we engineered electronic wavefunctions in type-II-aligned epitaxial semiconductor heterostructures such that resonant interband photoexcitation results in ultrafast charge separation over several nanometres without any external bias. To thoroughly assess the new emitter concept, we developed and built a flexible experimental setup, which provides ultrashort near-infrared excitation pulses with tunable pulse durations at a high repetition rate of 4 MHz. Exploiting a highly efficient and robust pulse compression scheme based on nonlinear spectral broadening in a bulk medium inside a multipass cell, the laser pulses from a high-power ytterbium fibre laser are compressed to durations adjustable from 120 fs down to 30 fs. Our emitter consisting of 100 $GaAs_{0.87}Sb_{0.13}/In_{0.141}Ga_{0.859}As$ quantum wells separated by $In_{0.124}Al_{0.876}As$ barriers generates extraordinary terahertz waveforms, which we resolve with ultrabroadband electro-optic detection: The transients encompass only 0.45 optical cycles within the full width at half maximum of their intensity envelope and are extremely asymmetric. Tuning the pump pulse spectrum and duration, we achieve a terahertz field peak of 1.1 $kV\,cm^{-1}$, which exceeds the feeble negative excursions by a factor of 3.7.

A quantum mechanical simulation of the emission process by Prof. Dr. Mackillo Kira and Qiannan Wen reveals a qualitatively new microscopic generation mechanism. Upon strong optical excitation of the quantum-confined system, dominant many-body Coulomb correlations of photoexcited electron–hole pairs dynamically shift

the confinement potential, lifting the spatial separation of electrons and holes. The abrupt quenching of the initial dipole moment gives rise to the observed, asymmetric terahertz waveform. Exploiting these ultrafast dynamics, we tune the terahertz spectral bandwidth with the pump pulse duration and generate multi-octave spanning spectra with frequency components beyond 20 THz. In addition, the terahertz field strength is scalable thanks to the strain-free epitaxial emitter growth. Our flexible emission scheme represents a valuable complement to the existing toolset for terahertz generation. In particular, the compatibility with high-power lasers and the almost unipolar shape of the electric-field waveform position the quantum well emitter as an outstanding source for lightwave-control in condensed matter[162].

Outlook: Ultrafast dynamics of individual spins on the atomic scale. Our novel source of intense sub-cycle terahertz waveforms will soon be combined with a new ultra-high vacuum scanning tunnelling microscope developed by the group of Prof. Dr. Jascha Repp. The intense and extremely sub-cycle field transients we generate are perfectly suited to drive state-selective tunnelling currents across the Angstrom-scale tip-sample junction in time windows as short as 70 fs. As superconducting magnetic coils built into the new microscope facilitate control over the magnetic order of the sample, this next-generation lightwave-driven scanning tunnelling microscope represents an important addition to pioneering techniques, in which precession of single spins has been observed[226] and even manipulated[227] with Angstrom spatial resolution. Our new experimental setup could enable simultaneous state-selective, atom-scale and, importantly, *femtosecond* control over individual spins, for the first time. We anticipate that spin-resolved lightwave-driven scanning tunnelling microscopy will shed light on molecular spintronics[228] and dynamics of atom-scale spin-orbit coupling[229,230] in the time domain. Additionally, one may even resolve ultrafast spin switching[40] and relaxation, one spin at a time. Ultimately, studying femtosecond spin-polarised currents in the quasi-one-dimensional magnet CrSBr on the atomic scale could provide new insights into the exotic quantum phases in Tomonaga-Luttinger liquids, where spin–charge separation can split the quantum degrees of freedom of an electron into three quasiparticles called holon, spinon and orbiton[231,232].

Appendix A

Improving the stability of the experimental setup

Active stabilisation of the beam pointing. The experiments presented in this thesis require remarkable stability of the experimental setup. One of the most important factors limiting the latter is beam jitter. Environmental vibrations, atmospheric turbulence and thermal instabilities can affect the beam pointing. Especially the employed high-power fibre laser used in this work is a potential source of drift. Thus, in addition to a setup built as compact and passively stable as possible, an active beam pointing stabilisation is required to reduce noise and enable long-term measurements.

A sketch of the stabilisation scheme employed in this work is shown in Figure A.1. The output of the pump laser is guided via two motorised mirrors that are placed in front of the experimental setup, where the beam pointing is desired to be as stable as possible. The motorised mirrors are steered by a closed-loop controller that uses the signal of two four-quadrant photodiodes to detect and compensate for the positional and angular deviation of the laser beam. For maximal sensitivity, the first diode is placed closely after the second motorised mirror, whereas the second diode is positioned as far away as possible.

The beam pointing deviation with and without active stabilisation, recorded with a scanning slit beam profiler placed 1 m behind the laser output, is shown in Figure A.2. When the closed-loop controller is turned off, right after a cold start of the laser,

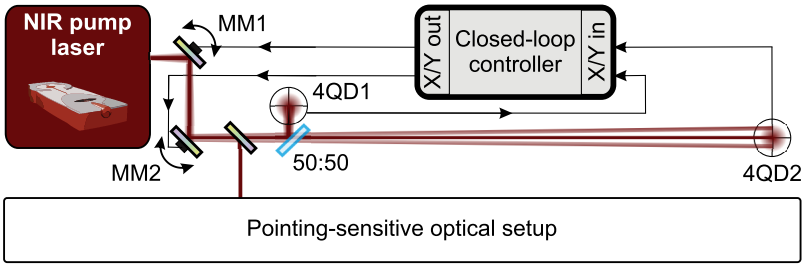

Figure A.1 | Setup of the active beam pointing stabilisation. The output of the pump laser used in this work is subject to pointing deviations (blurred lines). These are detected by two four-quadrant photodiodes (4QD1, 4QD2), placed behind a mirror (reflectivity < 1) steering the beam to the experimental setup. The horizontal and vertical pointing deviation are then read out in a fast, closed-loop controller actuating two motorised mirrors (MM1, MM2) to compensate for the deviation, such that the beam pointing is stable in the experimental setup.

both the horizontal (red circles) and vertical (dark red diamonds) pointing drift substantially by 80 µm and 180 µm, respectively, before reaching a steady position after 30 min (see Figure A.2a). With the active beam stabilisation enabled, this initial drift is almost completely compensated for both axes (light blue circles and dark blue diamonds) and the equilibrium position is achieved directly after the cold start.

Furthermore, the long-term stability shown in Figure A.2b is drastically improved by the beam stabilisation scheme. For disabled stabilisation, the vertical position oscillates with an amplitude of over 10 µm and a period of around 1.2 hours. Simultaneously, the laser beam exhibits a long-term drift in the horizontal axis, that did not stop after eleven hours. These deviations are absent when the active stabilisation is turned on, resulting in a very steady beam pointing, exhibiting a root-mean-square deviation of only 1.6 µm in both directions. Owing to this remarkable long-term stability, we were able to perform the highly sensitive measurements presented in this work.

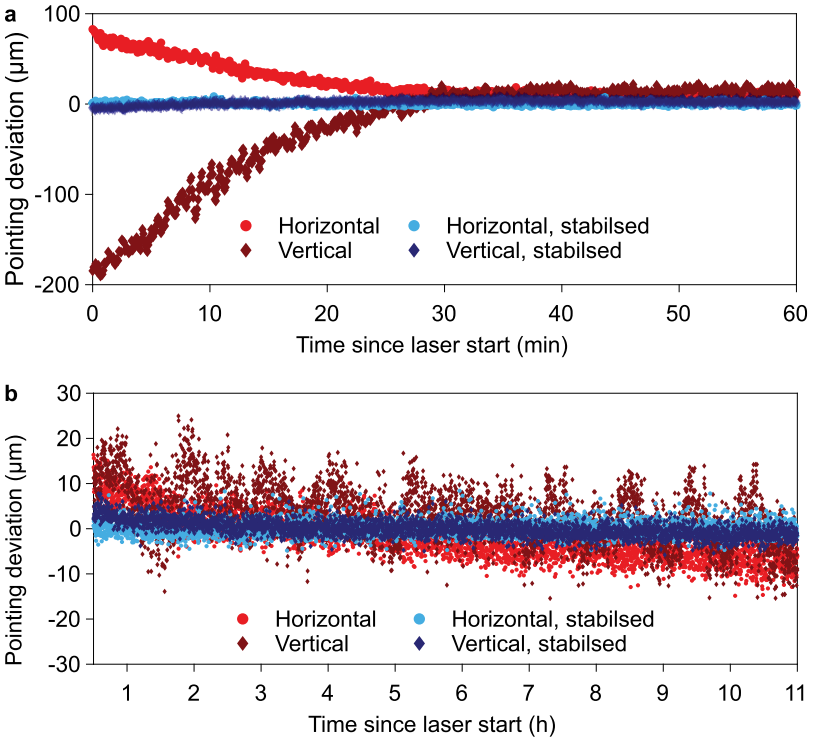

Figure A.2 | Beam pointing stability of the near-infrared pump laser. a, Beam pointing deviation directly after a cold start of the laser, detected 1 m behind the laser output. Without active stabilisation, both the vertical and the horizontal beam pointing of the laser (light and dark red points) drift significantly during the first 30 minutes, whereas when actively stabilised (light and dark blue points), the beam pointing does not drift. **b**, Long-term pointing stability. Even after thermalisation of the laser amplifier, the beam position oscillates vertically with a period of around 1.2 hours. In the horizontal direction the pointing undergoes a small but steady, long-term drift. When the active beam stabilisation is turned on, the beam pointing is stable, exhibiting a root-mean-square deviation of only 1.6 µm in both directions.

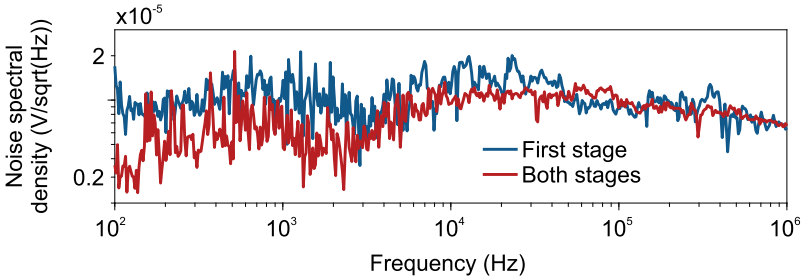

Figure A.3 | Reducing excess noise in a two-stage NOPA by pump depletion. Noise spectral density of the signal pulses (centre wavelength, 650 nm) amplified in one stage (blue) and both stages of the NOPA (red).

Reducing excess noise by pump depletion. The NOPA presented in Chapter 4 makes use of cascaded nonlinear optical effects such as second harmonic generation ($\chi^{(2)}$), supercontinuum generation ($\chi^{(3)}$) and optical parametric amplification ($\chi^{(2)}$), which amplify the excess noise of the laser driving the NOPA. To reduce the most important source of technical noise, that is, the delicate supercontinuum generation, the second stage of the NOPA is driven into pump depletion. Figure A.3 depicts the noise spectral density spectra of the signal pulses centred at a wavelength of 650 nm, amplified in the first stage (blue) and in both NOPA stages (red). The noise spectrum was recorded with a lock-in amplifier (Zurich Instruments, HF2LI) and a silicon photodiode, keeping a constant incident optical power resulting in a voltage drop of 100 mV. Particularly at frequencies below 3 kHz, the pulses, which were amplified in both stages and were subject to pump depletion, the excess noise is substantially reduced.

Appendix B

Details on the modelling of CrSBr

B.1 Modelling the near-field response of bulk CrSBr

Estimating the near-field probing sensitivity. In Chapter 5, a spatial weighting factor, $\xi(\boldsymbol{r})$, is introduced to account for the probing sensitivity in the near field of the tip apex, which is mainly determined by the field distribution of the tip apex. To simplify the spatial distribution of the probing sensitivity to a one-dimensional problem, in Chapter 5, we approximate $\xi(\boldsymbol{r})$ by separating it into in- and out-of-plane components, $\xi(\boldsymbol{r}) = \xi_{x,y}(x,y)\,\xi_z(z)$. As the sample is probed by *evanescent* near fields at the tip apex, which decay exponentially[108,233], one can approximate $\xi(\boldsymbol{r})$ as a product of Gaussians determined by the shape of the tip apex and the tapping amplitude, along the in-plane direction, and an exponential decay along the out-of-plane direction,

$$\xi(\boldsymbol{r}) = \xi_{x,y}(x,y)\,\xi_z(z) \propto \exp\left[-\left(\frac{x}{\sigma_x}\right)^2 - \left(\frac{y}{\sigma_y}\right)^2\right] \cdot \exp\left(-\frac{z}{\kappa_z}\right). \tag{B.1}$$

Here, σ_x and σ_y determine the in-plane width of $\xi(\boldsymbol{r})$, which mainly depends on the radius of curvature of the tip apex and κ_z is the decay constant along z, which depends on the dielectric screening in the sample and the tapping amplitude of the

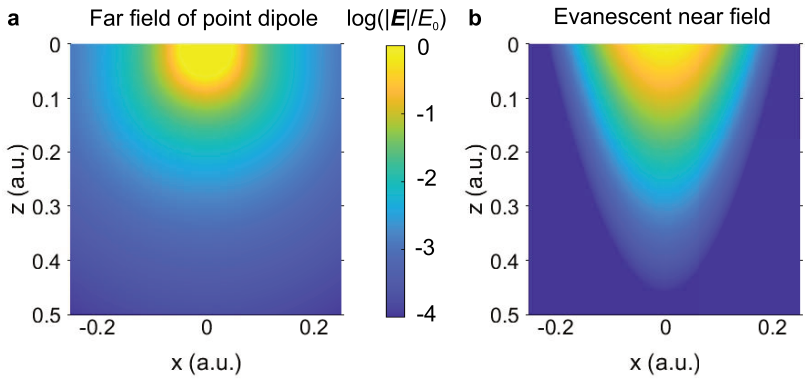

Figure B.1 | Comparison of a radial far-field and an evanescent field distribution. **a**, Logarithmic false-colour plot of the far-field distribution, $|\boldsymbol{E}|$, of a point dipole located at the coordinate origin. **b**, Logarithmic false-colour plot an exemplary field distribution of an evanescent near field beneath a tip apex, composed of a product of in-plane (xy-plane) Gaussians and an out-of-plane (z) exponential decay.

tip. Figure B.1 compares such an exemplary near-field distribution to the far-field distribution of a point dipole.

The pump-induced change with the finite-dipole model. In Section B.1, we model the frequency-dependent complex-valued scattering amplitude, $\tilde{E}$ and pump-induced change $\Delta\tilde{E} = (\tilde{E}_{\text{pumped}} - \tilde{E}_{\text{unpumped}})$ with the finite-dipole model[113] In the calculations, we use the experimental tapping amplitude (150 nm) and radius of curvature of the tip apex (20 nm) as well as a tip spheroid length, $2L = 720$ nm and an empirical geometry factor, $g = 0.7e^{0.06i}$, as described in previous studies using the finite-dipole model in the terahertz frequency range[114,115]. The sample is modelled as a layered system, where the CrSBr flake (thickness, 400 nm) is located on SiO_2 (thickness, 285 nm). The dielectric function of the CrSBr sample, ε, is parametrised

Drude	$h\nu_\mathrm{p} = 1.81\,\mathrm{eV}$, $t_\mathrm{p} = 0.5\,\mathrm{ps}$	Lorentz	$h\nu_\mathrm{p} = 1.81\,\mathrm{eV}$, $t_\mathrm{p} = 2.5\,\mathrm{ps}$	$h\nu_\mathrm{p} = 1.39\,\mathrm{eV}$, $t_\mathrm{p} = 0.5\,\mathrm{ps}$
$\frac{\omega_\mathrm{plasma}}{2\pi}$ (THz)	18	$\frac{\omega_{\mathrm{res},1}}{2\pi}$ (THz)	1	1
τ_sc (fs)	85	f_1	20	35
		β_1 (THz)	20	20
		$\frac{\omega_{\mathrm{res},2}}{2\pi}$ (THz)	14	14
		f_2	150	350
		β_2 (THz)	30	30

Table B.1: Parameters of the dielectric functions used to reproduce the spectral near-field responses in bulk CrSBr.

as either a Drude response,

$$\varepsilon(\omega) = \varepsilon_\mathrm{eq} - \frac{\omega_\mathrm{plasma}^2}{\omega^2 + i\frac{\omega}{\tau_\mathrm{sc}}} \tag{B.2}$$

with a constant equilibrium dielectric function, $\varepsilon_\mathrm{eq} = 10$ (Reference 34), the plasma frequency $\omega_\mathrm{plasma} = \sqrt{\frac{ne^2}{m^*\varepsilon_0}}$, Drude scattering time, τ_sc, charge-carrier density, n, elementary charge, e, effective mass, m^* and vacuum permittivity, ε_0, or two Lorentz oscillators,

$$\varepsilon(\omega) = \varepsilon_\mathrm{eq} + \sum_k \frac{f_k\omega_{\mathrm{res},k}^2}{\omega_{\mathrm{res},k}^2 - \omega^2 - i\beta_k\omega}, \tag{B.3}$$

with resonant angular frequency, $\omega_{\mathrm{res},k}^2$, damping coefficient, β_k and oscillator strength, f_k, for each oscillator k. The parameters used to fit the pump-induced near-field response of bulk CrSBr are listed in table B.1. The calculated relative amplitude spectrum obtained for the Drude response is rescaled by a factor 0.11 to obtain optimal agreement with the experimental data.

B.2 Modelling the nonequilibrium dielectric function of monolayer CrSBr

The modified, anisotropic Rytova-Keldysh potential described in Section 5.4 (Equation (5.10)) is shown in Figure B.2a alongside the eigenenergies of the obtained

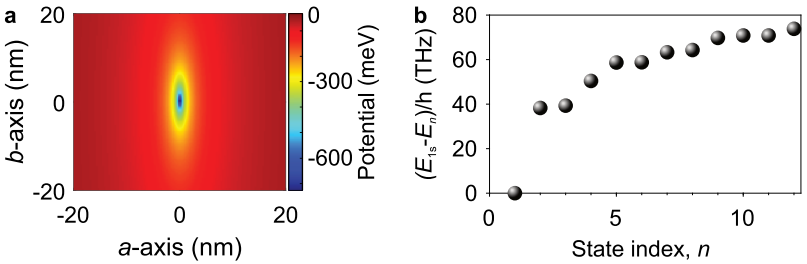

Figure B.2 | Anisotropic Rytova-Keldysh potential and eigenenergies of exciton states in monolayer CrSBr. a, Rytova-Keldysh potential for strongly anisotropic reduced effective masses. **b**, Calculated eigenenergies of the first exciton states with respect to the 1s ground state.

exciton states with respect to the 1s ground state (Figure B.2b). The spectral shape of the pump-induced change of the dielectric function was modelled as follows: By solving the two-dimensional Schrödinger equation the first 30 eigenstates of the Rytova-Keldysh potential were retrieved (Figure B.3). For each pair of eigenstates, the transition dipole matrix element for light polarised along the *b*-axis is calculated. The matrix elements are multiplied with the thermal population of the exciton states at a thermal energy, $k_\mathrm{B}T = 40\,\mathrm{meV}$ and the product is used as the oscillator strength of Lorentz lines, which are centred at the respective transition energies (Figure B.2b). We assume a width of 20 meV for every line. The pump-induced change of the dielectric function is obtained by summation of the Lorentz oscillators and used in the finite-dipole model and scaled by a constant real factor to match the experimental data.

Equilibrium dielectric function of monolayer CrSBr. The only required assumption to extract the dielectric function of a photoexcited CrSBr monolayer by inverting the finite-dipole model is its equilibrium dielectric function, ε_eq. The spectral shape of ε_eq can be retrieved by analysing distinct signal harmonics, $\tilde{E}_\mathrm{n}$ of the scattered field transient, demodulated at the n-th harmonic of the tip oscillation frequency[116]. By, for example, dividing the third and second demodulation order, dipole-active oscillators can be identified as spectral features in the ratio $\tilde{E}_3/\tilde{E}_2$.

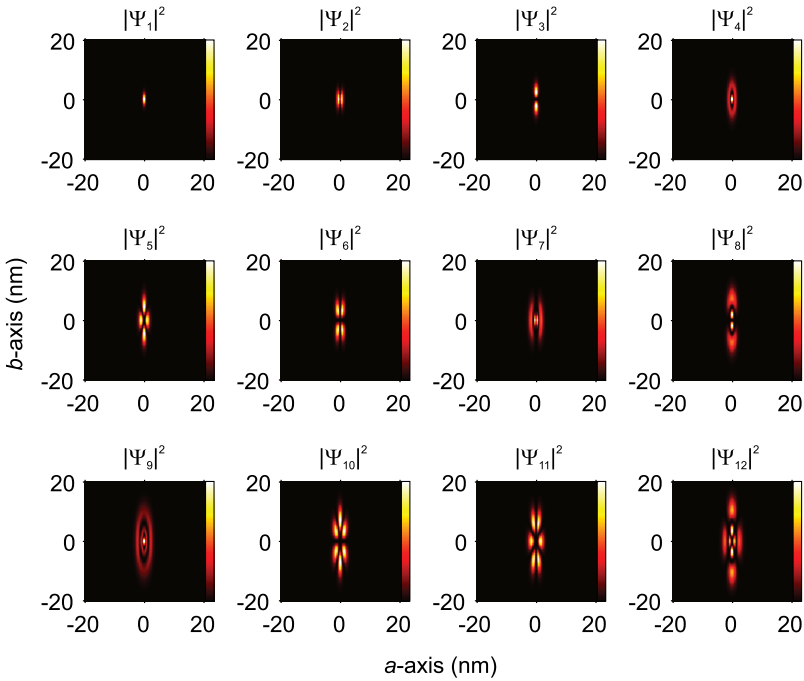

Figure B.3 | Calculated probability density of the first twelve exciton wavefunctions in monolayer CrSBr.

However, when the signature of $\tilde{E}_3/\tilde{E}_2$ is spectrally flat, the equilibrium dielectric function can be assumed flat, which is the case for the CrSBr monolayer as shown in Figure B.4b,c. Reflectance measurements have revealed a steady-state dielectric background of $\varepsilon_{\mathrm{eq}} = 10$ in bulk CrSBr[34], which we use as an estimate of the monolayer dielectric function.

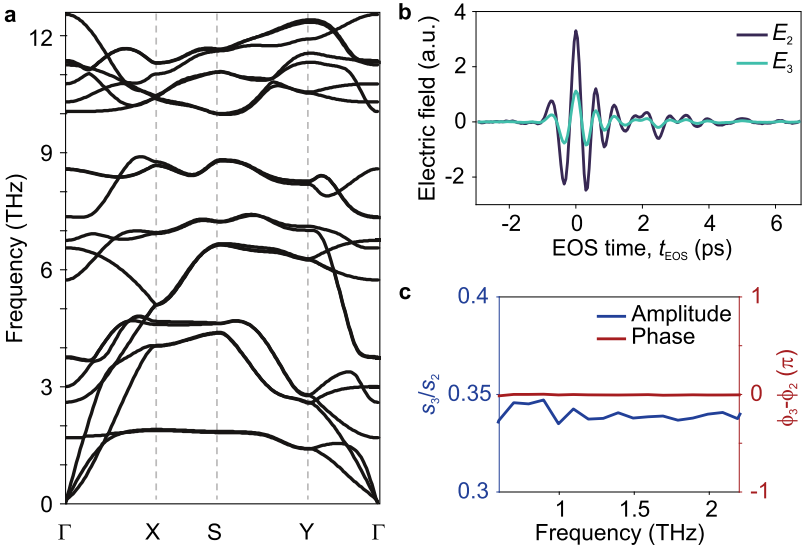

Figure B.4 | Phonon spectrum and steady-state harmonics nanospectroscopy of monolayer CrSBr. a, Calculated phonon dispersion of CrSBr, adapted from Reference 81. **b**, Electro-optically detected scattered terahertz near field at the second and third harmonic of the tip oscillation frequency, E_2 (dark blue) and E_3 (teal). **c**, Relative spectral amplitude, s_3/s_2 (blue), and phase, $\phi_3 - \phi_2$ (red). The flat spectral response indicates a constant equilibrium dielectric function.

Appendix C

Details on the characterisation of ultrashort light pulses

C.1 Frequency-resolved optical gating of the utilized laser pulses

Knowing the temporal shape of ultrashort pump pulses is essential for ultrafast pump-probe experiments, as pulses featuring the same time-integrated frequency spectrum can trigger different dynamics if their dispersion varies. Thus, it is imperative to characterise the complex-valued spectrum of the employed laser pulses. Frequency-resolved optical gating (FROG)[234] is one of the most wide-spread techniques to determine both the temporal intensity envelope and the dispersion of femtosecond pulses. In this work, second harmonic FROG is used, where two copies of the same ultrashort pulse are spatially overlapped in a nonlinear crystal. The generated sum frequency spectrum is resolved as a function of the delay time between the two identical pulses. Consequently, a spectrogram or FROG trace is obtained, which contains the information about the complex-valued spectrum. It is retrieved by an iterative algorithm reconstructing the measured FROG trace[235]. Owing to the temporal symmetry of the spectrogram, the carrier-envelope phase and the sign of the phase are not determined. The sign can be revealed by a FROG measurement with an additional medium with known dispersion.

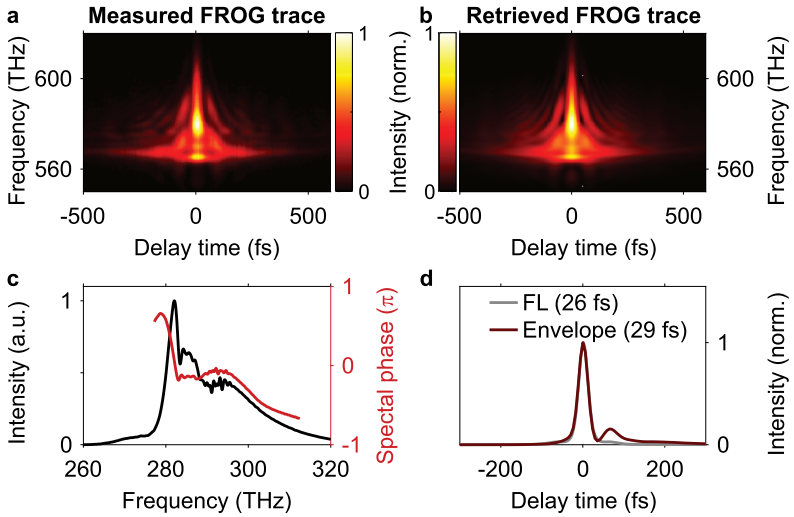

Figure C.1 | FROG of the compressed laser pulses for a medium centred in the compression cell. a, Measured FROG spectrogram. **b**, Retrieved FROG spectrogram. **c**, Reconstructed spectral amplitude (black) and phase (red). **d**, Reconstructed temporal intensity envelope (red) and intensity envelope of the Fourier-limited (FL) pulse with the same spectrum. The respective full width at half maximum is given in parentheses.

In Section 6.3, the laser pulses used to generate and gate the intense, broadband terahertz pulses are compressed in a multi-pass cell compression scheme. The amount of spectral broadening and, thus, the temporal compression was tuned by moving the nonlinear medium along the beam axis of the cell. Figures C.1 to C.5 depict the recorded and retrieved FROG traces as well as the complex-valued Fourier spectrum and temporal intensity envelope of the reconstructed pulse for different distances of the nonlinear medium from the centre of the multi-pass cell.

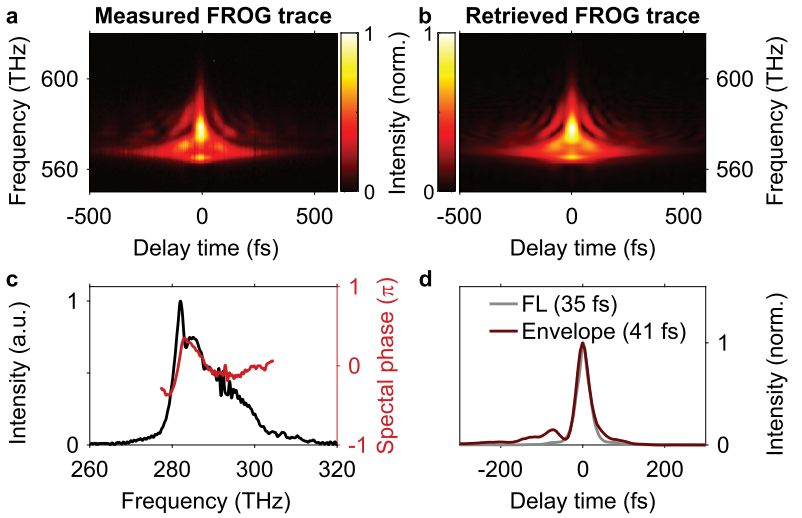

Figure C.2 | FROG of the compressed laser pulses for a medium placed 10 cm from the centre of the compression cell. **a**, Measured FROG spectrogram. **b**, Retrieved FROG spectrogram. **c**, Reconstructed spectral amplitude (black) and phase (red). **d**, Reconstructed temporal intensity envelope (red) and intensity envelope of the Fourier-limited (FL) pulse with the same spectrum. The respective full width at half maximum is given in parentheses.

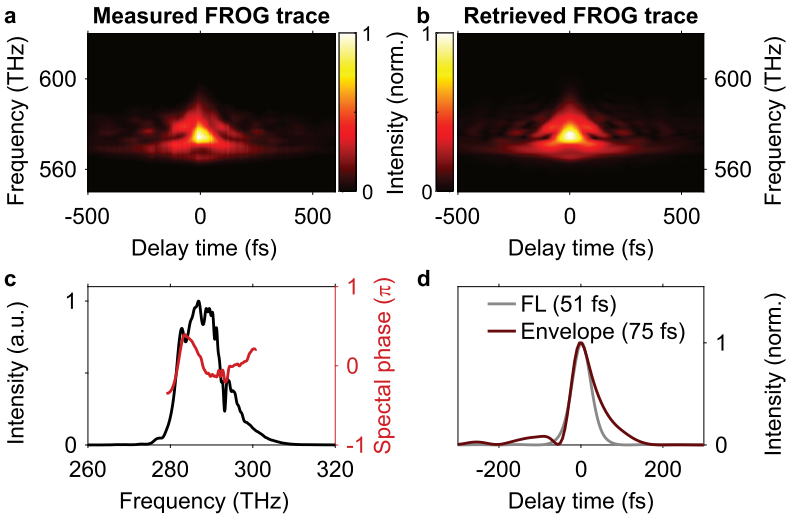

Figure C.3 | FROG of the compressed laser pulses for a medium placed 20 cm from the centre of the compression cell. **a**, Measured FROG spectrogram. **b**, Retrieved FROG spectrogram. **c**, Reconstructed spectral amplitude (black) and phase (red). **d**, Reconstructed temporal intensity envelope (red) and intensity envelope of the Fourier-limited (FL) pulse with the same spectrum. The respective full width at half maximum is given in parentheses.

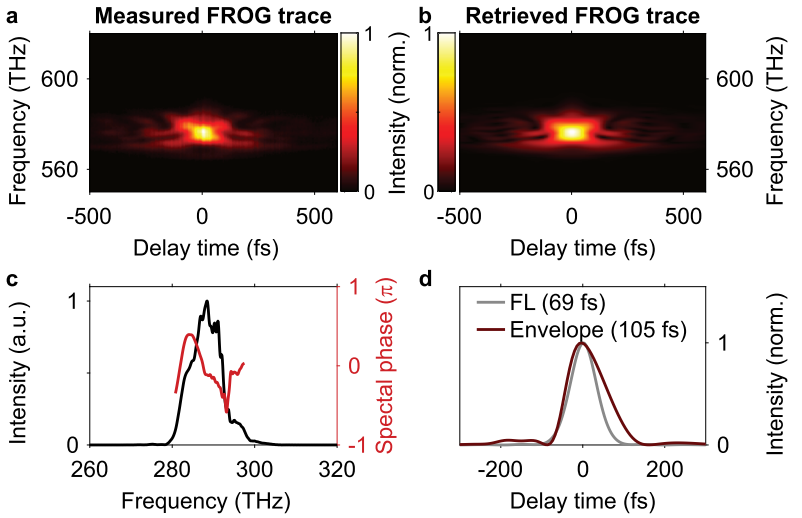

Figure C.4 | FROG of the compressed laser pulses for a medium placed 30 cm from the centre of the compression cell. a, Measured FROG spectrogram. **b**, Retrieved FROG spectrogram. **c**, Reconstructed spectral amplitude (black) and phase (red). **d**, Reconstructed temporal intensity envelope (red) and intensity envelope of the Fourier-limited (FL) pulse with the same spectrum. The respective full width at half maximum is given in parentheses.

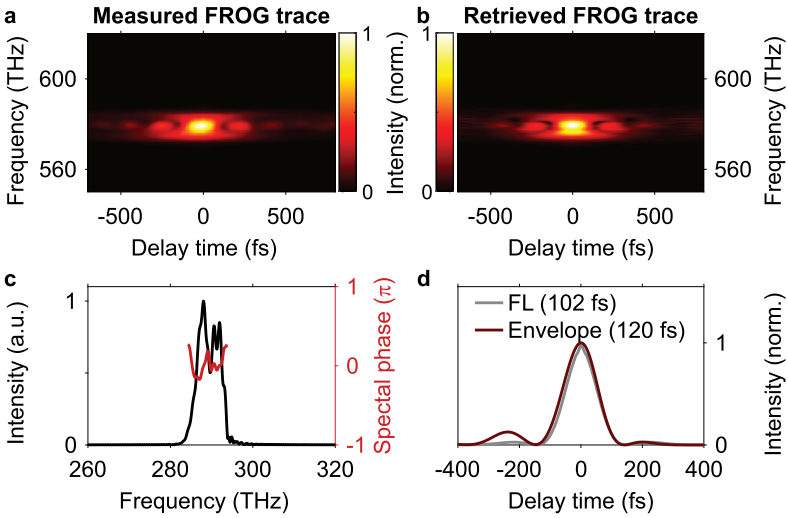

Figure C.5 | FROG of the compressed laser pulses without a medium in the compression cell. **a**, Measured FROG spectrogram. **b**, Retrieved FROG spectrogram. **c**, Reconstructed spectral amplitude (black) and phase (red). **d**, Reconstructed temporal intensity envelope (red) and intensity envelope of the Fourier-limited (FL) pulse with the same spectrum. The respective full width at half maximum is given in parentheses.

C.2 Calculating the electro-optic detector response

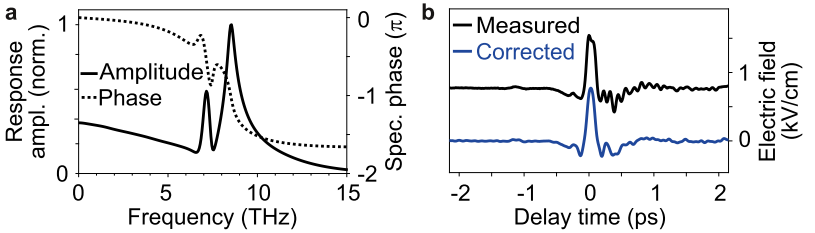

Figure C.6 | Detector response of GaSe. a, Response amplitude (solid line) and phase (dotted line) of a GaSe crystal with a thickness of 6 µm combined with a gate pulse with a duration of 75 fs. **b**, Electro-optic signal (black) and waveform corrected for the detector response shown in **a** (blue). The waveforms are offset for clarity.

In this work, for retrieval of the actual terahertz waveforms from the measured electro-optic signal, the complex-valued response function of the respective detection crystals, a gallium phosphide crystal with a thickness of 2 mm (Section 3.4) a gallium selenide crystal with a thickness of 6 µm (Section 6.3.2), is calculated following References 44 and 236. The employed method takes into account the mismatch of the terahertz phase velocity and group velocity of the gating pulse, absorption in the detector and dispersion of the second-order nonlinearity. The correction was only applied for Fourier components featuring an amplitude above the noise floor of the measurement to avoid unphysical amplification of noise. Figure C.6 shows the complex-valued detector response for a gate pulse with a duration of 75 fs, and the electro-optically detected (Figure C.6b, black, offset for clarity) as well as the corrected terahertz waveform (Figure C.6b, blue).

C.3 Determining the number of optical cycles

Chapter 6 discusses the generation of sub-cycle terahertz pulses. At first read, the existence of a light pulse featuring a *sub-cycle* waveform might seem counter-intuitive: Maxwell's equations require propagating far-field waves to oscillate, prohibiting a strict half-cycle transient, which solely features electric field components of the same

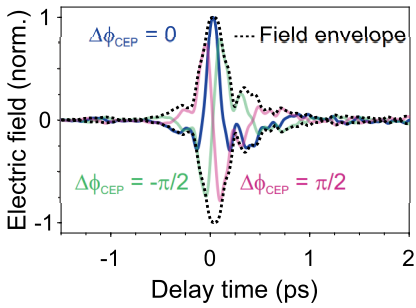

Figure C.7 | Identifying the field envelope of a subcycle waveform. The field envelope (black) of a phase-stable, subcycle laser pulse (blue) can be obtained by shifting its carrier-envelope phase Φ_{CEP} and tracking the maximum of the electric field at each delay time.

sign. It is therefore essential to clarify what property makes a *single- or sub-cycle* light pulse. In this thesis and across the field of ultrafast photonics, the duration of an optical pulse, τ_{p}, is determined by the full width at half maximum of the intensity envelope[237]. Consequently, the number of optical cycles, n_{cycles}, is determined as the ratio of the oscillation period, T_{c}, corresponding to the centre frequency, f_{c}, divided by the pulse duration,

$$n_{\mathrm{cycles}} = \frac{\tau_{\mathrm{p}}}{T_{\mathrm{c}}} = f_{\mathrm{c}} \cdot \tau_{\mathrm{p}}. \tag{C.1}$$

The centre frequency is typically calculated based on energetic weight, that is

$$f_{\mathrm{c}} = \frac{1}{2\pi} \frac{\int \omega |E(\omega)|^2 \, \mathrm{d}\omega}{\int |E(\omega)|^2 \, \mathrm{d}\omega}, \tag{C.2}$$

where $|E(\omega)|^2$ is the intensity spectrum of the laser pulse.

For single- and sub-cycle pulses, the pulse duration is on the order of the oscillation period, that is, $\tau_{\mathrm{p}} \sim T_{\mathrm{c}}$. In this regime, it is not straightforward to specify a field envelope. Thus, we use a rigorous method to determine the field envelope of any waveform: When the carrier-envelope phase of the considered field transient is shifted continuously from $-\pi$ to π, the extrema at each point in time trace the field envelope (see Figure C.7). Numerically, the Hilbert transform $H[...]$[238] is used to calculate the

amplitude envelope $A(t)$ of the transient electric field $E(t)$:

$$A(t) = \sqrt{E(t)^2 + H[E(t)]^2}. \tag{C.3}$$

The intensity envelope is then given by $I(t) = A(t)^2$. For envelopes, which can be approximated by functions featuring a finite time-bandwidth product like a Gaussian or sech^2, the full width at half maximum is an accurate measure of τ_p.

Appendix D

Strain-free grown epitaxial quantum wells

The quantum well emitters described in Chapter 6 were grown on a semi-insulating (100) GaAs substrate by molecular beam epitaxy. To overcome the lattice-mismatch of 1% between the GaAs substrate and the active layers, an $In_xAl_{1-x}As$ step-graded buffer was utilised (see Figure D.1). There, the indium content was increased from $x = 0$ to 0.15 in three 50 nm steps ($x = 0.05$, 0.10 and 0.15) and a 50 nm step back to $x = 0.124$. An $In_{0.124}Al_{0.876}As$ layer with a thickness of 100 nm grown on top of the buffer serves as a lattice-matched virtual substrate for the following active layers. The active layers are composed as follows: InAlAs provides the QW potential walls, while the type-II heterostructure quantum well is built from a suitable combination of InGaAs and GaAsSb. The quantum well is formed by 7 nm of $In_{0.141}Ga_{0.859}As$ and 7 nm of $GaAs_{0.87}Sb_{0.13}$. Each quantum well is embedded into 30 nm $In_{0.124}Al_{0.876}As$ on each side, acting as potential barriers. The heterostructures were capped with 2 nm of $In_{0.141}Ga_{0.859}As$ to prevent oxidation damage. The buffer was grown at a substrate temperature, $T = 335\,°C$, while the active layers were grown at $T = 450 - 470\,°C$.

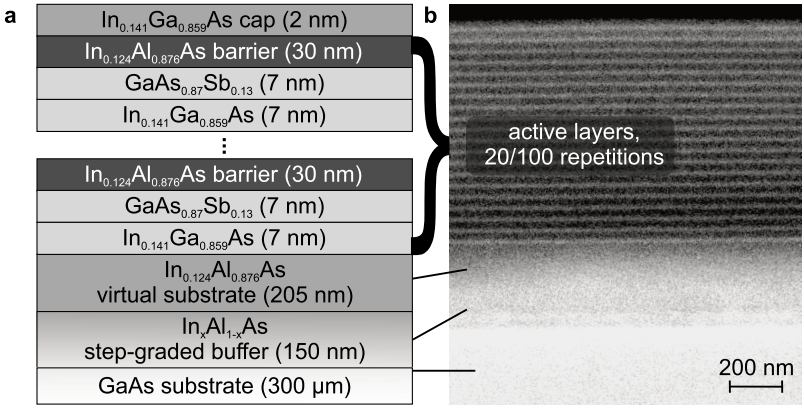

Figure D.1 | Structure of the epitaxially grown quantum well terahertz emitters. a, Schematic composition of the quantum well emitters: An InAlAs-based virtual substrate and step-graded buffer are epitaxially grown onto a GaAs substrate in order to overcome the lattice mismatch of the substrate and the active layers. The latter consist of GaAsSb and InGaAs as well as InAlAs potential barriers. The heterostructures are capped with InGaAs to prevent oxidation of the active layers. **b**, Scanning electron microscope image of a quantum well emitter with 20 repetitions of active layers, cut along the growth direction. The corresponding layers from the schematic sketch in **a** are indicated with lines.

Scientific record

Publications in peer-reviewed journals

- Philipp Merkl, Matthias Knorr, Christian Meineke, Lukas Kastner, Dominik Peller & Rupert Huber
  Multibranch pulse synthesis and electro-optic detection of subcycle multi-terahertz electric fields
  Optics Letters **44**, 5521-5524 (2019) | DOI:10.1364/OL.44.005521

- Christian Meineke*, Michael Prager*, Johannes Hayes, Qiannan Wen*, Lukas Z. Kastner, Dieter Schuh, Kilian Fritsch, Oleg Pronin, Markus Stein, Felix Schäfer, Sangam Chatterjee, Mackillo Kira, Rupert Huber & Dominique Bougeard
  * equal contributions
  Scalable high-repetition-rate sub-half-cycle terahertz pulses from spatially indirect interband transitions
  Light: Science & Applications **11**, 151 (2022) | DOI:10.1038/s41377-022-00824-6

- Martin Zizlsperger, Svenja Nerreter, Qimu Yuan, Kilian B. Lohmann, Fabian Sandner, Felix Schiegl, Christian Meineke, Yaroslav Gerasimenko, Laura M. Herz, Tom Siday, Markus A. Huber, Michael B. Johnston & Rupert Huber
  In-situ imaging of single-grain nano-morphology and ultrafast carrier dynamics in metal halide perovskites
  accepted in principle

- Christian Meineke, Jakob Schlosser, Martin Zizlsperger, Marlene Liebich, Niloufar Nilforoushan, Kseniia Mosina, Sophia Terres, Zdenek Sofer, Alexey Chernikov, Markus A. Huber, Matthias Florian, Mackillo Kira, Florian Dirnberger & Rupert Huber
  Ultrafast exciton dynamics in the atomically thin van der Waals magnet CrSBr
  Nano Letters **24**, 4101-4107 (2024) | DOI:10.1021/acs.nanolett.3c05010

Publications in international conference proceedings

- Christian Meineke, Michael Prager, Johannes Hayes, Qiannan Wen, Lukas Z. Kastner, Dieter Schuh, Kilian Fritsch, Oleg Pronin, Markus Stein, Felix Schäfer, Sangam Chatterjee, Mackillo Kira, Dominique Bougeard & Rupert Huber
  A flexible high-repetition-rate source of sub-half-cycle terahertz pulses based on spatially indirect interband transitions
  47th International Conference on Infrared, Millimeter and Terahertz Waves 2022
  DOI:10.1109/IRMMW-THz50927.2022.9895658

- Christian Meineke, Michael Prager, Johannes Hayes, Qiannan Wen, Lukas Z. Kastner, Dominique Bougeard, Mackillo Kira & Rupert Huber
  Intense Sub-Half-Cycle Terahertz Waveforms for Lightwave-Driven Scanning Tunnelling Microscopy
  23rd International Conference on Transparent Optical Networks (ICTON 2023)
  DOI:10.1109/ICTON59386.2023.10207294

Contributions at conferences as presenting author

- **47th International Conference on Infrared, Millimeter and Terahertz Waves 2022**
  28 August – 2 September 2022 | Delft, The Netherlands
  Poster

  Christian Meineke, Michael Prager, Johannes Hayes, Qiannan Wen, Lukas Z. Kastner, Dieter Schuh, Kilian Fritsch, Oleg Pronin, Markus Stein, Felix Schäfer, Sangam Chatterjee, Mackillo Kira, Dominique Bougeard & Rupert Huber
  A flexible high-repetition-rate source of sub-half-cycle terahertz pulses based on spatially indirect interband transitions

- **DPG-Tagung der Sektion Kondensierte Materie (SKM) 2022**
  4 – 9 September 2022 | Regensburg, Germany
  Contributed Talk

  Christian Meineke, Michael Prager, Johannes Hayes, Qiannan Wen, Lukas Z. Kastner, Dieter Schuh, Kilian Fritsch, Oleg Pronin, Markus Stein, Sangam Chatterjee, Mackillo Kira, Rupert Huber & Dominique Bougeard
  Generation of intense sub-half-cycle terahertz pulses from spatially indirect interband transitions

- **23rd International Conference on Transparent Optical Networks**
  2 – 6 July 2023 | Bucharest, Romania
  Invited talk

  Christian Meineke, Michael Prager, Johannes Hayes, Qiannan Wen, Lukas Z. Kastner, Dominique Bougeard, Mackillo Kira & Rupert Huber
  Intense sub-half-cycle terahertz waveforms for lightwave-driven scanning tunneling microscopy

References

1. Fermi, E. Zur Quantelung des idealen einatomigen Gases. *Zeitschrift für Physik* **36**, 902–912 (1926).

2. Bloch, F. Über die Quantenmechanik der Elektronen in Kristallgittern. *Zeitschrift für Physik* **52**, 555–600 (1929).

3. The Theory of a Fermi Liquid. *Soviet Physics JETP* **3**, 920–925 (1957).

4. Cava, R., De Leon, N. & Xie, W. Introduction: Quantum Materials. *Chemical Reviews* **121**, 2777–2779 (2021).

5. Orenstein, J. Ultrafast spectroscopy of quantum materials. *Physics Today* **65**, 44–50 (2012).

6. The rise of quantum materials. *Nature Physics* **12**, 105 (2016).

7. Geim, A. K. & Novoselov, K. S. The rise of graphene. *Nature Materials* **6**, 183–191 (2007).

8. Xia, F., Wang, H., Xiao, D., Dubey, M. & Ramasubramaniam, A. Two-dimensional material nanophotonics. *Nature Photonics* **8**, 899–907 (2014).

9. Chhowalla, M., Jena, D. & Zhang, H. Two-dimensional semiconductors for transistors. *Nature Reviews Materials* **1**, 16052 (2016).

10. Daus, A. *et al.* High-performance flexible nanoscale transistors based on transition metal dichalcogenides. *Nature Electronics* **4**, 495–501 (2021).

11. He, K. *et al.* Tightly bound excitons in monolayer WSe_2. *Physical Review Letters* **113**, 026803 (2014).

12. Schaibley, J. R. *et al.* Valleytronics in 2D materials. *Nature Reviews Materials* **1**, 16055 (2016).

13. Chernikov, A. *et al.* Exciton binding energy and nonhydrogenic Rydberg series in monolayer WS_2. *Physical Review Letters* **113**, 076802 (2014).

14. Steinleitner, P. *et al.* Direct Observation of Ultrafast Exciton Formation in a Monolayer of WSe_2. *Nano Letters* **17**, 1455–1460 (2017).

15. Huang, B. *et al.* Layer-dependent ferromagnetism in a van der Waals crystal down to the monolayer limit. *Nature* **546**, 270–273 (2017).

16. Gong, C. *et al.* Discovery of intrinsic ferromagnetism in two-dimensional van der Waals crystals. *Nature* **546**, 265–269 (2017).

17. Burch, K. S., Mandrus, D. & Park, J. G. Magnetism in two-dimensional van der Waals materials. *Nature* **563**, 47–52 (2018).

18. Gibertini, M., Koperski, M., Morpurgo, A. F. & Novoselov, K. S. Magnetic 2D materials and heterostructures. *Nature Nanotechnology* **14**, 408–419 (2019).

19. Klein, J. *et al.* The Bulk van der Waals Layered Magnet CrSBr is a Quasi-1D Material. *ACS Nano* **17**, 5316–5328 (2023).

20. Akiyama, H. One-dimensional excitons in GaAs quantum wires. *Journal of Physics Condensed Matter* **10**, 3095–3139 (1998).

21. Remskar, M. *et al.* Self-Assembly of Subnanometer-Diameter Single-Wall MoS_2 Nanotubes. *Science* **292**, 479–481 (2001).

22. Wang, J., Graham, M. W., Ma, Y., Fleming, G. R. & Kaindl, R. A. Ultrafast spectroscopy of midinfrared internal exciton transitions in separated single-walled carbon nanotubes. *Physical Review Letters* **104**, 177401 (2010).

23. Bai, Y. *et al.* Excitons in strain-induced one-dimensional moiré potentials at transition metal dichalcogenide heterojunctions. *Nature Materials* **19**, 1068–1073 (2020).

24. Bae, Y. J. *et al.* Exciton-coupled coherent magnons in a 2D semiconductor. *Nature* **609**, 282–286 (2022).

25. Diederich, G. M. *et al.* Tunable interaction between excitons and hybridized magnons in a layered semiconductor. *Nature Nanotechnology* **18**, 23–28 (2023).

26. Qian, T.-X., Zhou, J., Cai, T.-Y. & Ju, S. Anisotropic electron-hole excitation and large linear dichroism in the two-dimensional ferromagnet CrSBr with in-plane magnetization. *Physical Review Research* **5**, 033143 (2023).

27. Telford, E. J. *et al.* Layered Antiferromagnetism Induces Large Negative Magnetoresistance in the van der Waals Semiconductor CrSBr. *Advanced Materials* **32**, 2003240 (2020).

28. Lee, K. *et al.* Magnetic Order and Symmetry in the 2D Semiconductor CrSBr. *Nano Letters* **21**, 3511–3517 (2021).

29. Avsar, A. Highly anisotropic van der Waals magnetism. *Nature Materials* **21**, 729–739 (2022).

30. Liu, W. *et al.* A Three-Stage Magnetic Phase Transition Revealed in Ultrahigh-Quality van der Waals Bulk Magnet CrSBr. *ACS Nano* **16**, 15917–15926 (2022).

31. Wang, Q. H. *et al.* The Magnetic Genome of Two-Dimensional van der Waals Materials. *ACS Nano* **16**, 6960–7079 (2022).

32. Rizzo, D. J. *et al.* Visualizing Atomically Layered Magnetism in CrSBr. *Advanced Materials* **34**, 2201000 (2022).

33. Dirnberger, F. *et al.* Magneto-optics in a van der Waals magnet tuned by self-hybridized polaritons. *Nature* **620**, 533–538 (2023).

34. Wang, T. *et al.* Magnetically-dressed CrSBr exciton-polaritons in ultrastrong coupling regime. *Nature Communications* **14**, 5966 (2023).

35. Wang, G. *et al.* Colloquium: Excitons in atomically thin transition metal dichalcogenides. *Reviews of Modern Physics* **90**, 21001 (2018).

36. Poellmann, C. *et al.* Resonant internal quantum transitions and femtosecond radiative decay of excitons in monolayer WSe_2. *Nature Materials* **14**, 889–893 (2015).

37. Merkl, P. *et al.* Proximity control of interlayer exciton-phonon hybridization in van der Waals heterostructures. *Nature Communications* **12**, 1719 (2021).

38. Frenzel, M. *et al.* Nonlinear terahertz control of the lead halide perovskite lattice. *Science Advances* **9**, eadg3856 (2023).

39. Kampfrath, T. *et al.* Coherent terahertz control of antiferromagnetic spin waves. *Nature Photonics* **5**, 31–34 (2011).

40. Schlauderer, S. *et al.* Temporal and spectral fingerprints of ultrafast all-coherent spin switching. *Nature* **569**, 383–387 (2019).

41. Rongione, E. *et al.* Emission of coherent THz magnons in an antiferromagnetic insulator triggered by ultrafast spin–phonon interactions. *Nature Communications* **14**, 1818 (2023).

42. Huber, R. *et al.* How many-particle interactions develop after ultrafast excitation of an electron-hole plasma. *Nature* **414**, 286–289 (2001).

43. Ulbricht, R., Hendry, E., Shan, J., Heinz, T. F. & Bonn, M. Carrier dynamics in semiconductors studied with time-resolved terahertz spectroscopy. *Reviews of Modern Physics* **83**, 543–586 (2011).

44. Huber, R., Brodschelm, A., Tauser, F. & Leitenstorfer, A. Generation and field-resolved detection of femtosecond electromagnetic pulses tunable up to 41 THz. *Applied Physics Letters* **76**, 3191–3193 (2000).

45. Kübler, C., Huber, R., Tübel, S. & Leitenstorfer, A. Ultrabroadband detection of multi-terahertz field transients with GaSe electro-optic sensors: Approaching the near infrared. *Applied Physics Letters* **85**, 3360–3362 (2004).

46. Merkl, P. *et al.* Ultrafast transition between exciton phases in van der Waals heterostructures. *Nature Materials* **18**, 691–696 (2019).

47. Abbe, E. Beiträge zur Theorie des Mikroskops und der mikroskopischen Wahrnehmung. *Archiv für mikroskopische Anatomie* **9**, 413–468 (1873).

48. Ash, E. A. & Nicholls, G. Super-resolution aperture scanning microscope. *Nature* **237**, 510–512 (1972).

49. Zenhausern, F., O'Boyle, M. & Wickramasinghe, H. K. Apertureless near-field optical microscope. *Applied Physics Letters* **65**, 1623–1625 (1994).

50. Inouye, Y. & Kawata, S. Near-field scanning optical microscope with a metallic probe tip. *Optics Letters* **19**, 159–161 (1994).

51. Hillenbrand, R. & Keilmann, F. Complex optical constants on a subwavelength scale. *Physical Review Letters* **85**, 3029–3032 (2000).

52. Hillenbrand, R., Taubner, T. & Keilmann, F. Phonon-enhanced light-matter interaction at the nanometre scale. *Nature* **418**, 159–162 (2002).

53. Raschke, M. B. & Lienau, C. Apertureless near-field optical microscopy: Tip-sample coupling in elastic light scattering. *Applied Physics Letters* **83**, 5089–5091 (2003).

54. Wagner, M. *et al.* Ultrafast and nanoscale plasmonic phenomena in exfoliated graphene revealed by infrared pump-probe nanoscopy. *Nano Letters* **14**, 894–900 (2014).

55. Huber, M. A. *et al.* Femtosecond photo-switching of interface polaritons in black phosphorus heterostructures. *Nature Nanotechnology* **12**, 207–211 (2017).

56. Plankl, M. *et al.* Subcycle contact-free nanoscopy of ultrafast interlayer transport in atomically thin heterostructures. *Nature Photonics* **15**, 594–600 (2021).

57. Siday, T. *et al.* Ultrafast Nanoscopy of High-Density Exciton Phases in WSe_2. *Nano Letters* **22**, 2561–2568 (2022).

58. Cocker, T. L., Peller, D., Yu, P., Repp, J. & Huber, R. Tracking the ultrafast motion of a single molecule by femtosecond orbital imaging. *Nature* **539**, 263–267 (2016).

59. Peller, D. *et al.* Sub-cycle atomic-scale forces coherently control a single-molecule switch. *Nature* **585**, 58–62 (2020).

60. Müller, M., Martín Sabanés, N., Kampfrath, T. & Wolf, M. Phase-Resolved Detection of Ultrabroadband THz Pulses inside a Scanning Tunneling Microscope Junction. *ACS Photonics* **7**, 2046–2055 (2020).

61. Peller, D. *et al.* Quantitative sampling of atomic-scale electromagnetic waveforms. *Nature Photonics* **15**, 143–147 (2021).

62. Yoshida, S. *et al.* Terahertz Scanning Tunneling Microscopy for Visualizing Ultrafast Electron Motion in Nanoscale Potential Variations. *ACS Photonics* **8**, 315–323 (2021).

63. Cao, Y. *et al.* Unconventional superconductivity in magic-angle graphene superlattices. *Nature* **556**, 43–50 (2018).

64. Merkl, P. *et al.* Twist-tailoring Coulomb correlations in van der Waals homobilayers. *Nature Communications* **11**, 2167 (2020).

65. Balents, L., Dean, C. R., Efetov, D. K. & Young, A. F. Superconductivity and strong correlations in moiré flat bands. *Nature Physics* **16**, 725–733 (2020).

66. Miao, S. *et al.* Strong interaction between interlayer excitons and correlated electrons in WSe2/WS2 moiré superlattice. *Nature Communications* **12**, 8–13 (2021).

67. Wilson, N. P., Yao, W., Shan, J. & Xu, X. Excitons and emergent quantum phenomena in stacked 2D semiconductors. *Nature* **599**, 383–392 (2021).

68. Huang, D., Choi, J., Shih, C. K. & Li, X. Excitons in semiconductor moiré superlattices. *Nature Nanotechnology* **17**, 227–238 (2022).

69. Bonilla, M. *et al.* Strong roomerature ferromagnetism in VSe_2 monolayers on van der Waals substrates. *Nature Nanotechnology* **13**, 289–293 (2018).

70. Fei, Z. *et al.* Two-dimensional itinerant ferromagnetism in atomically thin Fe_3GeTe_2. *Nature Materials* **17**, 778–782 (2018).

71. Seyler, K. L. *et al.* Ligand-field helical luminescence in a 2D ferromagnetic insulator. *Nature Physics* **14**, 277–281 (2018).

72. Sun, Z. *et al.* Giant nonreciprocal second-harmonic generation from antiferromagnetic bilayer CrI_3. *Nature* **572**, 497–501 (2019).

73. Sivadas, N., Daniels, M. W., Swendsen, R. H., Okamoto, S. & Xiao, D. Magnetic ground state of semiconducting transition-metal trichalcogenide monolayers. *Physical Review B - Condensed Matter and Materials Physics* **91**, 235425 (2015).

74. Calder, S. *et al.* Magnetic structure and exchange interactions in the layered semiconductor $CrPS_4$. *Physical Review B* **102**, 024408 (2020).

75. Long, G. *et al.* Persistence of Magnetism in Atomically Thin $MnPS_3$ Crystals. *Nano Letters* **20**, 2452–2459 (2020).

76. Chu, H. *et al.* Linear Magnetoelectric Phase in Ultrathin $MnPS_3$ Probed by Optical Second Harmonic Generation. *Physical Review Letters* **124**, 27601 (2020).

77. Kang, S. *et al.* Coherent many-body exciton in van der Waals antiferromagnet $NiPS_3$. *Nature* **583**, 785–789 (2020).

78. Hwangbo, K. *et al.* Highly anisotropic excitons and multiple phonon bound states in a van der Waals antiferromagnetic insulator. *Nature Nanotechnology* **16**, 655–660 (2021).

79. Dirnberger, F. *et al.* Spin-correlated exciton–polaritons in a van der Waals magnet. *Nature Nanotechnology* **17**, 1060–1064 (2022).

80. Xu, X. *et al.* Strong Spin-Phonon Coupling in Two-Dimensional Magnetic Semiconductor CrSBr. *Journal of Physical Chemistry C* **126**, 10574–10583 (2022).

81. Torres, K. *et al.* Probing Defects and Spin-Phonon Coupling in CrSBr via Resonant Raman Scattering. *Advanced Functional Materials* **2023**, 2211366 (2023).

82. Pawbake, A. *et al.* Raman scattering signatures of strong spin-phonon coupling in the bulk magnetic van der Waals material CrSBr. *Physical Review B* **107**, 075421 (2023).

83. Göser, O., Paul, W. & Kahle, H. G. Magnetic properties of CrSBr. *Journal of Magnetism and Magnetic Materials* **92**, 129–136 (1990).

84. Mermin, N. D. & Wagner, H. Absence of ferromagnetism or antiferromagnetism in one- or two-dimensional isotropic Heisenberg models. *Physical Review Letters* **17**, 1133–1136 (1966).

85. Telford, E. J. *et al.* Coupling between magnetic order and charge transport in a two-dimensional magnetic semiconductor. *Nature Materials* **21**, 754–760 (2022).

86. Esteras, D. L., Rybakov, A., Ruiz, A. M. & Baldoví, J. J. Magnon Straintronics in the 2D van der Waals Ferromagnet CrSBr from First-Principles. *Nano Letters* **22**, 8771–8778 (2022).

87. Zheng, Y. *et al.* Paramagnon drag in high thermoelectric figure of merit Li-doped MnTe. *Science Advances* **5**, eaat9461 (2019).

88. Wang, L. *et al.* Paramagnons and high-temperature superconductivity in a model family of cuprates. *Nature Communications* **13**, 3163 (2022).

89. Wu, F. *et al.* Quasi-1D Electronic Transport in a 2D Magnetic Semiconductor. *Advanced Materials* **34**, 2109759 (2022).

90. Qiao, J., Kong, X., Hu, Z. X., Yang, F. & Ji, W. High-mobility transport anisotropy and linear dichroism in few-layer black phosphorus. *Nature Communications* **5**, 4475 (2014).

91. Bianchi, M. *et al.* Paramagnetic Electronic Structure of CrSBr: Comparison between Ab Initio GW Theory and Angle-Resolved Photoemission Spectroscopy. *Physical Review B* **107**, 235107 (2023).

92. Frenkel, J. On the transformation of light into heat in solids. *Physical Review* **37**, 17–44 (1931).

93. Wannier, G. H. The structure of electronic excitation levels in insulating crystals. *Physical Review* **52**, 191–197 (1937).

94. Haug, H. & Koch, S. W. *Quantum Theory of the Optical and Electronic Properties of Semiconductors* (World Scientific, 2004).

95. Ye, Z. *et al.* Probing excitonic dark states in single-layer tungsten disulphide. *Nature* **513**, 214–218 (2014).

96. Ugeda, M. M. *et al.* Giant bandgap renormalization and excitonic effects in a monolayer transition metal dichalcogenide semiconductor. *Nature Materials* **13**, 1091–1095 (2014).

97. Wilson, N. P. *et al.* Interlayer electronic coupling on demand in a 2D magnetic semiconductor. *Nature Materials* **20**, 1657–1662 (2021).

98. Malic, E. *et al.* Dark excitons in transition metal dichalcogenides. *Physical Review Materials* **2**, 014002 (2018).

99. Wang, F. *et al.* Exciton polarizability in semiconductor nanocrystals. *Nature Materials* **5**, 861–864 (2006).

100. Leitenstorfer, A. *et al.* The 2023 terahertz science and technology roadmap. *Journal of Physics D: Applied Physics* **56**, 223001 (2023).

101. Mitrofanov, O. *et al.* Terahertz near-field microscopy based on a collection mode detector. *Applied Physics Letters* **77**, 3496–3498 (2000).

102. Dürig, U., Pohl, D. W. & Rohner, F. Near-field optical-scanning microscopy. *Journal of Applied Physics* **59**, 3318–3327 (1986).

103. Lahrech, A., Bachelot, R., Gleyzes, P. & Boccara, A. C. Infrared-reflection-mode near-field microscopy using an apertureless probe with a resolution of $\lambda/600$. *Optics Letters* **21**, 1315 (1996).

104. Moon, K. *et al.* Quantitative coherent scattering spectra in apertureless terahertz pulse near-field microscopes. *Applied Physics Letters* **101**, 011109 (2012).

105. Eisele, M. *et al.* Ultrafast multi-terahertz nano-spectroscopy with sub-cycle temporal resolution. *Nature Photonics* **8**, 841–845 (2014).

106. Ma, E. Y. *et al.* Recording interfacial currents on the subnanometer length and femtosecond time scale by terahertz emission. *Science Advances* **5**, eaau0073 (2019).

107. Mastel, S. *et al.* Terahertz Nanofocusing with Cantilevered Terahertz-Resonant Antenna Tips. *Nano Letters* **17**, 6526–6533 (2017).

108. Mooshammer, F. *et al.* Nanoscale Near-Field Tomography of Surface States on $(Bi_{0.5}\ Sb_{0.5})_2Te_3$. *Nano Letters* **18**, 7515–7523 (2018).

109. Siday, T., Natrella, M., Wu, J., Liu, H. & Mitrofanov, O. Resonant terahertz probes for near-field scattering microscopy. *Optics Express* **25**, 27874 (2017).

110. Zenhausern, F., Martin, Y. & Wickramasinghe, H. K. Scanning Interferometric Apertureless Microscopy: Optical Imaging at 10 Angstrom Resolution. *Science* **269**, 1083–1085 (1995).

111. Knoll, B. & Keilmann, F. Near-field probing of vibrational absorption forchemical microscopy. *Nature* **399**, 134–137 (1999).

112. Chen, X. *et al.* Modern Scattering-Type Scanning Near-Field Optical Microscopy for Advanced Material Research. *Advanced Materials* **31**, 1804774 (2019).

113. Cvitkovic, A., Ocelic, N. & Hillenbrand, R. Analytical model for quantitative prediction of material contrasts in scattering-type near-field optical microscopy. *Optics Express* **15**, 8550–8565 (2007).

114. Hauer, B., Engelhardt, A. P. & Taubner, T. Quasi-analytical model for scattering infrared near-field microscopy on layered systems. *Optics Express* **20**, 13173–13188 (2012).

115. Liewald, C. *et al.* All-electronic terahertz nanoscopy. *Optica* **5**, 159–163 (2018).

116. Mester, L., Govyadinov, A. A. & Hillenbrand, R. High-fidelity nano-FTIR spectroscopy by on-pixel normalization of signal harmonics. *Nanophotonics* **11**, 377–390 (2022).

117. Ni, G. X. *et al.* Ultrafast optical switching of infrared plasmon polaritons in high-mobility graphene. *Nature Photonics* **10**, 244–247 (2016).

118. Sternbach, A. J. *et al.* Programmable hyperbolic polaritons in van der Waals semiconductors. *Science* **371**, 617–620 (2021).

119. Nishida, J. *et al.* Nanoscale heterogeneity of ultrafast many-body carrier dynamics in triple cation perovskites. *Nature Communications* **13**, 6582 (2022).

120. Klarskov, P., Kim, H., Colvin, V. L. & Mittleman, D. M. Nanoscale Laser Terahertz Emission Microscopy. *ACS Photonics* **4**, 2676–2680 (2017).

121. Cheng, L. *et al.* Far out-of-equilibrium spin populations trigger giant spin injection into atomically thin MoS_2. *Nature Physics* **15**, 347–351 (2019).

122. Pizzuto, A. *et al.* Nonlocal Time-Resolved Terahertz Spectroscopy in the near Field. *ACS Photonics* **8**, 2904–2911 (2021).

123. Kim, R. H. *et al.* Terahertz Nanoimaging of Perovskite Solar Cell Materials. *ACS Photonics* **9**, 3550–3556 (2022).

124. Wu, Q. & Zhang, X. C. Free-space electro-optic sampling of terahertz beams. *Applied Physics Letters* **67**, 3523 (1995).

125. Boyd, R. W. *Nonlinear Optics* (Academic Press, 2008).

126. Madarasz, F. L., Dimmock, J. O., Dietz, N. & Bachmann, K. J. Sellmeier parameters for $ZnGaP_2$ and GaP. *Journal of Applied Physics* **87**, 1564–1565 (2000).

127. Meyer, F., Hekmat, N., Mansourzadeh, S., Hoffmann, M. & Saraceno, C. J. Optical Rectification of a 100W Average Power Ultrafast Thin-Disk Oscillator. *Optics Letters* **43**, 5909–5912 (2018).

128. Gallot, G. & Grischkowsky, D. Electro-optic detection of terahertz radiation. *Journal of the Optical Society of America B* **16**, 1204–1212 (1999).

129. Porer, M., Ménard, J.-M. & Huber, R. Shot noise reduced terahertz detection via spectrally postfiltered electro-optic sampling. *Optics Letters* **39**, 2435 (2014).

130. Cerullo, G. & De Silvestri, S. Ultrafast optical parametric amplifiers. *Review of Scientific Instruments* **74**, 1–18 (2003).

131. Manzoni, C. & Cerullo, G. Design criteria for ultrafast optical parametric amplifiers. *Journal of Optics* **18**, 103501 (2016).

132. Musheghyan, M. *et al.* Tunable, few-cycle, CEP-stable mid-IR optical parametric amplifier for strong field applications. *Journal of Physics B: Atomic, Molecular and Optical Physics* **53** (2020).

133. Bradler, M. & Riedle, E. Sub-20 fs μJ-energy pulses tunable down to the near-UV from a 1 MHz Yb-fiber laser system. *Optics Letters* **39**, 2588 (2014).

134. Wittmann, E. *Taming Optical Parametric Amplification: Stable few cycle pulses at 210 to 10000 nm from Ti:Sapphire and Yb-based lasers.* Ph.D. thesis, LMU München (2018).

135. Alfano, R. R. *The Supercontinuum Laser Source* (Springer, New York, 2016).

136. Bradler, M., Baum, P. & Riedle, E. Femtosecond continuum generation in bulk laser host materials with sub-μJ pump pulses. *Applied Physics B: Lasers and Optics* **97**, 561–574 (2009).

137. Nillon, J., Crégut, O., Bressler, C. & Haacke, S. Two MHz tunable non collinear optical parametric amplifiers with pulse durations down to 6 fs. *Optics Express* **22**, 14964 (2014).

138. Tamošauskas, G., Beresnevičius, G., Gadonas, D. & Dubietis, A. Transmittance and phase matching of BBO crystal in the 3–5 μm range and its application for the characterization of mid-infrared laser pulses. *Optical Materials Express* **8**, 1410–1418 (2018).

139. Zhan, T., Shi, X., Dai, Y., Liu, X. & Zi, J. Transfer matrix method for optics in graphene layers. *Journal of Physics Condensed Matter* **25**, 215301 (2013).

140. Ansari, N. & Ghorbani, F. Light absorption optimization in two-dimensional transition metal dichalcogenide van der Waals heterostructures. *Journal of the Optical Society of America B* **35**, 1179 (2018).

141. Schinke, C. *et al.* Uncertainty analysis for the coefficient of band-to-band absorption of crystalline silicon. *AIP Advances* **5**, 067168 (2015).

142. Robert, C. *et al.* Exciton radiative lifetime in transition metal dichalcogenide monolayers. *Physical Review B* **93**, 205423 (2016).

143. Green, M. A. Intrinsic concentration, effective densities of states, and effective mass in silicon. *Journal of Applied Physics* **67**, 2944–2954 (1990).

144. Liebich, M. *et al.* submitted (2024).

145. Rodin, A. S., Carvalho, A. & Castro Neto, A. H. Excitons in anisotropic two-dimensional semiconducting crystals. *Physical Review B* **90**, 075429 (2014).

146. Tuan, D. V., Yang, M. & Dery, H. Coulomb interaction in monolayer transition-metal dichalcogenides. *Physical Review B* **98**, 125308 (2018).

147. Kamban, H. C., Pedersen, T. G. & Peres, N. M. Anisotropic Stark shift, field-induced dissociation, and electroabsorption of excitons in phosphorene. *Physical Review B* **102**, 115305 (2020).

148. Klein, J. *et al.* Sensing the Local Magnetic Environment through Optically Active Defects in a Layered Magnetic Semiconductor. *ACS Nano* **17**, 288–299 (2023).

149. Yoshida, S. *et al.* Subcycle Transient Scanning Tunneling Spectroscopy with Visualization of Enhanced Terahertz Near Field. *ACS Photonics* **6**, 1356–1364 (2019).

150. Sheng, S. *et al.* Launching Coherent Acoustic Phonon Wave Packets with Local Femtosecond Coulomb Forces. *Physical Review Letters* **129**, 43001 (2022).

151. Binning, G., Rohrer, H., Gerber, C. & Weibel, E. Surface Studies by Scanning Tunneling Microscopy. *Physical Review Letters* **49**, 57–61 (1982).

152. Crommie, M. F., Lutz, C. P. & Eigler, D. M. Confinement of electrons to quantum corrals on a metal surface. *Science* **262**, 218–220 (1993).

153. Repp, J., Meyer, G., Stojković, S. M., Gourdon, A. & Joachim, C. Molecules on insulating films: Scanning-tunneling microscopy imaging of individual molecular orbitals. *Physical Review Letters* **94**, 026803 (2005).

154. Natterer, F. D. *et al.* Reading and writing single-atom magnets. *Nature* **543**, 226–228 (2017).

155. Yan, S. *et al.* Influence of Domain Walls in the Incommensurate Charge Density Wave State of Cu Intercalated 1T-$TiSe_2$. *Physical Review Letters* **118**, 106405 (2017).

156. Loth, S., Etzkorn, M., Lutz, C. P., Eigler, D. M. & Heinrich, A. J. Measurement of fast electron spin relaxation times with atomic resolution. *Science* **329**, 1628–1630 (2010).

157. Hamers, R. J. & Cahill, D. G. Ultrafast time resolution in scanned probe microscopies. *Applied Physics Letters* **57**, 2031–2033 (1990).

158. Groeneveld, R. H. & Van Kempen, H. The capacitive origin of the picosecond electrical transients detected by a photoconductively gated scanning tunneling microscope. *Applied Physics Letters* **69**, 2294–2296 (1996).

159. Nunes, G. & Freeman, M. Picosecond Resolution in Scanning Tunneling Microscopy. *Science* **262**, 1029–1032 (1993).

160. Dolocan, A., Acharya, D. P., Zahl, P., Sutter, P. & Camillone, N. Two-color ultrafast photoexcited scanning tunneling microscopy. *Journal of Physical Chemistry C* **115**, 10033–10043 (2011).

161. Goulielmakis, E. *et al.* Attosecond Control and Measurement: Lightwave Electronics. *Science* **317**, 769–775 (2007).

162. Borsch, M., Meierhofer, M., Huber, R. & Kira, M. Lightwave electronics in condensed matter. *Nature Reviews Materials* **8**, 668–687 (2023).

163. Schiffrin, A. *et al.* Optical-field-induced current in dielectrics. *Nature* **493**, 70–74 (2013).

164. Schubert, O. *et al.* Sub-cycle control of terahertz high-harmonic generation by dynamical Bloch oscillations. *Nature Photonics* **8**, 119–123 (2014).

165. Hohenleutner, M. *et al.* Real-time observation of interfering crystal electrons in high-harmonic generation. *Nature* **523**, 572–575 (2015).

166. Langer, F. *et al.* Lightwave-driven quasiparticle collisions on a subcycle timescale. *Nature* **533**, 225–229 (2016).

167. Langer, F. *et al.* Lightwave valleytronics in a monolayer of tungsten diselenide. *Nature* **557**, 76–80 (2018).

168. Borsch, M. *et al.* Super-resolution lightwave tomography of electronic bands in quantum materials. *Science* **370**, 1204–1207 (2020).

169. Freudenstein, J. *et al.* Attosecond clocking of correlations between Bloch electrons. *Nature* **610**, 290–295 (2022).

170. Keldysh, L. V. Ionization in the Field of a Strong Electromagnetic Wave. *Journal of Experimental and Theoretical Physics* **20**, 1307–1314 (1965).

171. Cocker, T. L. *et al.* An ultrafast terahertz scanning tunnelling microscope. *Nature Photonics* **7**, 620–625 (2013).

172. Rauch, J. & Mourou, G. The Time Integrated Far Field for Maxwell's and D'Alembert's Equations. *Proceedings of the American Mathematical Society* **134**, 851–858 (2006).

173. Fülöp, J. A., Tzortzakis, S. & Kampfrath, T. Laser-Driven Strong-Field Terahertz Sources. *Advanced Optical Materials* **8**, 1900681 (2020).

174. Auston, D. H., Cheung, K. P. & Smith, P. R. Picosecond photoconducting Hertzian dipoles. *Applied Physics Letters* **45**, 284–286 (1984).

175. Singh, A., Pashkin, A., Winnerl, S., Helm, M. & Schneider, H. Gapless Broadband Terahertz Emission from a Germanium Photoconductive Emitter. *ACS Photonics* **5**, 2718–2723 (2018).

176. Ropagnol, X. *et al.* Intense THz Pulses with large ponderomotive potential generated from large aperture photoconductive antennas. *Optics Express* **24**, 11299–11311 (2016).

177. Sell, A., Leitenstorfer, A. & Huber, R. Phase-locked generation and field-resolved detection of widely tunable terahertz pulses with amplitudes exceeding 100 MV/cm. *Optics Letters* **33**, 2767 (2008).

178. Knorr, M. *et al.* Phase-locked multi-terahertz electric fields exceeding 13 MV/cm at a 190 kHz repetition rate. *Optics Letters* **42**, 4367 (2017).

179. Junginger, F. *et al.* Single-cycle multiterahertz transients with peak fields above 10 MV/cm. *Optics Letters* **35**, 2645 (2010).

180. Hamster, H., Sullivan, A., Gordon, S., White, W. & Falcone, R. W. Subpicosecond, electromagnetic pulses from intense laser-plasma interaction. *Physical Review Letters* **71**, 2725–2728 (1993).

181. Cook, D. J. & Hochstrasser, R. M. Intense terahertz pulses by four-wave rectification in air. *Optics Letters* **25**, 1210 (2000).

182. Thomson, M. D., Blank, V. & Roskos, H. G. Terahertz white-light pulses from an air plasma photo-induced by incommensurate two-color optical fields. *Optics Express* **18**, 23173 (2010).

183. Koulouklidis, A. D. *et al.* Observation of extremely efficient terahertz generation from mid-infrared two-color laser filaments. *Nature Communications* **11**, 292 (2020).

184. Seifert, T. *et al.* Efficient metallic spintronic emitters of ultrabroadband terahertz radiation. *Nature Photonics* **10**, 483–488 (2016).

185. Kampfrath, T. *et al.* Terahertz spin current pulses controlled by magnetic heterostructures. *Nature Nanotechnology* **8**, 256–260 (2013).

186. Yang, D. *et al.* Powerful and Tunable THz Emitters Based on the Fe/Pt Magnetic Heterostructure. *Advanced Optical Materials* **4**, 1944–1949 (2016).

187. Meineke, C. *et al.* Scalable high-repetition-rate sub-half-cycle terahertz pulses from spatially indirect interband transitions. *Light: Science and Applications* **11**, 151 (2022).

188. Stein, M., Fuchs, C., Stolz, W., Mittleman, D. M. & Koch, M. Direct Probe of Room-Temperature Quantum-Tunneling Processes in Type-II Heterostructures Using Terahertz Emission Spectroscopy. *Physical Review Applied* **13**, 054073 (2020).

189. Planken, P. C. M., Nuss, M. C., Knox, W. H., Miller, D. A. & Goossen, K. W. THz pulses from the creation of polarized electron-hole pairs in biased quantum wells. *Applied Physics Letters* **61**, 2009–2011 (1992).

190. Nuss, M. C. *et al.* Terahertz electromagnetic radiation from quantum wells. *Applied Physics B Laser and Optics* **58**, 249–259 (1994).

191. Runge, M. *et al.* Mono-cycle terahertz pulses from intersubband shift currents in asymmetric semiconductor quantum wells. *Optica* **8**, 1638 (2021).

192. Laman, N., Bieler, M. & Van Driel, H. M. Ultrafast shift and injection currents observed in wurtzite semiconductors via emitted terahertz radiation. *Journal of Applied Physics* **98**, 103507 (2005).

193. Bieler, M., Pierz, K. & Siegner, U. Simultaneous generation of shift and injection currents in (110)-grown GaAsAlGaAs quantum wells. *Journal of Applied Physics* **100**, 083710 (2006).

194. Russbueldt, P., Mans, T., Weitenberg, J., Hoffmann, H. D. & Poprawe, R. Compact diode-pumped 11 kW Yb:YAG Innoslab femtosecond amplifier. *Optics Letters* **35**, 4169 (2010).

195. Saraceno, C. J. *et al.* Toward Millijoule-Level High-Power Ultrafast Thin-Disk Oscillators. *IEEE Journal of Selected Topics in Quantum Electronics* **21**, 106–123 (2015).

196. Russbueldt, P. *et al.* Innoslab Amplifiers. *IEEE Journal of Selected Topics in Quantum Electronics* **21**, 447–463 (2015).

197. Müller, M. *et al.* 1 kW 1 mJ eight-channel ultrafast fiber laser. *Optics Letters* **41**, 3439 (2016).

198. Russell, P. S. J. Photonic Crystal Fibers. *Science* **299**, 358–363 (2003).

199. Travers, J. C., Chang, W., Nold, J., Joly, N. Y. & St. J. Russell, P. Ultrafast nonlinear optics in gas-filled hollow-core photonic crystal fibers. *Journal of the Optical Society of America B* **28**, A11–A26 (2011).

200. Mak, K. F. *et al.* Compressing μJ-level pulses from 250 fs to sub-10 fs at 38-MHz repetition rate using two gas-filled hollow-core photonic crystal fiber stages. *Optics Letters* **40**, 1238 (2015).

201. Weitenberg, J. *et al.* Multi-pass-cell-based nonlinear pulse compression to 115 fs at 75 µJ pulse energy and 300 W average power. *Optics Express* **25**, 20502 (2017).

202. Weitenberg, J., Saule, T., Schulte, J. & Rußbüldt, P. Nonlinear Pulse Compression to Sub-40 fs at 4.5 μJ Pulse Energy by Multi-Pass-Cell Spectral Broadening. *IEEE Journal of Quantum Electronics* **53**, 8600204 (2017).

203. Fritsch, K., Poetzlberger, M., Pervak, V., Brons, J. & Pronin, O. All-solid-state multipass spectral broadening to sub-20 fs. *Optics Letters* **43**, 4643 (2018).

204. Travers, J. C., Grigorova, T. F., Brahms, C. & Belli, F. High-energy pulse self-compression and ultraviolet generation through soliton dynamics in hollow capillary fibres. *Nature Photonics* **13**, 547–554 (2019).

205. Anderson, D. & Lisak, M. Nonlinear asymmetric self-phase modulation and self-steepening of pulses in long optical waveguides. *Physical Review A* **27**, 1393–1398 (1983).

206. Mak, K. F., Travers, J. C., Joly, N. Y., Abdolvand, A. & Russell, P. S. J. Two techniques for temporal pulse compression in gas-filled hollow-core kagomé photonic crystal fiber. *Optics Letters* **38**, 3592 (2013).

207. Herriott, D., Kogelnik, H. & Kompfner, R. Off-Axis Paths in Spherical Mirror Interferometers. *Applied Optics* **3**, 523–526 (1964).

208. Malitson, I. H. Interspecimen Comparison of the Refractive Index of Fused Silica. *Journal of the Optical Society of America* **55**, 1205 (1965).

209. Panish, M. B. & Casey, H. C. Temperature dependence of the energy gap in GaAs. *Journal of Applied Physics* **40**, 163–167 (1969).

210. Feng, S., Winful, H. G. & Hellwarth, R. W. Gouy shift and temporal reshaping of focused single-cycle electromagnetic pulses. *Optics Letters* **23**, 1141 (1998).

211. Bäumner, A., Kira, M. & Koch, S. W. Charging dynamics in electrically pumped quantum wells. *IEEE Journal of Quantum Electronics* **45**, 1024–1032 (2009).

212. Kira, M. & Koch, S. W. *Semiconductor quantum optics* (Cambridge University Press, 2012).

213. Cahill, D. G. & Pohl, R. O. Lattice Vibrations And Heat Transport In Crystals And Glasses. *Annual Review of Physical Chemistry* **39**, 93–121 (1988).

214. Matthiesen, M. *et al.* Temperature dependent inverse spin Hall effect in Co/Pt spintronic emitters. *Applied Physics Letters* **116**, 212405 (2020).

215. Seo, M. A. *et al.* Terahertz field enhancement by a metallic nano slit operating beyond the skin-depth limit. *Nature Photonics* **3**, 152–156 (2009).

216. Savage, K. J. *et al.* Revealing the quantum regime in tunnelling plasmonics. *Nature* **491**, 574–577 (2012).

217. Yoshida, K., Shibata, K. & Hirakawa, K. Terahertz Field Enhancement and Photon-Assisted Tunneling in Single-Molecule Transistors. *Physical Review Letters* **115**, 138302 (2015).

218. Yoshioka, K. *et al.* Real-space coherent manipulation of electrons in a single tunnel junction by single-cycle terahertz electric fields. *Nature Photonics* **10**, 762–765 (2016).

219. Jelic, V. *et al.* Ultrafast terahertz control of extreme tunnel currents through single atoms on a silicon surface. *Nature Physics* **13**, 591–597 (2017).

220. Jestädt, R., Ruggenthaler, M., Oliveira, M. J., Rubio, A. & Appel, H. Light-matter interactions within the Ehrenfest–Maxwell–Pauli–Kohn–Sham framework: fundamentals, implementation, and nano-optical applications. *Advances in Physics* **68**, 225–333 (2019).

221. Barbry, M. *et al.* Atomistic near-field nanoplasmonics: Reaching atomic-scale resolution in nanooptics. *Nano Letters* **15**, 3410–3419 (2015).

222. Kang, J. H., Kim, D. S. & Park, Q. H. Local capacitor model for plasmonic electric field enhancement. *Physical Review Letters* **102**, 093906 (2009).

223. Hejazi, K., Luo, Z. X. & Balents, L. Noncollinear phases in moiré magnets. *Proceedings of the National Academy of Sciences of the United States of America* **117**, 10721–10726 (2020).

224. Song, T. *et al.* Direct visualization of magnetic domains and moiré magnetism in twisted 2D magnets. *Science* **374**, 1140–1144 (2021).

225. Boix-Constant, C. *et al.* Multistep magnetization switching in orthogonally twisted ferromagnetic monolayers. *Nature Materials*, **23**, 212–218 (2024).

226. Baumann, S. *et al.* Electron paramagnetic resonance of individual atoms on a surface. *Science* **350**, 417–420 (2015).

227. Sellies, L. *et al.* Single-molecule electron spin resonance by means of atomic force microscopy. *Nature* **624**, 64–68 (2023).

228. Sanvito, S. Molecular spintronics. *Chemical Society Reviews* **40**, 3336–3355 (2011).

229. Wang, K. *et al.* Ultrafast coherent control of a hole spin qubit in a germanium quantum dot. *Nature Communications* **13**, 206 (2022).

230. Panda, S. N., Rana, B., Otani, Y. C. & Barman, A. Role of Spin–Orbit Coupling on Ultrafast Spin Dynamics in Nonmagnet/Ferromagnet Heterostructures. *Advanced Quantum Technologies* **5**, 2200016 (2022).

231. Jompol, Y. *et al.* Probing Spin-Charge Separation in a Tomonaga-Luttinger Liquid. *Science* **325**, 597–601 (2009).

232. Schlappa, J. *et al.* Spin-orbital separation in the quasi-one-dimensional Mott insulator Sr_2CuO_3. *Nature* **485**, 82–85 (2012).

233. Novotny, L. & Hecht, B. *Principles of Nano-Optics* (Cambridge University Press, 2006).

234. Trebino, R. *et al.* Measuring ultrashort laser pulses in the time-frequency domain using frequency-resolved optical gating. *Review of Scientific Instruments* **68**, 3277–3295 (1997).

235. Kane, D. J. Recent progress toward real-time measurement of ultrashort laser pulses. *IEEE Journal of Quantum Electronics* **35**, 421–431 (1999).

236. Kampfrath, T., Nötzold, J. & Wolf, M. Sampling of broadband terahertz pulses with thick electro-optic crystals. *Applied Physics Letters* **90**, 231113 (2007).

237. Diels, J.-C. & Rudolph, W. *Ultrashort Laser Pulse Phenomena* (Academic Press, 2006).

238. Bracewell, R. *The Fourier Transform And Its Applications* (McGraw-Hill, 2000).

Acknowledgements

No project the size of a doctoral thesis can be tackled by one person alone – after all, science is a team sport. Therefore, at this point, I would like to thank both my scientific and non-scientific colleagues, companions and friends over the past years:

Prof. Dr. Rupert Huber mentored this work and, by his exceptional expertise combined with the gift for explaining complicated physical matters in a comprehensible way, greatly contributed to the success of this work. I am blessed not only to have been able to work on a project at the leading edge of research with state-of-the-art equipment but also to have had an advisor, who was not above helping out in the lab himself. His infectious curiosity and enthusiasm for physical questions were a constant source of inspiration and encouraged me to always delve a bit deeper into subjects. I will definitely profit from these lessons in the coming chapters in my life.

I very much enjoyed the fruitful exchange with **Prof. Dr. Jascha Repp** during both my master's and doctoral thesis, especially with regard to the highly promising B-field STM project. Moreover, I thank him for taking the time to assess my work.

I am also highly grateful to all members of the board of examiners formed by **Prof. Dr. Vladimir Braun**, **Prof. Dr. Rupert Huber**, **Prof. Dr. Jascha Repp** and **Prof. Dr. Jörg Wunderlich** for evaluating my work and conducting the oral examination.

I greatly appreciate the pleasant and successful collaboration with **Prof. Dr. Dominique Bougeard**, **Dr. Dieter Schuh** and **Dr. Michael Prager**. They greatly contributed to this work with the sophisticated design and high-quality growth of epitaxial heterostructures, which have emerged as unparalleled terahertz emitters.

Martin Furthmeier embodies the attitude "if there is a problem, there is a solution" like few others. Martin designed countless optomechanical components, housings and water-cooling units, without which none of the experiments in this thesis would have been possible. Most notably, he managed all of this in an unparalleled pace, from which this work profited tremendously.

Ulla Franzke, the good soul of the chair and the guide who lead and still leads not only me, but our entire group safely through the jungle of German bureaucracy.

Imke Gronwald made this work possible in the first place with her outstandingly exfoliated monolayers. Imke was always very supportive and brave enough to polish GaAs wafers with highly dangerous chemicals.

Ignaz Läpple was always ready to step in where my knowledge of electrical engineering found its limits. Every terahertz waveform presented in this thesis was measured with the help of his diode circuits.

Dr. Markus A. Huber supported me setting up a near-field microscope in my lab in record time. Markus' enthusiasm for Blender, which has passed on to me to some extent, was definitely beneficial to the aesthetics of this work. I thank him for all the helpful discussions and always having an open door.

Dr. Dominik Peller accompanied my scientific journey from my master's thesis onwards and, especially in the beginning, helped to shape it with his unique wit and efficient work style. Away from science, delightful evening walks, mountain hikes and long-distance as well as high-speed bike rides, including an epic alpine crossing, have forged a friendship for which I would like to thank him here.

Dr. Philipp Merkl guided my first steps in the lab, giving me confidence working with a high-power laser with his calm aura. I also really enjoyed working together on the Fourier pulse synthesis project.

Dr. Tom Siday also selflessly supported me in my early "near-field career", giving me both theoretical background and practical tips for my newly acquired microscope.

Dr. Lukas Kastner and I, after following an almost parallel curriculum, ended up in the same group and even worked on related projects, making us long-term companions. Thank you for the constant pleasant exchange over the last years. I also have fond memories of our multiple bike rides together, particularly of course our alpine adventures.

Simon Maier and **Carmen Roelcke** also accompanied my PhD thesis from its very beginning. Thank you for the pleasant time in the coffee kitchen discussing science and everything but science, the "Selbsthilfegruppe" meetings and of course the many activities after work, including Yoga, bouldering and enjoying Carmen's fantastic violin play.

I had the honour to co-guide **Johannes Hayes**' first steps in science, starting from his bachelor's thesis. Luckily, he continued working with me during his master's thesis. Thank you for the extraordinarily pleasant shared time in the lab and office, which was both entertaining and fruitful. In my view, our joint writing process of the manuscript on the quantum well emitters was a prime example of synergy that led to me having a positive time despite the time pressure. I am also thankful for all the nice common memories outside of work, especially of course our shared bikepacking and bike racing experiences.

Martin Zizlsperger was a great support when I was introduced to near-field microscopy. I deeply appreciate and admire his work ethics, combined with his selfless attitude and all the helpful scientific and non-scientific discussions we had. Outside of work we spent very pleasant time together bouldering and hanging out at the Danube. I also greatly appreciate our hilarious exchange of memes.

Jakob Schlosser has managed extraordinarily well not only to familiarise himself with a project in its final stages at record speed, right at the beginning of his master's thesis, but also to significantly contribute to it. Owing to this talent and his sympathetic and open-minded nature, it was and still is a pleasure for me to co-guide his master's thesis.

Christian Weidgans supported me during his bachelor's thesis in fine-tuning and characterising the performance of our self-made optical parametric amplifier. Thanks for the enjoyable time in the lab!

I also had the privilege of having pleasant office mates for the entirety of my time in the Huber group. My special thanks go to **Martin Zizlsperger**, **Svenja Nerreter**, **Simon Anglhuber** and **Jakob Schlosser**, who never let dullness come into my everyday office life, but at the same time created a productive working atmosphere.

Here, I want to express my gratitude towards the entire **Huber group**, where I found a collegiality between peers that will be hard to find anywhere else. I greatly appreciate the friendly atmosphere, fun evenings and fruitful discussions with this brilliant bunch of people.

I also thank our collaboration partners **Prof. Dr. Oleg Pronin**, **Kilian Fritsch**, **Prof. Dr. Mackillo Kira**, **Qiannan Wen**, **Dr. Markus Stein** and **Dr. Florian Dirnberger**.

My special thanks go to **Dr. Markus Huber**, **Dr. Lukas Kastner**, **Johannes Hayes** and **Martin Zizslperger** for their valuable feedback on my thesis!

Finally, I would like to thank my parents for their unwavering support throughout the past three decades. Without them, I would not be, where I am today. Therefore, I dedicate this work to them.